國 立 交 通 大 學

資 訊 科 學 與 工 程 研 究 所
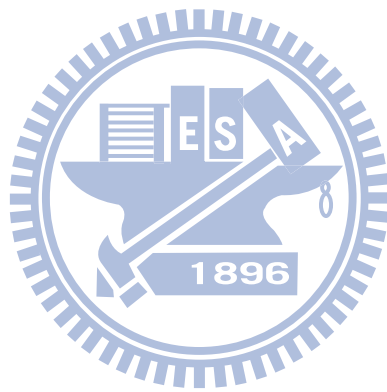## 博 士 論 文

無線區域網路第一層與第二層核心技術
之設計與實現

**Design and Implementation of WLAN Layer 1 and
Layer 2 Core Techniques**

研 究 生：鄭紹余

指導教授：許騰尹

中 華 民 國 一 百 年 七 月

無線區域網路第一層與第二層核心技術
之設計與實現

Design and Implementation of WLAN

Layer 1 and Layer 2 Core Techniques

研 究 生：鄭紹余　　　　Student：Shau-Yu Cheng

指導教授：許騰尹 博士　　Advisor：Dr. Terng-Yin Hsu

國 立 交 通 大 學

資 訊 科 學 與 工 程 研 究 所

博 士 論 文

A Dissertation

Submitted to Department of Computer Science

College of Computer Sicience

National Chiao Tung University

in Partial Fulfillment of the Requirements

for the Degree of Doctor of Philosophy

in

Computer Science

July 2011

Hsinchu, Taiwan, Republic of China

中 華 民 國 一 百 年 七 月

無線區域網路第一層與第二層
核心技術之設計與實現

鄭紹余

國立交通大學資訊科學與工程研究所

指導教授：許騰尹 教授

摘要

對於一個支持 IEEE 802.11 的接收器來說，最近以來的一個挑戰就是讓接收器架構越簡潔越好，譬如在無循環前綴單載波分組傳輸(non-cyclic prefix single-carrier block transmission, non-CP SCBT))、單輸入單輸出(single-input single-output, SISO)與多輸入多輸出(multi-input multi-output，MIMO)正交頻分複用(orthogonal frequency division multiplexing，OFDM)間進行有效率的硬體共享。基於頻率域類比數位轉換器(frequency-domain analog-to-digital conversion, FD-ADC)技術，本論文提出了一個多模接收器在頻率域上去處理所有的數位訊號，為了要在頻率域回復符號時序(symbol timing)，本論文提出了一個採用了符號速率循序並用匹配濾波器(matched filter)結果去搜尋的頻率域符號同步器(FD symbol synchronizer)，由模擬與實作結果顯示這個提出的頻率域符號同步器在低訊雜比下仍然很強健並且在 VLSI 實作上有很低的複雜度。而為了要讓等化器(equalizer)盡量簡潔，在無循環前綴單載波分組傳輸上，另外也提出了一個採用了單 FFT 架構以及球面解碼(sphere decoding)演算法的單載波頻率域等化器(SC-FDE)，因此 IEEE 802.11b 的等化可共用 MIMO-OFDM 收發機中的硬體元件。除此之外，我們還設計了一個事前修剪的技術去更進一步降低使用空間多工多輸

入多輸出傳輸中信號偵測的複雜度，這個事前修剪的技術利用 zero forcing (ZF) 的偵測結果及 N_q-QAM 星座圖上多層次結構的特性去減少傳統 K-best 演算法的搜尋空間，因此這方法很適合同時擁有 K-best 及 ZF 偵測器的接收器。

除了上述的實體層問題外，因為無線高速網際網路(Internet)的存取的增加讓資料由存取網路(access network)轉傳到網際網路的高速無線後置網路(wireless backhaul network)的需求變的必要，而實務上更高的傳輸率要更高的基地台密度，因此使得在高速無線後置網路的佈署中，使用基礎網路的架構變的不符成本效益，在這情況下，IEEE 802.11s 無線網狀網路(wireless mesh network, WMN) 提供一個吸引人的方法來快速且低成本的佈署，在本論文中研發了 IEEE 802.11s 無線網狀網路並實際佈署了一個 3x3 的格狀拓樸網狀網路在實驗室及一個跨三層樓的建築物中，考量到無線網狀功能的可攜性，網狀網路的開發是在一個現成的商用無線晶片中的純軟體延伸，其中使用模組化軟體設計及不需要高成本硬體更動，為了要加強傳輸廣播類(broadcast-type)網狀網路控制封包的可信度，數種廣播策略在實驗室中進行路由重建率、可接受的延遲及通道使用率等評量，對於網狀網路的佈署上，我們的觀察指出 RTS/CTS 可以增加網路吞吐量達到 87.5%，另外比起使用 IEEE 802.11b/g，用 802.11n 傳輸可在多重資料流(multi-stream)或多點跳躍(multi-hop)的通訊上能達到更好的公平性(fairness)，在本論文中總結的網狀網路的實驗觀察希望能提供給要佈署小型或中型室內 IEEE 802.11s 無線網狀網路的人一些導引。

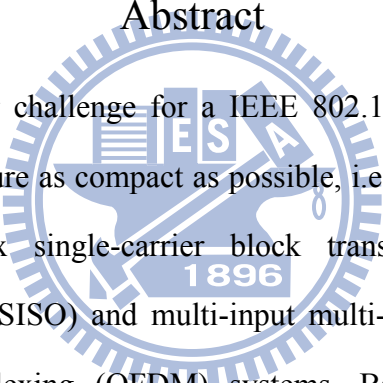# Design and Implementation of WLAN Layer 1 and Layer 2 Core Techniques

By

Shau-Yu Cheng

Department of Computer Science

National Chiao Tung University

Advisor: Terng-Yin Hsu

Abstract

Recently, one of the major challenge for a IEEE 802.11 compatible receiver is to make the receiver architecture as compact as possible, i.e., efficient hardware sharing between non-cyclic prefix single-carrier block transmission (non-CP SCBT), single-input single-output (SISO) and multi-input multi-output (MIMO) orthogonal frequency division multiplexing (OFDM) systems. Based on frequency-domain analog-to-digital conversion (FD-ADC) technology, this dissertation presents a multi-mode receiver to handle all digital signals in frequency domain. A frequency-domain (FD) symbol synchronizer adopting a symbol-rate sequential search with simple matched filter detection is presented to recover symbol timing over the frequency domain. Simulation and implementation results show that the proposed FD symbol synchronizer is robust at low single-to-noise (SNR) and low complexity for VLSI implementations. To make equalizer as compact as possible, a single-carrier frequency-domain equalization (SC-FDE) for non-CP SCBT is proposed with single-FFT architecture and sphere decoding algorithm. Thus, the equalization of IEEE 802.11b can reuse the hardware components in the MIMO-OFDM modem.

Moreover, a pre-pruning scheme is designed to further reduce the complexity of MIMO detection module for MIMO transmission using spatial multiplexing. The pre-pruning scheme reduces the search space of conventional K-best algorithm by using the zero forcing (ZF) detection result and the property of multilevel structure in N_q-QAM constellation. Hence, it is very attractive for the receivers equipping with both K-best and ZF detectors.

In spite the issues mentioned above in physical layer, a high rate wireless backhaul network transporting data between the access network and the wired Internet becomes essential due to the increasing of wireless high-speed Internet access. The infrastructure network becomes cost ineffective in the deployment of a high-rate wireless backhaul network due to the higher data rates requires much higher cell densities to realize in practice. Under this situation, IEEE 802.11s wireless mesh network (WMN) can provide an attractive approach for the fast and low cost deployment. This dissertation develops an IEEE 802.11s WMN and then deploys a testbed with 3-by-3 grid topology in both laboratory and field crossing three floors of the building. For the portability of mesh functions, the mesh development is a pure software extension for commercial off-the-shelf WLAN chipsets with modularized software design and without costly hardware modifications. To improve the transmission reliability of broadcast-type mesh control frames, several broadcasting strategies are evaluated based on the routing construction ratio, acceptable latency, and channel utilization in the laboratory testbed. For the WMN deployment, our observations indicate that RTS/CTS can improve throughput by up to 87.5%. Moreover, compared with the IEEE 802.11b/g, 802.11n achieves better fairness for multi-stream or multi-hop communications. The experimental observations of WMN deployment summarized in this dissertation are expected to provide guidance for the small or medium scale indoor IEEE 802.11s WMN.

Acknowledgements

I would like to express my sincere gratitude to my dissertation advisor, Prof. Terng-Yin Hsu, for his kind guidance, assistance, consultation, and encouragement during the course of my graduate study. Whenever I encounter difficulties or feel disappointment for my work, either in the research or in the daily life, he always tries to give me a hand and lead me to an appropriate place.

Also, I would like to thank many of present and former ISIP members: Wei-Chi Lai, Cheng-Yuan Lee, and Kai-Shu Su, whose contributions were instrumental in the development of ideas. Moreover, I will keep in mind for the friendship coming form You-Hsien Lin, Chueh-An Tsai, Shao-Ying Yeh, and Tsung-Yeh He.

The thanks also goes to the Realtek-NCTU jointly research center for its complete research environment and financial support during the several years of my Ph.D study. Particularly, I would like to thank the chief director, Prof. Ying-Dar Lin and the technical adviser, Prof. Shiao-Li Tsao, for their open management and valuable comments. In addition, I never forget the useful cooperation experience coming from Der-Zheng Liu, David Hsu, Shun-Lee Chang, and Jui-Hung Yeh.

Furthermore, I want to share my happiness with my family, especially for my dear parents for their ageless love during my whole life. In addition, I take thanks for the parents of my wife. Without their assistance and blessing, this dissertation might not be worked out and I could not reach where I am now.

Finally, and that is also the most important of all, I have to express my appreciation to my wife, Etta Fan, for her endless love, inexhaustible understanding, and dependable harbor, especially the patience and waiting for so many lonely moments.
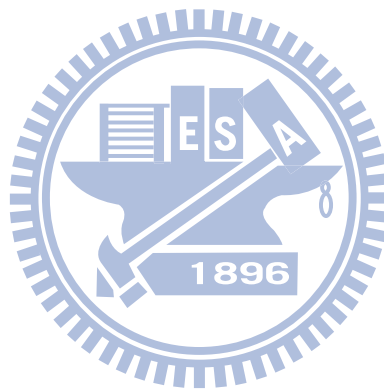
Shau-Yu Cheng

Hsinchu, Taiwan

Table of Contents

List of Figures

List of Tables

List of Acronyms

The following acronyms are used through this dissertation.

ACK	acknowledgment
ACI	adjacent channel interference
ADC	analog-to-digital conversion
AFC	automatic frequency control
AGC	auto gain control
AODV	Ad Hoc On-Demand Vector
AP	access point
ARF	automatic rate fallback
AWGN	additive white Gaussian noise
B&B	branch and bound
CCK	complementary code keying
CFO	carrier frequency offset
CFR	channel frequency response
CMOS	complementary metal-oxide-semiconductor
CoMP	coordinated multipoint transmission
CP	cyclic prefix
CPU	central processing unit
CTS	clear to send
DF-AC	decision-feedback aliasing canceller
DFT	discrete Fourier transform
DHCP	dynamic host configuration protocol
DSP	digital signal processor
DSSS	direct sequence spread spectrum
DST	destination node
EVM	error vector magnitude

FD	frequency-domain
FD-ADC	frequency-domain analog-to-digital conversion
FD-CE	FD channel estimator
FFT	fast Fourier transform
FPGA	field programmable gate array
HWMP	hybrid wireless mesh protocol
IBI	interblock interference
IFS	inter-frame space
IEEE	Institute of Electrical and Electronics Engineers
JAER	just-acceptable error rate
JTC	Joint Standards Committee
LUT	look up table
LTE-A	Long Term Evolution-Advance
MAC	media access control
MANETs	mobile ad hoc networks
MAP	mesh access point
MCN	multihop cellular network
MIMO	multi-input multi-output
ML	maximum-likelihood
MLD	maximum likelihood detection
MP	mesh point
MPP	mesh portal
MU-MIMO	multi-user MIMO
OFDM	orthogonal frequency-division multiplexing
OLPC	One Laptop per Child
PED	partial Euclidean distance
PAPR	peak-to-average power ratio
PER	packet error rate
PHY	physical
PN	pseudo noise

PREP	path response
PREQ	path request
QPSK	Quadrature phase-shift keying
RMS	root mean square
ROM	read-only memory
RTS	request to send
SC	single-carrier
SCBT	single-carrier block transmission
SC-FDE	single-carrier frequency-domain equalization
SD	sphere decoder
SDR	software-defined radio
SISO	single-input single-output
SM	spatial multiplexing
SNR	signal-to-noise ratio
SRAM	static random-access memory
SRC	source node
SSC	semi-synchronous clocker
SSCG	semi-synchronous clock generator
STA	station
TCP	Transmission Control Protocol
TD	time-domain
TDC	time-to-digital converter
TSMC	Taiwan Semiconductor Manufacturing Company
UCG	unified channel graph
VHT	very high throughput
VLSI	very large scale integration
WDS	wireless distribution system
WLAN	wireless local area network
WMN	wireless mesh network
WPAN	wireless personal area network

Chapter 1

Introduction

In recent years, broadband wireless communications have been considered as the key enabling technology for innovative future consumer products. Moreover, applications like multimedia sharing and cloud computing grow the demands of higher data rate transmission in wireless communication system. Being the most popular and successful wireless broadband network standard, IEEE 802.11 [1] wireless local area network (WLAN) has be adopted in client devices over several hundreds million worldwide. WLAN radios are appearing not just in PCs and laptops, but in equipment as diverse as mobile phones/pads, security cameras and home entertainment equipment, etc. With large, diverse and rapidly growing WLAN installed bases, the research and development investment in WLAN technology becomes very important.

IEEE 802.11 is a set of standards consisting of the base standard [1] defined in 1997 and a series of amendments started from 1999 [2]-[5]. The evolution of IEEE 802.11 is still ongoing. The base standard is originally designed for 1 and 2 Mbps throughput and is now being upgraded to support 600 Mbps in 802.11n and is being considered as a high-throughput (up to several Gbps) wireless interface for the multimedia data service in the scope of the next-generation of wireless systems. To support higher data rate with backward compatibility during the evolutions of amendments, IEEE 802.11 adopts two radio modulation schemes: non-cyclic prefix single-carrier block transmission (non-CP SCBT) and orthogonal frequency division multiplexing (OFDM). In addition, the radio system is evaluated from single-input single-output (SISO) to multi-input multi-output (MIMO) for the transmission rate over hundreds Mbps. These advances of radio technologies make a high demand for multi-mode receiver design to support non-CP SCBT, SISO OFDM and MIMO OFDM transmission in modern WLAN applications.

It is also recognizes that the later amendments usually provide higher data rate with shorter transmission distance. For example, typical access points can provide 54 Mbps data rates only up to tens of feet whereas they can extend 11 Mbps data rates up to hundreds of feet. This is because these higher rates require higher levels of signal-to-noise ratio (SNR) at the receiver. In other words, these higher data rates will

require much higher cell densities to realize in practice. To construct a high-data rate network with conventional infrastructure architecture, the deployment cost could be unacceptable. Therefore, the relay-based network architecture is essential for current and next generation WLAN applications. Currently, the relay-based network can be achieved by deployment with Ad hoc or wireless distribution system (WDS) modes. However, Ad hoc can not let client devices connect to Internet while WDS loses the flexibly of deployment with manually configurations and static network topology. To overcome those drawbacks, The 802.11s Task Group is now working on an infrastructure mesh amendment to allow 802.11 access points or cells from multiple manufacturers to self-configure into multi-hop wireless topologies. Example usage scenarios for mesh networks include interconnectivity for devices in the digital home, unwired campuses, and community area networks or hotzones.

To build a low cost, high rate, high flexibility WLAN network, there are still many challenges issues need more research investment. In this dissertation, we focus on the design of IEEE 802.11 compatible multi-mode receiver and development of IEEE 802.11s wireless mesh works.

1.1 Introduction of WLAN Radio technologies

The radio technologies of IEEE 802.11 family include two modulation schemes: non-CP SCBT and OFDM modulations. The non-CP SCBT is a type of single-carrier (SC) modulation, which is adopted in the original (legacy) standard 802.11-1997 and the first amendments IEEE 802.11b [2]. The non-CP SCBT modulation owns the good characteristics of friendly front-end implementation and insensitive impact on CFO [6]. However, non-CP SCBT modulation provides lower frequency spectrum efficiency than OFDM modulation scheme and complex design of equalizer in time domain. Therefore, IEEE 802.11a [3] provides an alternative approach with OFDM modulation to provide high data rate up to 54Mbps in the 5GHz unlicensed bands. The 2.4GHz OFDM system is first started from 802.11g [4] in 2003, which is a backwards-compatible extension to the 802.11b standard allows data rates up to 54 Mbps through use of OFDM or complementary code keying (CCK) modulation in the 2.4GHz band. The advantages of OFDM modulation is well known to have high spectrum efficiency and robust to multipath fading (i.e., frequency-selective) channels. However, the requirement of the front-end for OFDM is stricter than non-CP SCBT modulation because its nature of high peak-to-average power ratio (PAPR) and sensitive to carrier frequency offset (CFO) [7]. In order to support the data rate up to

few hundreds megabits per second, OFDM-based MIMO spatial multiplexing (SM) technique is introduced in the latest amendment IEEE 802.11n [5]. MIMO system can significantly improve the spectrum efficiency and achieve a much higher transmission rate than a SISO system. In addition, combining OFDM and MIMO can simplify the implementation of MIMO detection in receiver architecture. Table 1-1 summarizes the radio technologies in IEEE 802.11 legacy and its amendments.

Table 1-1 Summary of IEEE 802.11 PHY related standards

802.11 std	Release	Freq. (GHz)	BW (MHz)	Max. Data rate (MBit/s)	Max # of stream	Modulation
Legacy [1]	Jun 1997	2.4	20	2	1	non-CP SCBT (DSSS)
a[3]	Sep 1999	5	20	54	1	OFDM
b[2]	Sep 1999	2.4	20	11	1	non-CP SCBT (DSSS/CCK)
g[4]	Jun 2003	2.4	20	54	1	OFDM, non-CP SCBT (DSSS/CCK)
n[5]	Oct 2009	2.4/ 5	20	288.8	4	OFDM
			40	600		
Note: DSSS and CCK represent direct sequence spread spectrum, and complementary code keying, respectively.						

1.2 Introduction of WLAN Relay-based Backhaul Network

Infrastructure-based wireless networks provide convenient access to the Internet, and are becoming increasingly popular in spite of their costly wired deployment. On the other hand, mobile ad hoc networks (MANETs) eliminate the need for infrastructure, decreasing deployment time and alleviating network construction costs. However, having routing functions on all nodes in a MANET complicates the design of networking devices [8]. The fact that MANET usage is typically limited to military and specialized civilian applications also hinders its growth [9]. By combining an infrastructure-based wireless network and a MANET, a wireless mesh network (WMN) presents a low-cost and fast-deployment solution compared to an infrastructure-based wireless network, and a reliable and less complicated solution compared to a MANET. A WMN is similar to a multihop cellular network (MCN) [10], which has been proved to improve aggregated throughput linearly due to spatial division.

In [8], the authors classify the WMN architecture into three types: infrastructure, client, and hybrid. An infrastructure WMN is organized as a hierarchical network, functionally consisting of mesh gateways, relay points, access points, and terminals. A

mesh gateway is a device capable of bridging the wireless mesh and wired

infrastructure. A relay point implements a routing algorithm to relay packets in a mesh.

To support non-mesh terminals, the mesh uses access points to bridge the WMN and

non-mesh terminals. In a client mesh there is no gateway and non-mesh terminal

because this kind of mesh emphasizes flat peer-to-peer communications. A hybrid

mesh includes both infrastructure and mesh terminals that provide interfaces for end

users and mesh routing capability.

Diverse mesh architectures result in various usage scenarios [8]-[9], and a

considerable number of challenges for designing and realizing a WMN [8], [11]–[13].

Industrial organizations have also prepared standards and recommended practices for

existing wireless technologies, such as IEEE 802.15.5 for low-rate wireless personal

area networks (WPANs). Among these efforts, IEEE 802.11s [14], which defines a

WLAN mesh using IEEE 802.11 MAC and PHY layers, is one of the most active

standards and has increasing commercial opportunities. Figure 1-1 shows the

architecture of mesh IEEE 802.11s network. The IEEE 802.11s standard uses the

IEEE 802.11 MAC and PHY, and has drawn numerous research and commercial

interests in recent years. Unlike ad hoc networks and sensor networks that are

motivated by military or crisis applications, WMNs introduce the commercial

applications such as the last-mile wireless access or home wireless networking.

WMNs can largely reduce the cost and complexity of network deployment by multi-hop relaying. The 802.11s WMN is composed of mesh portals (MPPs), mesh points (MPs), mesh access points (MAPs), and wireless stations (STAs). An MPP connects the WMN and the Internet. MPPs, MAPs, and MPs communicate with one another via the wireless medium and form a wireless backbone network. Then, STAs that associate with an MAP can communicate with the other STAs or access the Internet.

Figure 1-1: IEEE 802.11s mesh networks architecture

1.3 Problem Statement and Literature Survey

From the Table 1-1, it is clearly that the IEEE 802.11 receiver needs to be multi-mode design to support both non-CP SCBT (802.11b) and OFDM (802.11 a/n) modes. In practice, most of the implementations of multi-mode receivers use dedicated hardware to support both non-CP SCBT and OFDM systems as shown in Fig 1-2. However, those dedicated modules are difficult to be shared and merged for different modes, which leads high cost and large die size in implementations. For example, the different packet format and coding scheme between non-CP SCBT and OFDM may lead difficult hardware sharing in synchronization, equalization and data decoding modules. Moreover, the less hardware sharing introduces complex control path and cost inefficiently in receiver design. Although the software-defined radio (SDR) solution [15]-[16] implemented with digital signal processors (DSPs), central processing unit (CPU) and field programmable gate array (FPGA) provides the flexible solutions for multi-mode applications, the designers still need to consider the complex data path introduced by different signal formats, i.e. time-domain signals in the pre-fast Fourier transform (pre-FFT) phase and frequency-domain signals in the post-FFT phase. The complex data path might cause bad influences in the pipeline design, e.g., data hazards, hard to identify pipeline stages and complex instruction sets,

which results in higher clock rate and more complex control circuit in hardware implementation [17]. To avoid the switch of data path between time and frequency domains, handling all signals in frequency domain after conventional ADC followed by FFT is investigated in the research [18].

Recently, the concept of FD receiver with FD-ADC technology [19]-[23] is proposed as a potential solution for a multi-standard receiver. Unlike the typical OFDM receiver architecture based on conventional analog-to-digital conversion (ADC) and time-domain (TD) synchronization followed by FFTs and data decoding in frequency domain, a FD receiver directly handles all signal processes in frequency domain. To reduce signal formats transformation between domains and increase the hardware sharing between two modes, this dissertation adopts the FD receiver architecture to support for WLAN multi-mode applications.

Based on the FD-ADC technology, Fig. 1-3 shows the proposed multi-mode FD receiver architecture. To realize this FD receiver, two problems need to be overcome: symbol synchronization and non-CP SCBT equalization over frequency domain. Although a number of methods for symbol synchronizations [24]-[32] have been proposed, they are all developed based on TD-ADC based receiver which decides the symbol boundary by a sliding window before FFT. However, FD ADC transforms a segment of continuous time-domain signal to a set of frequency coefficients. Since

those synchronization algorithms performs sample-by-sample search for correlation peak within the sliding window, they can not function with FD-ADC technology properly. Therefore, the synchronization problem of the FD receiver architecture is to detect symbol boundary with frequency coefficients of FD-ADC outputs. For OFDM-based packets, the channel frequency response (CFR) can be obtained from the frequency response of received OFDM symbol divided by the frequency response of the frequency domain training symbol (long training symbol) due to the existence of cyclic-prefix (CP) [33]. For equalization of non-CP SCBT over frequency domain, a single-carrier frequency-domain equalizer (SC-FDE) is developed to eliminate FFT aliasing without a circular property in some approaches [34]-[35], e.g., overlap-and-save and overlap-and-add methods. Yet, additional DFT units were included—hardware complexity of the multi-mode FD receiver may increase significantly. Thus, one of the major challenge for multi-mode integrations is to make equalizers as compact as possible, i.e., consolidation of non-CP SCBT, SISO OFDM and MIMO OFDM. Finally, it is also important to reduce the complexity of MIMO detection module for a low cost receiver design. Numbers of methods have proposed in the literature [36]-[43]. However, those methods include some of the following drawbacks, i.e., poor performance, unacceptable complexity, not favored for VLSI implementation. Therefore, the design of a low complexity MIMO detection method

is investigated in this dissertation.
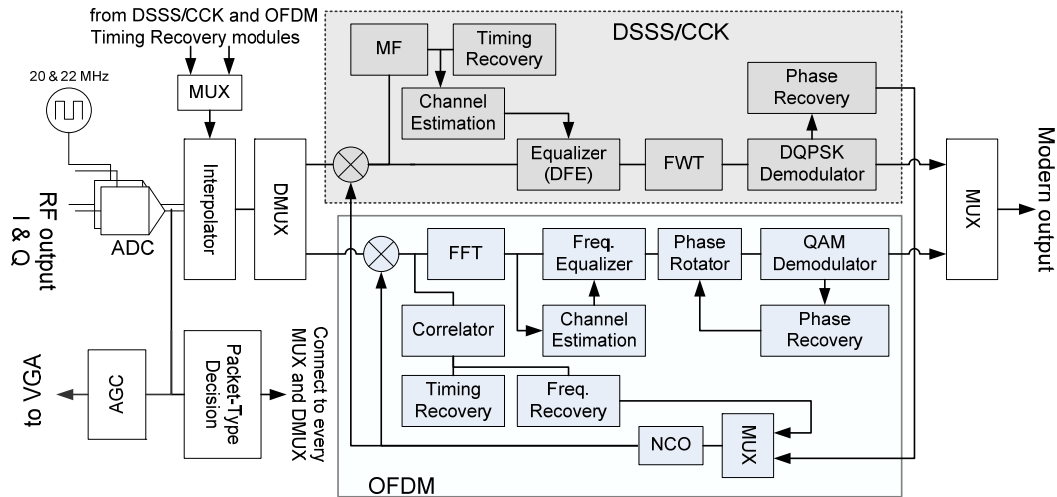
Figure 1-2: Block diagram of the conventional 802.11 b/g/n/ac multi-mode receiver.
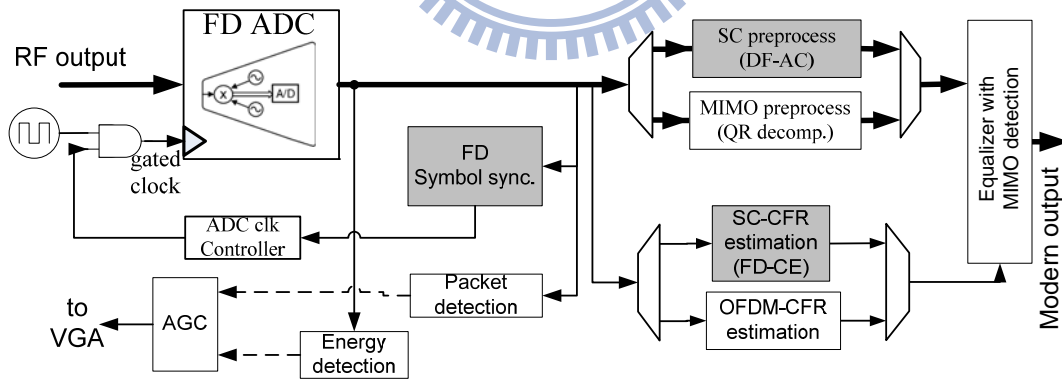
Figure 1-3: The proposed FD receiver architecture for SCBT and OFDM systems, where dash lines are the control signals, thin solid lines are the synchronization and channel estimation paths, and bold solid lines represent the data paths.

Besides the multi-mode integration issue, another important issue for modern WLAN applications is to provide cost effective and high rate networks over a wider coverage area. From radio technique perspective, MIMO scheme can provide the high date rate transmission yet it also requires good link quality which means the coverage of high rate transmission is very small. As shown in Fig. 1-4, the coverage can be extended by deploying an IEEE 802.11s WMN. Therefore, the knowledge related to the development and deployment of an IEEE 802.11s system becomes emergency topic for WLAN research filed recently. Although Prior studies, such as the mesh on XO-laptop for One Laptop per Child (OLPC) [44] and the open80211s project for Linux, has evaluated the network performance of the IEEE 802.11s mesh, few studies examine system architectures and mesh stability. Moreover, conventional mesh deployment [8], [45]-[50] focuses on the outdoor environment, which regards the WMNs as backbone networks. For WLAN application, the backhaul network is usually considered as an indoor deployment. However, indoor and outdoor WMNs possess distinguishable attributes and limitations. To the best of our knowledge, only a little previous work focuses on indoor WMNs [45]-[46].
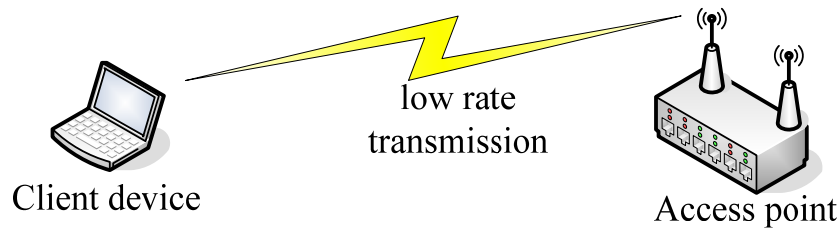
(a)
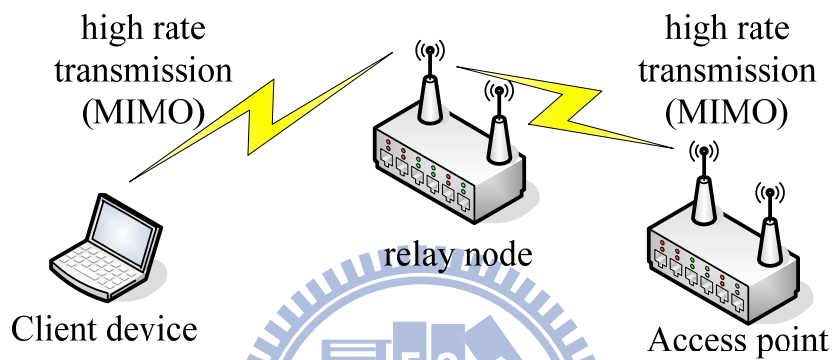
(b)

Figure 1-4: (a) the conventional WLAN infrastructure. (b) relay-based WLAN infrastructure.

1.4 Dissertation Overview

The designs of FD receiver architecture and its key components of synchronizer and equalizer are discussed in Chapters 2, 3 and 4 while the design, implementation and deployment of IEEE 802.11s mesh network are discussed in Chapters 5 and 6. Details of the research contributions in each chapter are as follows.

In Chapter 2, we design and implement a low-complexity sequential searcher for

robust symbol synchronization in a 4x4 FD MIMO-OFDM modem. Based on the FD

ADC, the searcher finds symbol boundary at symbol-rate and then the hardware

sharing can successfully accomplish low-complexity implementations Moreover, this

chapter also includes the design and implement of a very low complexity clock

generator, called semi-synchronous clock generator (SSCG), to provide a high-speed

clocking.

In Chapter 3, we design and implement a single-FFT approach SC

frequency-domain equalization (FDE) approach for non-CP SCBT system. This

approach makes IEEE 802.11b data packet can be equalized in frequency domain for

FD receiver architecture. Moreover, the approach can be implemented by sphere

decoder (SD) algorithm [51] which is widely adopted in MIMO-OFDM modems.

Thus, the efficient hardware sharing of equalization module in FD receiver can be

achieved.

In Chapter 4, we propose a pre-pruning scheme to reduce the search space of

K-best algorithm. Based on the property of multilevel structure in N_q-QAM

constellation, the scheme adopts a cluster-based search to find the reliable

constellation points according to the ZF detection results. Compared to the

conventional K-best algorithm [40] with the same K value, the proposed work

achieves the same performance with fewer search nodes (67.6%~77.21% of the

conventional K-best algorithm). Hence, the proposed pre-pruning scheme is attractive for those receivers equipping with both K-best and ZF detectors.

In Chapter 5, we develop a prototype of WLAN mesh network based on the draft D2.03 of IEEE 802.11s, and port the mesh functions to the commercial off-the-shelf WLAN chipsets such as Realtek RTL8186 and Realtek RTL8192SE+RTL8196B platforms. Then, we evaluate the design strategies for broadcast-type mesh control frames.

In Chapter 6, we present a two-phase deployment plan with 3-by-3 grid topology to establish the benchmark of the implemented mesh network in last chapter. In the first phase, the testbed was deployed in a laboratory to evaluate its basic capacity and performance for a dense deployment. In the second phase, the grid WMN was deployed in the sixth to eighth floors of the Microelectronics and Information Systems Research Center (MIRC) at National Chiao Tung University. The experiments mainly focus on the effects of different IEEE 802.11 settings, including RTS/CTS, links with IEEE 802.11n or IEEE 802.11b/g, and beacon interval. Finally, the experimental observations are summarized to provide guidance for small or medium scale indoor 802.11 WMNs.

In Chapter 7, we draw some conclusions of this work and outline possible topics for further research.

Part I PHY Layer: Three Key modules for Multi-mode FD receiver
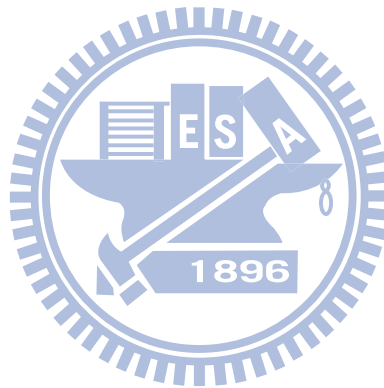
Chapter 2

Symbol Rate Frame

Synchronization with FD-ADC

Architecture

Based on the FD ADC, this chapter builds a low-complexity sequential searcher for

robust symbol synchronization in a 4x4 frequency-domain (FD) multiple-input

multiple-output orthogonal frequency-division multiplexing (MIMO-OFDM) modem.

The proposed scheme adopts a symbol-rate sequential search with simple matched

filter detection to recover symbol timing over the frequency domain. Simulation

results show that the detection error is less than 2% at SNR $\leqq$ 5 dB. And

performance loss is not significant when carrier frequency offset (CFO) $\leqq$ 100 ppm.

Using an in-house 65-nm CMOS technology, the proposed solution occupies 84.881K gates and consumes 5.2mW at 1.0V supply voltage. This work makes the FD ADC more attractive to be adopted in high throughput OFDM systems.

Symbol synchronization is one of the essential processes to correctly detect symbol boundary in wireless packet-based receiver. The incorrect boundary disarranges the amplitude as well as the phase of the received signal. Moreover, it causes the error position of FFT windows within orthogonal frequency-division multiplexing (OFDM) symbols, introducing intersymbol and interference (ISI) and significant performance degradation during data demodulation. To guarantee the system performance, the reliability of symbol synchronization is therefore critical to OFDM-based systems.

Based on the receiver architecture using conventional ADC (Fig. 2-1(a)), numbers of symbol synchronizers have been revealed in the literature. By exploiting the known structure of the preamble or the cyclic prefix, a number of methods for OFDM symbol synchronization have been proposed in the literature. The autocorrelation-based method [24] is presented to find the peak of correlation between the previous and current received symbols. The implementation is rather simple but the correlation peak of the timing metric exhibits a plateau which causes large variance for the timing estimator [25]. The cross-correlation method [26] uses a

"clean" copy of the preamble to form a matched filter which is applied to the received

symbol. In spite of the advantage of more accurate timing detection, more sensitive to

the carrier frequency offsets [27] and higher implementation complexity of the

matched filer [28] are the main drawbacks. The double correlation metric [29] is

presented to develop a reliable frequency and time synchronization scheme. However,

its complexity is also doubled. Although those correlation-based methods mentioned

above are suitable for hardware implementations, the performances are easily affected

by multipath fading [30]. To overcome this limitation, the generalized Akaike

information criterion (GAIC) [31] and [32] are presented to jointly estimate the

channel order and establish the symbol timing. Both of the two method provide a

pretty good performance when SNR $\geq$ 10 dB. However, the two methods are more

complex than the correlation-based methods.

Recently, frequency-domain analog-to-digital conversion (ADC) for OFDM

applications [19]–[23] has been reported to gain several advantages, e.g., the

relaxation of ADC requirements, robustness in narrow band interference (NBI)

suppression. Such structure is also named FD receiver [20] since all baseband

processes are operated in the frequency domain as shown in Fig. 2-1(b). To make an

FD receiver function well in practices, a reliable FD symbol synchronization is

necessary. Yet, this technique is difficultly ported to most broadband standards, e.g.,

IEEE 802.11 and 15 series, because those algorithms perform sample-by-sample search for correlation peak within the sliding window. In contrast, FD ADC transforms a segment of continuous time-domain signal to a set of frequency coefficients. Therefore, a symbol rate symbol synchronizer that processes signals in the frequency domain is needed for the FD receiver architecture.
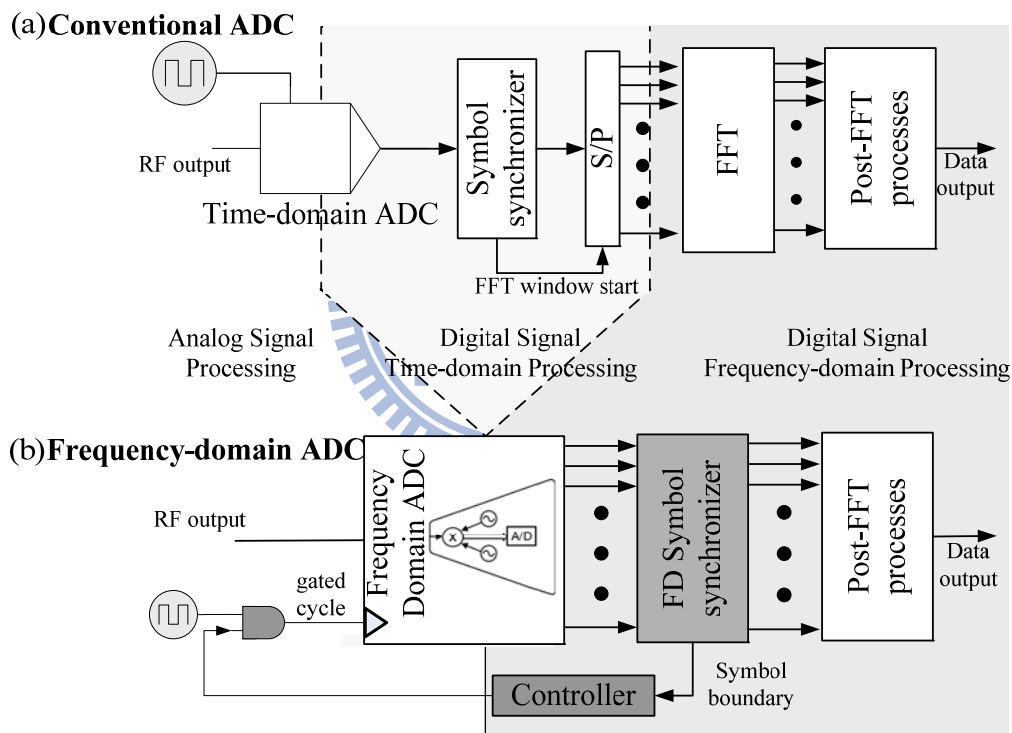
Figure 2-1: The block diagram of OFDM receivers: (a) using the conventional ADC, and (b) using the FD ADC.

To the best of our knowledge, so far no FD symbol synchronizer has been built for FD-OFDM receivers. This work develops a low-complexity sequential searcher in

a 4x4 MIMO-OFDM modem with IEEE 802.11a/n [3], [5] compatibility for the robust symbol synchronization using FD-ADC techniques. Only simple matched filter detection with TD preambles is required to detect the correct symbol timing over the frequency domain. Moreover, an all-digital semi-synchronous clock generator (SSCG) is proposed without PLLs to make high-speed inner clocking much easier in VLSI implementations, so that a shared architecture can work efficiently. By using an in-house 65-nm CMOS library, our all-digital SSCG only requires 3.03 gates. To build in a 4x4 FD MIMO-OFDM modem, the total gate count of the proposed sequential searcher is 84.881K and the power consumption at 1.0 V supply voltage is 5.2 mW. In conclusion, the proposed sequential searcher for robust symbol synchronization is attractive to very high throughput (VHT) wireless LAN (IEEE 802.11 ac/ad) [52] and Multi-Gbps WPAN (IEEE 802.15.3c) [53] specifications implemented using FD-ADC techniques.

The organization of this chapter is described as follows. Section 2.1 introduces the technology of FD ADC. Section 2.2 depicts the system model and the problem statement. Section 2.3 addresses the algorithm of the proposed sequential searcher for FD symbol timing synchronizations. Section 2.4 shows the performance evaluations of SISO- and 4x4 MIMO-OFDM systems and also gives a comparison with other methods. Section 2.5 then presents the low-complexity VLSI architecture and

implementation results. Finally, conclusions are given in Section 2.6.

2.1 Frequency-Domain Analog-to-Digital Conversion

2.1.1 Basic Concept

Fig. 2-2 displays the block diagram of FD ADC. FD ADC projects the received signal $r(t)$ over the complex exponential functions to a set of N_b basis functions such that the frequency coefficients $\mathbf{R}'[n]$ can be obtained via sampling of the continuous-time signal spectrum at the frequencies $\{F_n\}_{n=0}^{N_b-1}$.

$$\mathbf{R}'[n] = \int_0^{T_c} r(t) e^{-j2\pi F_n t} dt \qquad (2.1)$$

where $n = 0 \cdots N_b - 1$. Each $\mathbf{R}'[n]$ outputted by the sampler is then quantized by an individual quantizer Q_n with associated bit resolutions to generate a digital word $\mathbf{R}[n] = Q_n(\mathbf{R}'[n])$. To avoid discrete-time aliasing, the frequency sample spacing $\Delta F = F_n - F_{n-1}$ needs to follow $\Delta F \leq (1/T_c)$, and the optimal number of frequency coefficients necessary to provide fully sampling over the signal spectrum of bandwidth W should be larger than the time-bandwidth product WT_c. Thus, the condition of the optimal number of frequency coefficients N_{opt} is given by

$$N_{opt} = \lceil W / \Delta F \rceil \geq \lceil WT_c \rceil \qquad (2.2)$$

where $\lceil \cdot \rceil$ denotes ceil function. Clearly, the FD ADC provides N frequency samples every T_c seconds. Compared with conventional ADC operated at $1/T_s$ sampling speed (T_s is the sample duration), FD ADC samples with the relaxed rate of a factor T_c/T_s at the cost of N_b parallel devices (i.e. N_b multipliers, integrators and ADCs in Fig. 2-2).
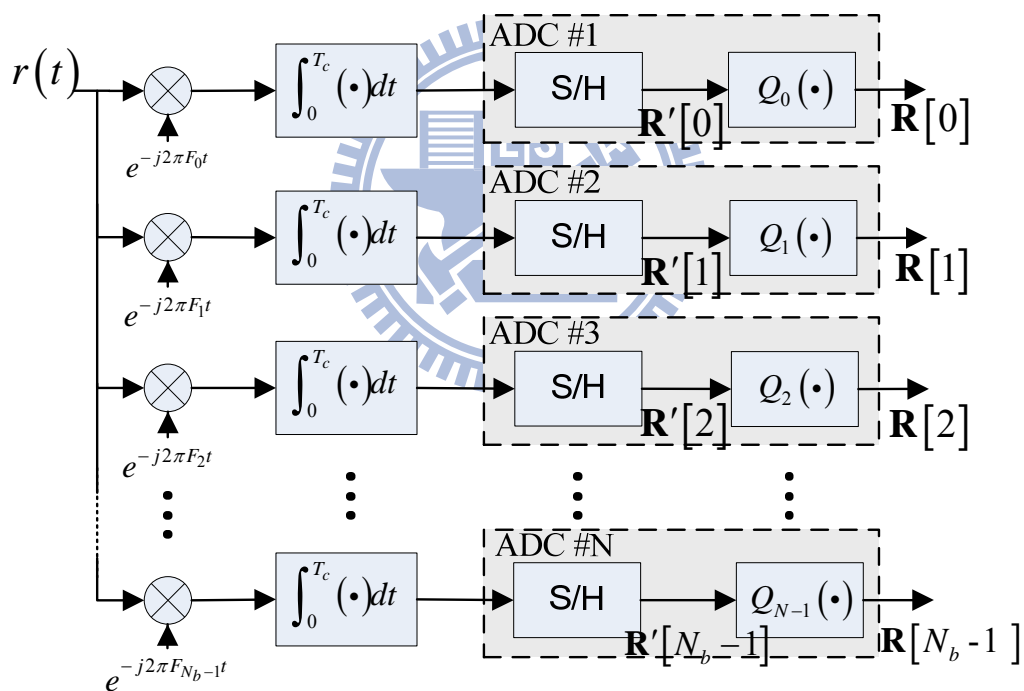
Figure 2-2: FD-ADC block diagram [20]

2.1.2 OFDM Receiver Based on FD ADC

For an OFDM system, T_c can be set to the OFDM symbol period T_{symbol}, which makes N_b equal to the number of subcarrier N_S. However, it might be infeasible to let the conversion-time T_c equal to the duration of OFDM signal T_{symbol} if the OFDM system employs large number of subcarrier. The system becomes impractical due to the complex implementation of too many parallel devices. To reduce the number of coefficients N used in FD-ADC based OFDM systems, the method of segmentation of the OFDM signal is investigated in research [20], which discusses the case of $T_c = T_{symbol}/M_s$ (M_s is the segmentation number). Let OFDM signal x(t) define as

$$x(t) = \sum_{s=0}^{N_s-1} a_s e^{j2\pi f_s t}, \qquad 0 \le t \le T \tag{2.3}$$

where a_s is the data modulated at s-th subcarrier tone. In order to reflect the effect of segmenting the signal x(t) into M_s time-slots, the following window signals is defined as

$$w_m(t) = \begin{cases} 1, & mT_c \le t < (m+1)T_c \\ 0, & \text{elsewhere} \end{cases} \tag{2.4}$$

$$x_m(t) = w_m(t) x(t) \tag{2.5}$$

where m= 0, $\cdots$, M_s-1. Then, the Fourier transform of $x_m(t)$ can be derived as [20]

$$\begin{aligned} X_m(F) &= F\{x_m(t)\} \\ &= \sum_{s=0}^{N_s-1} a_s \frac{\sin(\pi T_c(F - f_s))}{\pi(F - f_s)} e^{-j\pi T_c(2m+1)(F-f_s)} \end{aligned} \tag{2.6}$$

where $F\{\cdot\}$ means the operation of Fourier transform. To detect the transmitted symbols $a_s \mid_{s=0}^{N_s-1}$ in the receiver side, the matched filter scheme can be used in time domain as

$$
\begin{aligned}
\overline{a}_s &= r(t) * p_s(t)\mid_{t=T} \\
&= \int_0^T r(\tau) p_s(T-\tau) d\tau
\end{aligned}
\tag{2.7}
$$

Let the channel frequency response is $H(f)$ and assume the channel is flat within each sub-band. Then, the matched filter impulse response is given by

$$
\begin{aligned}
p_s(t) &= H^*(f_s) x_s^*(T-t) \\
&= H^*(f_s) e^{j2\pi f_s t}
\end{aligned}
\tag{2.8}
$$

where $x_s(t) = e^{j2\pi f_s t}$ is the carrier at frequency f_s. Let $p_s(T-t)$ is $g_s^*(t)$. The segmented signals can be expressed as

$$
r_m(t) = r(t) w_m(t)
\tag{2.9}
$$

$$
g_{s,m}(t) = g_s(t) w_m(t)
\tag{2.10}
$$

Then, the $\overline{a}_s$ can be rewritten as

$$
\begin{aligned}
\overline{a}_s &= \sum_{m=0}^{M_s-1} \int_{mT_c}^{(m+1)T_c} r(\tau) g_s^*(\tau) d\tau \\
&= \sum_{m=0}^{M_s-1} \int_{-\infty}^{\infty} r_m(\tau) g_{s,m}^*(\tau) d\tau
\end{aligned}
\tag{2.11}
$$

To express the matched filter operations in the frequency-domain, the above equation can be applied Parseval's theorem leading to [20]

$$\bar{a}_s = \sum_{m=0}^{M_s-1} \int_{-\infty}^{\infty} r_m(\tau) g_{s,m}^*(\tau) d\tau$$

$$= \sum_{m=0}^{M_s-1} \int_{-\infty}^{\infty} R_m(F) G_{s,m}^*(F) dF \qquad (2.12)$$

$$\approx \sum_{m=0}^{M_s-1} \Delta F_c \sum_{n=0}^{N_b-1} R_m(F_n) G_{s,m}^*(F_n)$$

where $R_m(F)\big|_{n=0}^{N_b-1}$ and $G_{s,m}(F_n)\big|_{n=0}^{N_b-1}$ are the samples from the spectrum of $r_m(t)$

and $g_{s,m}(t)$, respectively. A good approximation of the above equation can be

obtained if the conversion frequency spacing ΔFc avoids discrete time aliasing and

samples are taken only in the frequency band of interest where most of the signal

energy is concentrated. If the number of spectrum samples N_b satisfies Equaltion (2.2)

which avoids discrete-time aliasing and makes the error in (20) negligible, then the

probability of error associated with this receiver will be the same probability of error

of a conventionally implemented OFDM system [20]. In addition, $G_{s,m}^*(F_n)$ needs to

be estimated from channel frequency response $H(f)$, which is can be estimated by

[20]

$$\hat{H}(f_s) = \frac{\sum_{i=0}^{I-1} a_{s,i}^* \tilde{a}_{s,i}}{\sum_{i=0}^{I-1} |a_{s,i}|^2} \qquad (2.13)$$

where I means constant channel blocks number. Then $G_{s,m}(F_n)$ is derived as [20]

$$G_{s,m}(F) = F\{g_{s,m}(t)\}$$

$$= H(f_s) \frac{\sin(\pi T_c(F-f_s))}{\pi(F-f_s)} e^{-j\pi T_c(2m+1)(F-f_s)} \qquad (2.14)$$

Finally, the block diagram of FD-ADC based OFDM receiver is shown in Fig. 2.3.
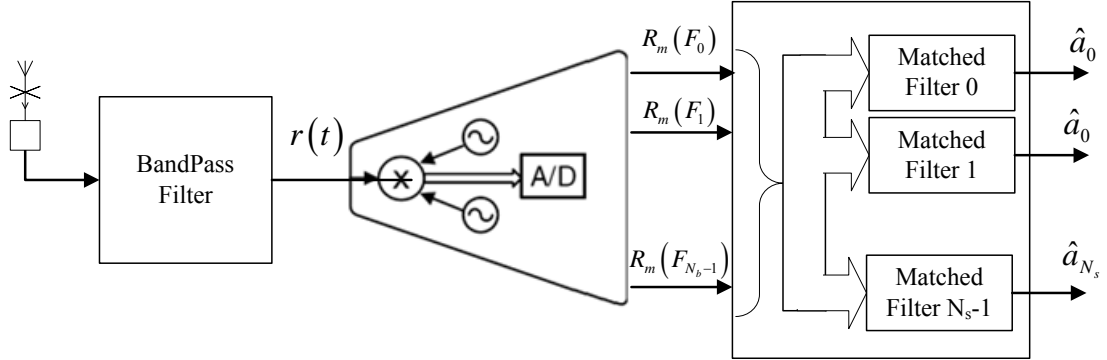
Figure 2-3: Block diagram of FD-ADC based OFDM receiver [20]

2.1.3 Frequency Offset and Phase Noise

Let $\theta(t) = 2\pi\delta\bar{f}t + \theta$ and $\Phi_n(t) = 2\pi\delta f_n t + \Phi_n$ where $\delta\bar{f}$ and δf are the frequency offsets. In order to investigate the effect of frequency offset and phase noise on the performance of the FD receiver, the received signal is rewritten as

$$r(t) = \left(\sum_{s=0}^{N_s-1} a_s H(f_s) e^{j2\pi f_s t} \right) e^{j\theta(t)} + z(t) \tag{2.15}$$

and the local oscillators $O_n(t)|_{n=0}^{N_s-1}$ are defined as

$$O_n(t) = e^{-j2\pi F_n t} e^{j\xi_n(t)} \tag{2.16}$$

Then, the frequency samples $R_m(F_n)|_{n=0}^{N_b-1}$ are rewritten as [20]

$$R_m(F_n) = \int_{-\infty}^{\infty} r_m(t)O_n(t)dt$$

$$= \sum_{s=0}^{N_s-1} H(f_s)a_s \int_{-\infty}^{\infty} e^{-j2\pi(F_n-f_s)t}w_m(t)e^{j(\theta(t)+\xi_n(t))}dt \qquad (2.17)$$

$$+ \int_{-\infty}^{\infty} z_m(t)e^{-j2\pi F_n t}e^{j\xi_n(t)}dt$$

when only frequency offset is taken into account, the above expression reduces to

$$R_m(F_n) = \sum_{s=0}^{N_s-1} H(f_s)a_s e^{j(\theta+\xi_n)}G_{s,m}\left(F_n - \left(\delta f_n + \delta\overline{f}\right)\right)dt + \tilde{Z}_m(F_n) \qquad (2.18)$$

where $\tilde{Z}_m(F_n) = \int_{-\infty}^{\infty} z_m(t)e^{-j2\pi F_n t}e^{j\xi_n(t)}dt$ Thus, frequency offset introduces a constant complex phase equal to $(\theta + \xi_n)$ and an offset in the frequency sample equal to $(\delta f_n + \delta\overline{f})$. The frequency estimation in FD ADC is detailed in the literature [21].

2.1.4 The Advantages and Disadvantages of FD ADC

As the bandwidth of the OFDM signal is increased to achieve higher data rates or to accommodate more users, the time-domain sampling approach of the conventional OFDM receiver poses serious challenges to the sampling speed requirement of the ADC. The FD ADC approach has the advantage of sub-Nyquist sampling rate, enabling parallel digital signal processing, flexibility, and scalability in receiver design, making it an attractive option for applications of high speed multi-mode wireless communication systems.

Sampling at frequency domain provides the several main advantages: 1) relaxation of ADC sampling rate; 2) possibility of optimally allocating the available

number of bits for ADC; 3) easily suppression of narrowband interference. Due to the lower sampling rate, FD ADC is more tolerant to the front-end distortions, e.g., clock jitter [22], carrier frequency offset and phase noise [20]. For example, the research [22] shows that FD-ADC receiver can tolerate up to 5-ps$_{rms}$ clock jitter while the conventional ADC requires 0.5-ps clock jitter at the same specifications.

Both of the analog front-end and digital complexities of FD-ADC approach are marginally higher than that of the conventional approach of FFT with time-interleaved ADC [21], [22]. However, the complexity overhead is not a critical drawback, and it is justified by the critical savings in the clock generation, routing, and driving circuits [22]. There are two main drawbacks for FD ADC architecture. The first one is the noise added by the N_b filters could degrade the overall receiver performance [22]. The second drawback is that too little literature can be referred for the issues of synchronization and distortion compensations when people considers to build a practical OFDM system based on FD-ADC technology. It is because many synchronizations and distortion compensations processes, including sample and symbol timing recovery, and compensation of I/Q imbalance, are developed in time-domain and may fail to work in frequency domain. Currently, the designs of multicarrier and direct spread systems based on FD-ADC architecture can be referred to the research [19].[21] and [23], respectively.

2.2 System Assumptions and Problem Statement

2.2.1 System Assumptions

The packet structure, depicted in Fig. 2-4, is assumed to contain several preambles without any guard interval (GI) in the packet header. The preamble and its cyclic shift versions are also assumed to have good autocorrelation and low cross-correlation with other shift versions. Let the preamble be denoted as $c \triangleq \{c[0], c[1], \cdots, c[L-1]\}$ with L samples length. Then, the baseband-equivalent model of the preamble is given by

$$c(t) = \left[\sum_{i=0}^{L-1} c[i] \cdot \Pi(t - iT_s) \right] \otimes f_T(t) \tag{2.19}$$

where $\otimes$ is the denotes continuous time convolution, $\Pi(t)$ is a function of BPSK modulation, and T_s is the sample period of preambles. To be consistent with the spectrum mask, $c(t)$ is passed through the transmission filter $f_T(t)$ (shaping filter). The duration of one preamble T_p, is derived from T_s by $T_p = LT_s$. The signal $c(t)$ is then transmitted through a multipath frequency-selective fading channel $h(t)$, e.g., IEEE random phase and Rayleigh fading SISO channel [55] and IEEE TGn MIMO channel [56].

At the receiver, the signal is first passed through the RF filter and then down converted into baseband signal. After the automatic gain control (AGC), the baseband signal of received preambles is given by

$$r(t) = \sigma(t) \bullet [c(t) \otimes h(t) \otimes f_R(t)] \bullet e^{j2\pi \cdot f_{CFO} \cdot t} + z(t) \tag{2.20}$$

where $\sigma(t)$ is an AGC compensated error, f_{CFO} is the carrier frequency offset, $w(t)$ represents additive white Gaussian noise (AWGN), $f_R(t)$ is the lowpass equivalent receiver filter response, and $h(t)$ is the channel response of multipath frequency-selective fading. FD ADC transforms a segment of continuous time-domain received signal into a vector of digital frequency coefficients by [19]

$$\mathbf{R}_q[n] = \int_0^{T_c} r(t + qT_c) e^{-j2\pi F_n t} dt \tag{2.21}$$

where $n = 0 \cdots N_b - 1$, $\mathbf{R}_q \triangleq [R_0, R_1, \cdots, R_{N_b-1}]^T$ is the frequency coefficient vector with the frequencies of $\{F_n\}_0^{N_b-1}$, T_c is the segment duration, and q is the segment index. T_c can be equal to the whole preamble period T_p or a segment of preamble, i.e. $T_c = T_p / M_s$. Due to the preamble period is usually shorter then an OFDM symbol, T_c is assumed to be equal to the preamble period T_p to simplify the following derivations. Hence, N_b is set to be equal to the the number of preamble samples L to avoid timing aliasing [20].
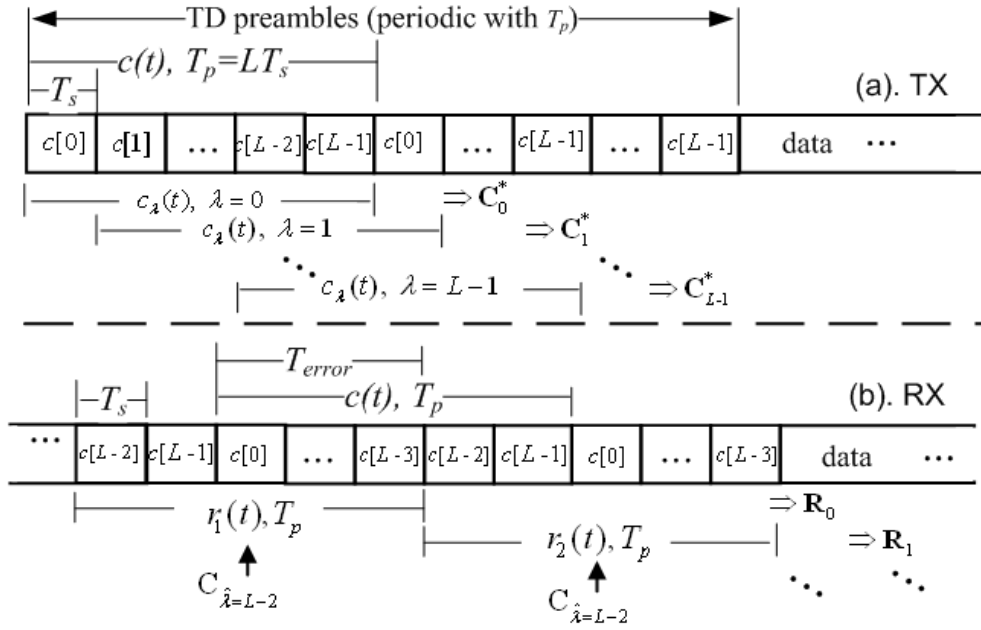
Figure 2-4: Definitions of data patterns: (a) TX preamble patterns; and (b) FD

signal vectors and an estimated example of $\lambda = L-2$ in RX.

2.2.2 Matched Filter Detection in FD Receiver

In practice, the matched filter detection is important to timing synchronization and

data detection for many communication systems. It can be efficiently realized in the

FD receiver structure, too. For example, the matched filter metric Φ between the

time segment of received signal $\bar{r}(t)$ (duration of T_p) and the preamble $c(t)$ can

express in continuous time domain as the conventional form of

$$\Phi = \int_{t_{ini}}^{t_{ini}+T_p} \bar{r}(t) c^*(t) dt \tag{2.22}$$

where $(\bullet)^*$ indicates complex conjugate, t_{ini} is the initial time to calculate matched

filter. With the help of the Parsevals' theorem [54], Equation (2.22) can be derived from the frequency-domain signals as

$$
\begin{aligned}
\Phi &= \int_{t_{ini}}^{t_{ini}+T_p} \bar{r}(t) c^*(t) dt \\
&= \int_{-\infty}^{\infty} \bar{R}(F) C^*(F) dF
\end{aligned}
\tag{2.23}
$$

where $\bar{R}(F)$ and $C^*(F)$ represent continuous frequency domain signals generated by Fourier transform of $\bar{r}(t)$ and $c^*(t)$, respectively. However, the output of FD ADC are N_b discrete frequency samples $\{\bar{\mathbf{R}}[n]\}_{n=0}^{N-1}$ from the spectrum of $\bar{r}(t)$. Therefore, Equation (2.23) is approximated as

$$
\begin{aligned}
\Phi &= \int_{-\infty}^{\infty} \bar{R}(F) C^*(F) dF \\
&\approx \Delta F_c \sum_{n=0}^{N_b-1} \bar{\mathbf{R}}[n] \mathbf{C}^*[n]
\end{aligned}
\tag{2.24}
$$

where $\{\mathbf{C}^*[n]\}_{n=0}^{N_b-1}$ is the set of frequency samples from the spectrum of $c^*(t)$. Note that the truncate error in Equation (2.24) can be negligible [20] and the discrete-time aliasing can be avoided when the number of frequency samples N_b is optimal, e.g., $N \geq \lceil WT_c \rceil$ in Equation (2.2). Therefore, the matched filter function can be adopted in the FD receiver as well as the conventional receiver.

2.2.3 Problem Statement

With the conventional TD ADC, most algorithms find the symbol boundary by serial search with a sliding window over the consecutive received signal samples. However,

FD ADC outputs the frequency-domain digital signals from the received signal segments of continuous time-domain signal in parallel. Without sampling index in FD receivers, the serial search is a failure because it cannot get any timing information in time domain. Meanwhile, directly utilizing the matched filter function with the frequency samples of one received signal segment might be a solution for the synchronization with FD ADC. However, it still could obtain a poor synchronization performance in the frequency selective channel [32]. To the best of our knowledge, so far no existing FD symbol synchronizer has been built for FD-ADC approaches.

Considering a low complexity design and implementation for FD synchronizer with FD ADC architecture, one way is to use a simple metric computation and reduce the detection space based on algorithm level. The other way is to decrease the gate counts of VLSI implementations via shared architectures, i.e. shared hardware by high-speed inner clocking without the help of PLLs. Finally, the proposed solution must be workable, reliable and robust at low SNR (i.e. SNR $\leq$ 10 dB) due to many broadband standards provide low-rate, medium-rate and high-rate transmissions for different environments (SNR).

2.3 The Proposed FD Symbol Synchronization

2.3.1 Sequential Search

Since the transmitted preamble repeats periodically as shown in Fig. 2-4, any time segment of duration T_p within the transmitted preambles can be defined as

$$c_\lambda(t) = \left[\sum_{i=\lambda}^{L-1+\lambda} c\left[(i)_L \right] \cdot \Pi(t - (i)_L T_s) \right] \otimes f_T(t)$$

$$\lambda T_s \le t < (\lambda + 1) T_s, \quad 0 \le \lambda < L-1$$

(2.25)

where $\lambda = 0, \cdots, L-1$ is the preamble pattern index, and $(\bullet)_L$ means "modulo L". The segment is one of the L possible preamble patterns where $c_0(t)$ is the preamble with zero shift, and the other $c_\lambda(t)$ are the preambles with cyclic shift of λ samples.

On the receiver side, the continuous time-domain received signals can be segmented into consecutive signal segments. Let q be the segment index and the corresponding segment is defined as

$$r_q(t) = r(t) w_q(t)$$

(2.26)

where

$$w_q(t) = \begin{cases} 1, & qT_p \le t < (q+1)T_p \\ 0, & \text{elsewhere} \end{cases}$$

(2.27)

Because preambles have good correlation property, the similarities between each received signal segment $r_q(t)$ and each $c_\lambda(t)$ can be obtained via the matched filter

output

$$\Phi(q,\lambda) = \int_{t_{ini}}^{t_{ini}+T_p} r_q(t) c_\lambda^*(t) dt \tag{2.28}$$

According to the Equation (2.28), $\Phi(q,\lambda)$ can also be calculated in frequency

domain being

$$\Phi(q,\lambda) = \Delta F_c \sum_{n=0}^{N-1} \mathbf{R}_q[n] C_\lambda^*[n] \tag{2.29}$$

where $\mathbf{R}_q[n]$ and $\mathbf{C}_\lambda^*[n]$ are one of the frequency coefficients from the spectrums

of $r_q(t)$ and $c_\lambda^*(t)$, respectively. $\{\mathbf{R}_q[n]\}_{n=0}^{N-1}$ is generated by FD ADC for each

segment $q = 0,1,\cdots$, but $\{\mathbf{C}_\lambda^*[n]\}_{n=0}^{N-1}$ can be pre-calculated by Fourier transform and

pre-stored in the memory. When all preamble patterns are correlated with the q-th

received signal segment, the maximum likelihood (ML) detection of segment q is

given by

$$\hat{\lambda} = \arg \max_{0 \le \lambda \le L-1} |\Phi_{q,\lambda}| \tag{2.30}$$

According to the $\hat{\lambda}$, the timing error T_{error} between the initial time of current received

segment and the correct symbol starting time of the corresponding preamble can be

obtained by $T_{error} = \hat{\lambda} T_s$ (Fig. 2-4). If the q-th segment is initial at t_1, the symbol

starting time is $t_{ss} = t_1 - T_{errors}$. Note that two symbol starting times t_{ss}' and t_{ss}'' are

equivalent under the condition of $|t_{ss}' - t_{ss}''| = \ell T_p$, where ℓ is an non-negative

integer.

Since the matched filter detection is not reliable in multipath fading, the symbol

timing derived from the ML detection of received signal segments might not be

equivalent. It is difficult to extract the correct symbol starting time via the detection

results of those segments. In order to solve this problem, each segment's detection can

be treated as a path element to form a search path that starting from an initial

detection result of the beginning segment. Then, the sequential search described in the

following is proposed to look for the path that consists of the correct detection result

of each segment. To explain more precisely, the definition of a path with K segments

is firstly given as follows

$$\rho \triangleq \lambda_0, \lambda_1, \cdots, \lambda_{K-1} \tag{2.31}$$

where the path element λ_q, $0 \leq q < K$ is the detection result of preamble pattern

index in q-th segment. If λ_q is assumed to be a correct detection result, the

reasonable pattern index of λ_{q+1} could be give by

$$\lambda_{q+1} = \lambda_q + \left(\left\lfloor D_{offset} / T_s \right\rfloor \right)_L, \quad 0 \leq q < K \tag{2.32}$$

where D_{offset} is timing offset between the end time of q-th segment and initial time of

(q+1)-th segment. Since q-th and (q+1)-th segments are consecutive in this chapter,

D_{offset} is equal to zero. Substituting D_{offset}=0 into Equation (2.32), the search finds the

path that in compliance with the following constraint (the first constraint)

$$C1: \lambda_{q+1} \text{ is equal to } \lambda_q, \quad 0 \leq q < K \tag{2.33}$$

As a result, the proposed search becomes to find the path as

38

$$\rho_{\lambda'} \triangleq \underbrace{\lambda', \lambda', \cdots, \lambda'}_{K \text{ elements}} \tag{2.34}$$

where λ' is the pattern index of first path element. In order to reflect the overall

similarity of $c_{\lambda'}(t)$, each matched filter output between $c_{\lambda'}(t)$ and $r_q(t)$ are sum

up to get the corresponding path metric $\Psi(\rho_{\lambda'})$, which is formulated by

$$\Psi(\rho_{\lambda'}) = \sum_{q=0}^{K-1} |\Phi(q, \lambda')| \tag{2.35}$$

Therefore, the pattern index of the allowable path leading to the path metric maximum

is the final detection result, which is given by

$$\hat{\lambda} = \arg \max_{\rho_{\hat{\lambda}} \in \Lambda} \Psi(\rho_{\hat{\lambda}}) \tag{2.36}$$

where Λ is the set of allowable paths. As mentioned above, T_{error} can be obtained

by $T_{error} = \hat{\lambda} T_s$. Then, FD ADC can be gated with $T_p - T_{error}$ to transform the

received signals into the frequency domain correctly.

2.3.2 Complexity Reduction and Performance Enhancement

In order to reduce the number of search paths for calculating the path metric in

Equation (2.36) and to avoid the case that local maximum (maximum correlation

metric of one certain segment) dominates the global maximum (maximum total path

metric), the following two constraints are developed based on the criteria of matched

filter outputs to limit the search of pattern index in each segment. Firstly, the preamble

patterns with top-Z largest matched filter outputs are obtained by the second

constraint defined as follows

$$C2 : \Phi\left(q,\lambda\right) \geq \Phi\left(q,\overline{\lambda}\right), \; 0 \leq q < K, 0 \leq \lambda < L \tag{2.37}$$

where $\overline{\lambda}$ is the pattern index with Z-th ($Z<L$) largest matched filter outputs in q-th

segment. Let $\mathbb{C}_q$ be the set of preamble patterns that follows $C2$ in q-th segment.

When the channel condition is good or SNR is high, most of the patterns in the $\mathbb{C}_q$

could have very small matched filter outputs because the matched filter detection of

matched preamble pattern is usually a peak value among all of the matched filter

outputs. Therefore, the third constraint defined a correlation threshold according to

the largest matched filter output is give by

$$C3 : \Phi\left(q,\lambda\right) \geq th \cdot \Phi\left(q,\tilde{\lambda}\right), \; 0 \leq q < K, 0 \leq \lambda < L, 0 < th < 1 \tag{2.38}$$

where $\tilde{\lambda}$ is the pattern index with maximum correlation value in q-th segment.

According to the above two constraints, the confidence of the pattern $c_\lambda(t)$ in the

q-th segment is defined as

$$conf_{q,\lambda} = \begin{cases} 1, & C2 \text{ and } C3 \text{ are } true \\ 0, & \text{elsewhere} \end{cases} \tag{2.39}$$

Let $\left(\lambda_q, \lambda_{q+1}\right)$ be the element pair of each two neighbor elements λ_q and λ_{q+1} in

the same path. Then, $\left(\lambda_q, \lambda_{q+1}\right)$ is called valid pair when the following condition is

satisfied.

$$C1 \text{ is } true \text{ and } conf_{q,\lambda_q} = 1 \text{ and } conf_{q+1,\lambda_{q+1}} = 1 \tag{2.40}$$

The search set Λ in Equation (2.36) is redefined as the set of survivor paths, in which the path elements are in compliance with the condition of valid element pair. The number of survivor paths is less then or equal to Z since the constraint $C2$ limits the candidate patterns in each segment.

To more clearly describe the behavior of the proposed sequential search, Fig. 2-5 gives a case example which includes invalid element pairs and the survivor paths. The path with three segments is $\rho_0 \triangleq (\lambda_0, \lambda_1, \lambda_2)$, and $\hat{\lambda} = 0$ is assumed as the correct estimation result. The pattern indexes of both black and gray nodes represent the cases which violate the constraints of $C2$ and $C3$, respectively. The node pairs connected with dash lines are cases of invalid element pair, i.e. the pairs of (λ_0, λ_1) is invalid in the cases of $(3,2)$ and $(3,3)$ because of the violations of constraints $C1$ and $C3$, respectively; the pair of (λ_1, λ_2) is invalid in the case of $(2,2)$ due to the violation of constraints $C2$. Two survivor paths ($\rho_0 = (0,0,0)$ and $\rho_1 = (1,1,1)$) are shown in Fig. 2-5, where the best survivor path is ρ_0 because of $\Psi(\rho_0) = 765\ (210+245+310)$ is larger than $\Psi(\rho_1) = 646\ (220+205+221)$. Then, the estimation result is $\hat{\lambda} = 0$. If the detection is only decided according to the matched filter outputs of 0-th segment, the detection result will be $\hat{\lambda} = 3$ since pattern index three has the largest matched filter output. However, it is a wrong estimation.

Finally, the computing complexity of the proposed algorithm is analyzed as

follows: the matched filter of each λ in Equation (2.10) needs L complex

multiplications and (L-1) complex additions, $C2$ requires $L \cdot \log_2 L$ comparisons and

$C3$ needs both Z real multiplications and comparisons for each time segment. For the

path length of K, the total computing complexity includes ($4 \cdot K \cdot L^2 + K \cdot Z$) real

multiplications, ($5 \cdot K \cdot L^2 - 2 \cdot K \cdot L$) real additions, and ($K \cdot (L \cdot \log_2 L + Z + 1) - 1$)

comparisons, which are all derived from K matched filter operations ($4 \cdot K \cdot L^2$ real

multiplications and $5 \cdot K \cdot L^2 - 2 \cdot K \cdot L$ real additions, assume one complex multiplication

needs four real multiplications and three real additions), (K-1) rule checks of C1 ((K-1)

comparisons), K rule checks of $C1$ and $C2$ ($K \cdot (L \cdot \log_2 L + Z)$ comparisons and $K \cdot Z$ real

multiplications), and the summation of the path metric ($Z \cdot (K$-1) real additions).

Obviously, the overall computing complexity is dominated by the matched filter

operations, and therefore, the implementation complexity of matched filter detection

will be discussed via a proposed shared architecture in Section 2.5.

$q = 0 \; (\lambda_0)$ $q = 1 \; (\lambda_1)$ $q = 2 \; (\lambda_2)$

$\lambda = 0$ ◯━━━━━━◯━━━━━━◯

$\Phi(0,0) = 210$ $\Phi(1,0) = 245$ $\Phi(2,0) = 310$

$\lambda = 1$ ◯──────◯──────◯

$\Phi(0,1) = 220$ $\Phi(1,1) = 205$ $\Phi(2,1) = 221$

$\lambda = 2$ ◯──────◯── ── ── ●

$\Phi(0,2) = 190$ $\Phi(1,2) = 220$ $\Phi(2,2) = 100$

$\lambda = 3$ ◯── ── ── ●── ── ── ●

$\Phi(0,3) = 270$ $\Phi(1,3) = 150$ $\Phi(2,3) = 180$

Invalid pairs

survivor paths

$\lambda = L - 1$ ●   ◐   ●

$\Phi(0, L-1) = 145$ $\Phi(1, L-1) = 20$ $\Phi(2, L-1) = 70$
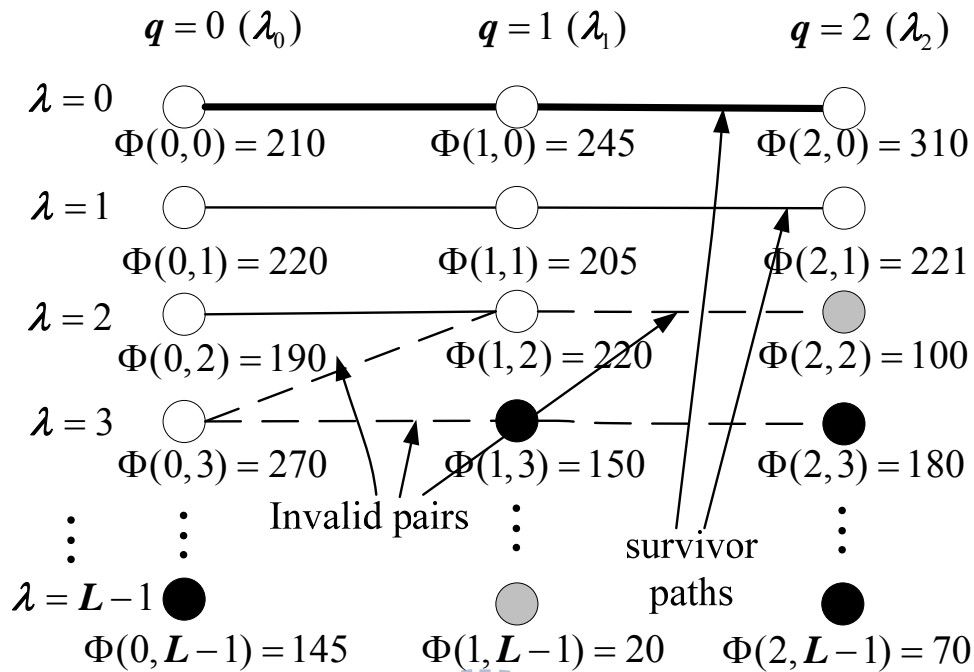
Figure 2-5: Example of the trellis diagram with path length K=3. The black and gray nodes are assumed to violate the constraints of $C2$ and $C3$, respectively. The dash lines are some cases of invalid element pairs in the same path

2.3.3 Algorithm Identification Step

Figure 2-6 presents the flowchart of the proposed sequential search. The detection of each received signal segment is first performed via performing matched filter with each preamble pattern. Then, some patterns with small matched filter outputs are discarded for the following path search. When the number of detected segments reaches to the defined path length, the sequential search is performed to determine the

survivor paths in compliance with Equation (2.40). From those survivor paths, the

best path that has the maximum summation of the matched filter outputs of each

segment can be obtained. Finally, the time offset to the next preamble starting time is

got according to the best path index. The identification steps of the proposed

algorithm are summarized as follows:

Step 1) Prepare the detection results of each received signal segments.

    a) **Perform matched filter:** take the input data $\mathbf{R}_q$ (the frequency

        coefficients of q-th received signal segment) generated by FD ADC. For

        each preamble pattern index λ, compute the corresponding matched

        filter outputs according to Equation (2.29).

    b) **Sorting**: sort the matched filter outputs with decreasing order of output

        values.

    c) **Confidence check**: filter out the pattern indexes according to constraints

        of *C2* and *C3*.

    d) Repeat from sub-step a) if the sequence length does not reach.

Step 2) Search best path

    a) **Survivor paths search**: determine the survivor paths according *C1*.

        Calculate the path metric of those survivor paths.

    b) **Best path calculation**: select the best path with path index $\hat{\lambda}$ which

        has the largest path metric (Equation (2.36)).

T_{error} is given by $\hat{\lambda}T_s$, and FD ADC is gated with $T_p - T_{error}$ seconds to start

conversion with the correct symbol timing.

Parallel data in
(From FD ADC)

$\{\mathbf{R}_q[n]\}_{n=0}^{N-1}$

Step 1

Perform matched filter
For each $c_\lambda(t)$
calculate $\Phi(q,\lambda)$ by Eq. (2-29)

Sorting
Sort $\{\lambda\}_{\lambda=0}^{L-1}$ according to $\Phi(q,\lambda)$

Confidence check
Eq. (2-39)

No   Path length $== K$ Yes

Step 2

Survivor paths search
Eq. (2-40)

survivor paths

Best path calculation
Eq. (2-36)

$\hat{\lambda}$

Step 3

FD ADC needs to gated
$T_p - \hat{\lambda}T_s$ seconds
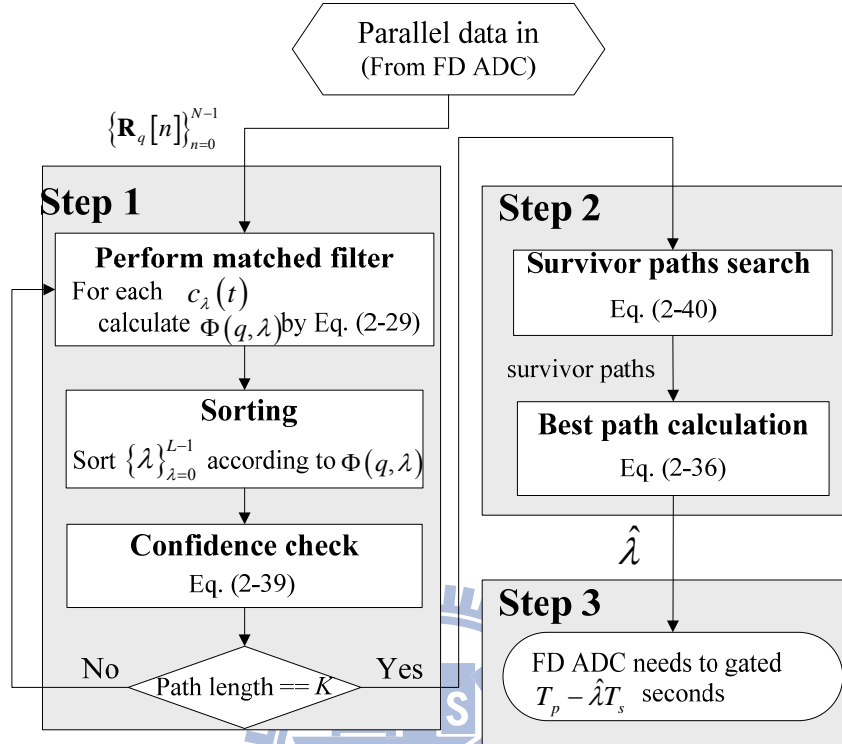
Figure 2-6: The flowchart of the proposed sequential search

2.4 Performance Evaluations

To reveal the feasibility in OFDM systems, our simulations are ported to IEEE 802.11a (SISO OFDM) and IEEE 802.11n/ac (4x4 MIMO OFDM). The default settings of the proposed sequential searcher are L=16, Z=7, K=3. And the performance criterion of boundary detection errors is 2%.

Figure 2-7 plots the synchronization performance of the proposed method in the

IEEE suggested channel models (IEEE fading model [55], IEEE TGn model [56]).

The simulation results indicate that the required SNRs of the acceptable performance

criterion are below 4 dB for all cases of search length K =3. For K=5, that gains 1.5

dB ~ 2.7 dB in both 11a and 11n/ac cases. Due to the diversity gain, the required SNR

of 4x4 MIMO OFDM is much lower than that of SISO OFDM. The simulation results

show that the proposed method can work robustly at low SNR for WLAN

applications. Figure 2-8 gives the simulation results of different frequency offsets

based on the acceptable performance criterion. The results indicate that our

performance only degrades 1% in the carrier frequency offset (CFO) range of ±100

ppm － this method is significantly tolerant to CFO to make initial synchronization

easier and more flexible.

Fig. 2-9 displays the performance comparisons of our method and five existing

algorithms ([24], [26], [29], [31]-[32]) in Channel II model [32], which is a Rayleigh

fading channel model where the first tap has zero delay and the other five taps present

delays uniformly distributed over the interval [0–300ns]. The probability of

synchronization failure with 0.5-dB SNR loss, denoted as $P_{\mathrm{f}}(0.5)$[32], is adopted to

compare with other solutions. From results of Fig. 2-9, it can be observed that at

medium to high SNRs (10≤SNR≤30 dB), the proposed method and the ML methods

that jointly estimates the channel and timing [31]-[32] have similar performances.

However, the proposed method shows its better performance compared to the other methods at low SNR range (i.e. 0≤SNR<10). Our performance gain at low SNRs might come from the utilization of MLSE-based search over three preambles (those compared methods use at most two preambles). Then, we also evaluated the computation complexity of our methods by big-O notation of number of complex multipliers in algorithm level. Those common symbol synchronization algorithms usually perform metric computation per sample in the sliding window of one preamble length. Therefore, the computation complexity is evaluated by the total number of complex multipliers required for the total metric computation. For the case of search path length equals to three ($K=3$), the proposed method needs to perform three times matched filter detections with L preamble patterns, where each detection needs L complex multiplications. Therefore, the computation complexity is $O(3L^2)$. Table 2-1 summarizes the algorithm comparisons in terms of performance, complexity and other system requirements. By utilizing the simpler detection metric and shorter preamble, the proposed method can obtain almost the best performance with lowest computation complexity (the double correlation method has a comparable complexity, but it provides a poor performance in high SNR range). The main cost of our algorithm is to require one additional preamble. (assuming $K=3$ in our method and at most two preambles are used for other symbol synchronization methods). However,

it can be avoided because our method is significantly tolerant of CFO, which makes

initial synchronization easier and more flexible.
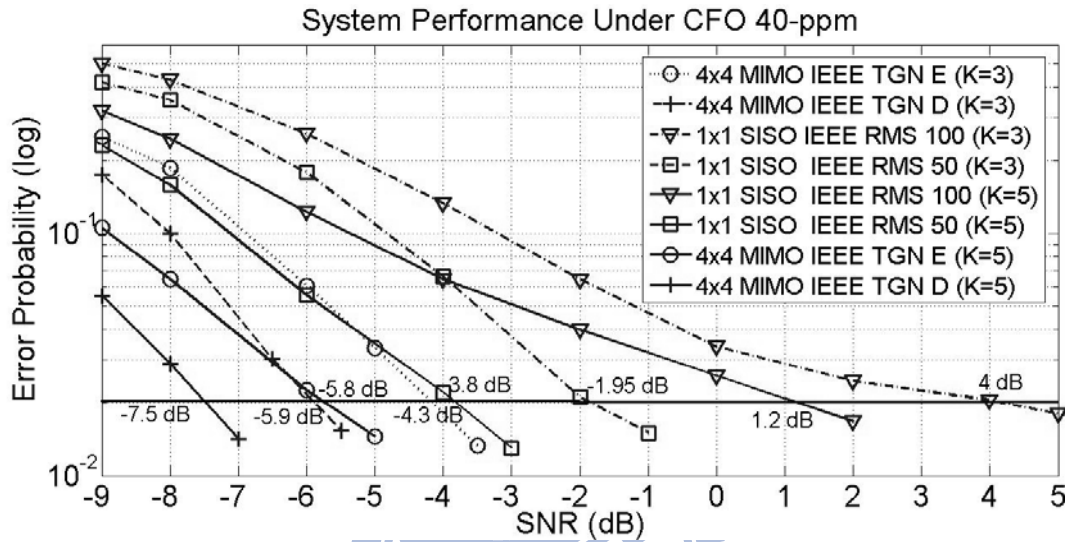
Figure 2-7: Error probability of symbol synchronization in IEEE SISO and

MIMO frequency-selective fading with a CFO of 40 ppm (typical CFO of

IEEE 802.11 series is ±20 ppm)
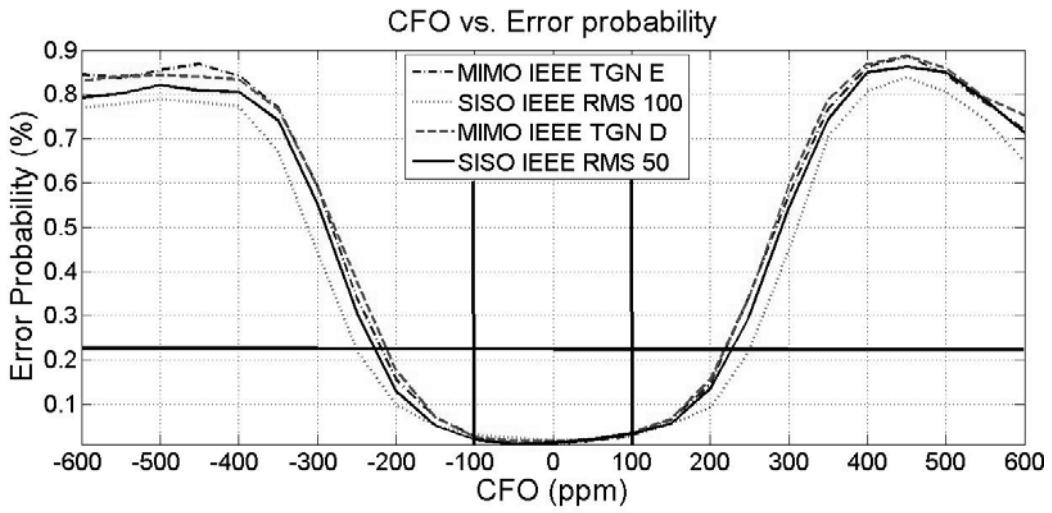
Figure 2-8: Error probability with different CFOs in IEEE and TGn frequency-selective fading with 50-ns and 100-ns RMS delay spreads
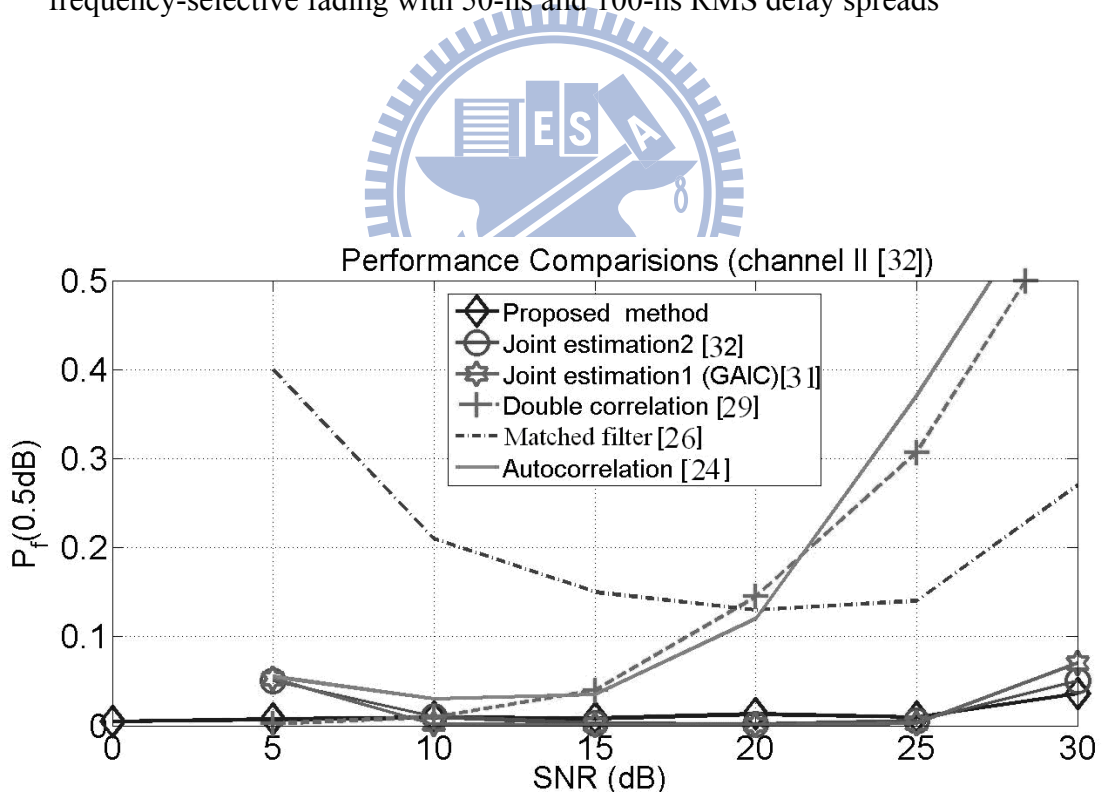
Figure 2-9: Performance comparisons of $P_f(0.5)$ in channel II

Table 2-1 Comparisons of Symbol Synchronization Methods in IEEE 802.11a Systems

	ADC type	Method	Decision rate	Processing domain	System Specs. (IEEE 802)	Preamble length / utilized length (N)	CFO pre-compensation or pre-estimation	Perform. $P_f(0.5)$ at SNR 5dB	Computation Complexity (# of complex multiplier)
[24]	TD	Auto	sample	time	11a	(L) 64/64	rough pre-estimation is assumed	94.5%	$O(L^2)$
[29]	TD	Double	sample	time	11a	(L) 64/64	NO	99.5%	$O(2L^2)$
[26]	TD	Matched filter (Cross)	sample	time	11a	(L) 64/64	pre-estimation is needed	96%	$O(L^2)$
[31]	TD	Joint	sample	frequency	11a	(L) 64/64	-	94.5%	$O(L^2(L+a))$
[32]	TD	Joint	sample	time	11a	(S) 16/16	pre-compensation is assumed	94.5%	$O(S^2(S+b))$
This work	FD	Matched filter + Sequential Search (K=3)	symbol	frequency	11a/n 11 ac	(S) 16/16	NO ($\pm$100 ppm)	99.3%	$O(3L^2)$
Note. (S) means short preamble, and (L) means long preamble in IEEE 802.11a/n/ac									

2.5 Architecture and Implementations

2.5.1 Low-Complexity Architecture

To obtain a low-complexity implementation, the resource shared architecture is

necessary. Firstly, the registers used to store the matched filter outputs must be shared

between each algorithm steps to achieve an efficient utilization. Then, the amount of

basic computation components to perform matched filter and sorting (e.g., complex

multipliers and comparators) are decreased by shared hardware with a high-speed

inner clock. Although the increasing clock rate would cause extra power consumption,

this cost can be omitted since the symbol synchronization is only activated within a

very short period (three preambles) as compared with the duration of whole packet.

The main problem is to realize a low complexity clock generator to solve high-speed

inner clocking.

Following this concept, the VLSI architecture of the proposed sequential

searcher for FD symbol synchronization is illustrated in Fig. 2-10(a), which is adopted

in a 4x4 FD MIMO-OFDM modem to meet IEEE 802.11 a/n specifications (the

system clock is 20 MHz ; the length of short preamble is 16). The sequential searcher

has seven major modules: 1) look up table (LUT); 2) cross-correlator unit; 3) sorter; 4)

candidate filter; 5) registers banks 6) constraints checker; 7) semi-synchronous clock

generator (SSCG). The LUT, implemented by ROM, stores the preamble patterns－

frequency responses of ideal preamble with different delays. To avoid the register

overhead, the shared registers banks are used to replace the internal registers in the

sorter, candidate filter, and constraints checker. There are 21 registers per registers

bank, dominated by constraints checker. Each register inside the bank needs to save a

triple unit including delay index, matched filter output and confidence value. The

matched filter banks include four banks for data flows of four received antennas.

During the period of one short preamble (800ns), each bank adopts four shared

complex multipliers to perform matched filter detection between each

frequency-domain received signal vectors and all delay versions of short preamble

(pre-stored in LUT). In the MIMO case, the matched filter outputs of four data flows

are accumulated to maximize the receiving gain and to merge the following process

into one data flow. By using four shared comparators, sorter reorders the data stored

in registers and inserts the input matched filter result into the corresponding register

immediately when the input matched filter result is generated from matched filter

banks. After each matched filter output between the preamble pattern and the received

signal segment are sorted, the candidate filter decides their confidence value and

saves the preamble patterns with the largest top-seven matched filter outputs into the

registers. When the path length is reached, the survivor paths are found via the

constraint checker, which includes seven (parallel) constraint-check engines to make

the processing latency meet specifications. Figure 2-10(d) displays the structure of

single constraints checking engine, which checks the validity of combination of

current and next segments in the trellis diagram (Fig. 2-10(e)) and accumulates the

matched filter output values. Finally, SSCG (detail the structure in next sub-section)

creates a high-speed inner clocking that is approximate to but larger than 4X system clock.

Since the overall computing complexity is dominated by the matched filter detections, the design of shared complex multipliers in matched filter banks is crucial to the overall implementation complexity and required inner clock speed. Instead of full parallel structure with 16 complex multipliers per matched filter bank, a shared structure of 4 complex multipliers per bank is proposed in Fig. 2-10(b). In contrast with the full parallel structure, the overall complexity of the shared structure is saved by a factor of $4 \cdot Ant_{rx}$ (Ant_{rx} is the receiver antenna number). To overcome the requirement of processing latency, each bank must operate at $\geq 4X$ system clock. Since the critical paths of the proposed architecture are the matched filter banks, the inner clock rate shall also be $\geq 4X$ system clock. According to such inner clock rate, the shared structures of sorter can be further exploited. Due to the sorter processes one element at each time, it acts like an inserter after 16 comparisons with the data stored in the registers. The 16 comparisons can be computed via four comparators in a shared structure of Fig. 2-10(c). At each cycle, the input of matched filter result is compared with four matched filter output values stored in the registers. If the input of matched filter results are larger than the matched filter output value stored in the register, the comparator outputs '1' to the shift register. Otherwise, it outputs '0' to the

shift register. After each four parallel comparisons, the bit array in the shift register

shifts four bits. When all 16 matched filter outputs stored in the register are compared

with the input data (count value reaches to four), the shift register outputs its bit array

as a command word to the control in parallel, and the control then inserts the input

matched filter results into the corresponding registers.

2.5.2 Semi-synchronous Clock Generator

To create high-speed clocking as easy as possible, an all-digital semi-synchronous

clock generator (SSCG), plotted in Fig. 2-11, is built without any analog and

all-digital PLL. The proposed SSCG consists of a divide-by-2 circuit, a time-to-digital

converter (TDC), a programmable divider, a semi-synchronous clocker (SSC), and a

SSC encoder. The divide-by-2 circuit is used to generate a reference clock of 1/2 input

clock to let TDC measure the period of input clock with duty-cycle free. After TDC, a

programmable divider calculates the clock period of a N_f-time high-speed clock ($1/N_f$

times input clock period). This divider is implemented via a shifter (N_f is a power of 2

integer, being 4 in our implementations) and a subtractor to calculate the approximate

clock period of a N_f-time high-speed clock as follows

$$Z_{clk} = \left\lfloor \left(T_{clk} / N_f \right) - \alpha \right\rfloor \tag{2.41}$$

where T_{clk} is the input clock, (N_f is frequency multiplication factor, Z_{clk} is the clock
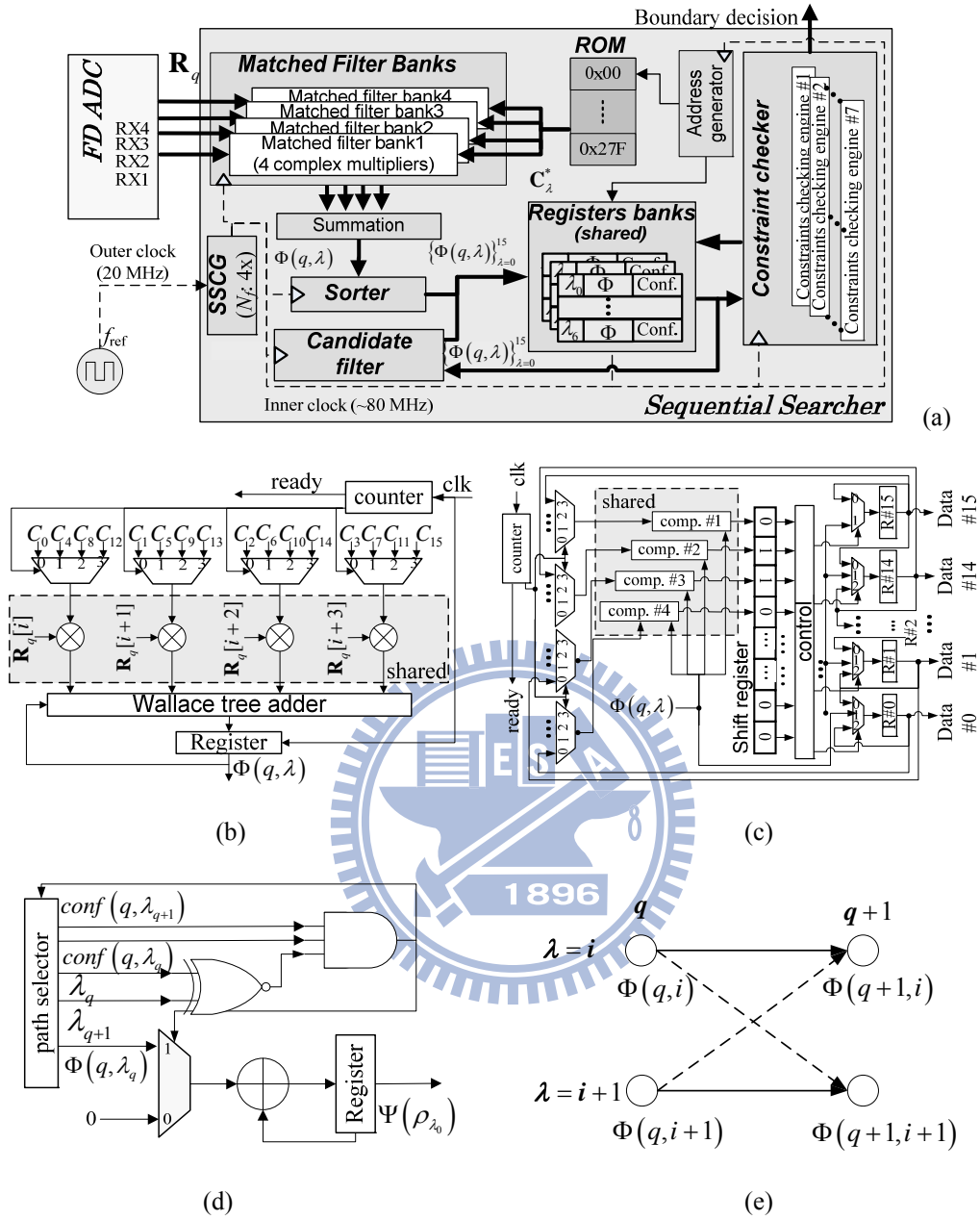
Figure 2-10: VLSI architecture and structure of the proposed sequential searcher for FD symbol synchronization in FD MIMO-OFDM modem. (a) shared architecture; (b) matched filter bank with 4 complex multipliers, where C_i is $\mathbf{C}_\lambda[n]$ for convenient expression; (c) sorter; (d) constraint-check engine; and (e) a subset of trellis.

period of N_f-time high-speed clock, and is a factor to tolerate the mismatches of circuits and layouts (α =0.5~2 in an in-house 65-nm CMOS digital process). Then the SSC encoder maps such period into a SSC control word. When the SSCG begins to generate an N_f-time high-speed clock, the counter maintains the "window" signals [57] (Fig. 2-11) to enable the SSC to generate N_f clocks at each rising edge of input clock and to disable the SSC after N_f clocks. This SSC is implemented via cell-based digital-controlled clocker, which utilizes an OR-gate delay chain with AND-gate controlled feedbacks (total 128 stages). Compared with tri-state feedback [58] and pass-transistor feedback, this structure does not need to bother about large parallel loading and long reset latency. With such delay chain, the SSC is able to output a high-speed clock at the positive edge of the "window" signal immediately. In order to reduce timing mismatches, this delay chain is applied in TDC designs too. However, the length of TDC delay chain is only 64, which is shorter than the length of SSC. One "D-type latch" must be used at the output stage of the proposed delay chain to reduce probabilities of timing violations of the TDC cascaded counter. This counter extends the measurement range of input clocks in the way similar to measure the distance of a ball rolling on the ground. The period of input clock is calculated via TDC. The delay chain inside TDC starts to run at the positive edge of the 1/2 input clock and the D-type flip-flops record the delays to digitize the input period at the

falling edge of the 1/2 input clock. By using the proposed all-digital SSCG, an approximate high-speed clock can be easily created and synchronized at each rising edge of input clock without PLLs. Yet, the main cost applying this SSCG is about 10% ~ 15% additional timing margin in VLSI implementations.

(a)
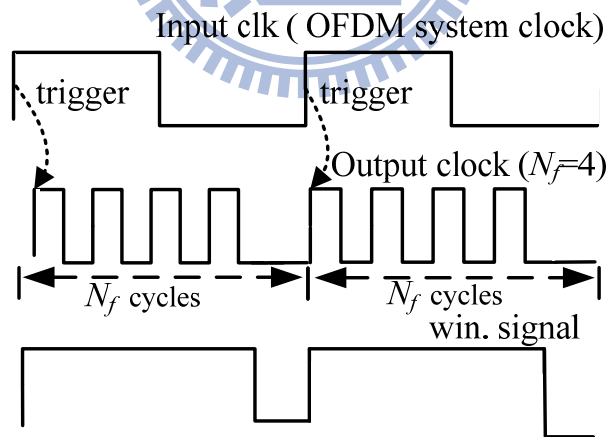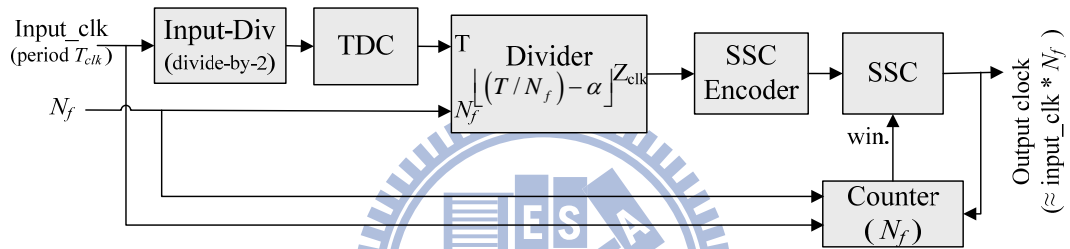
(b)
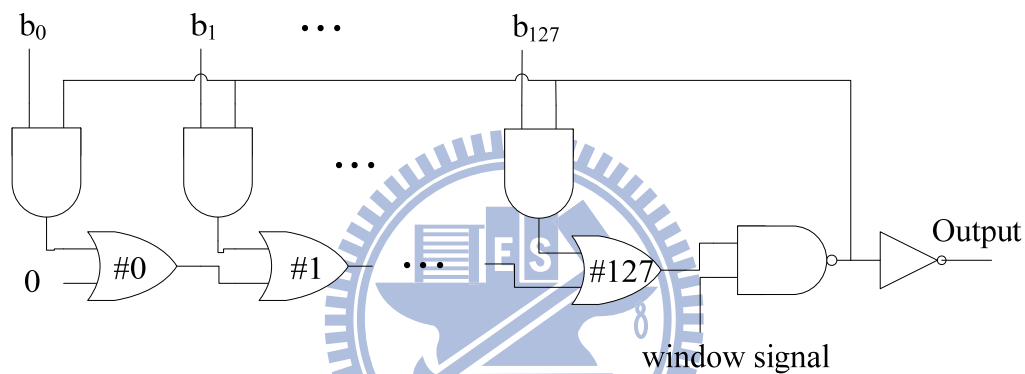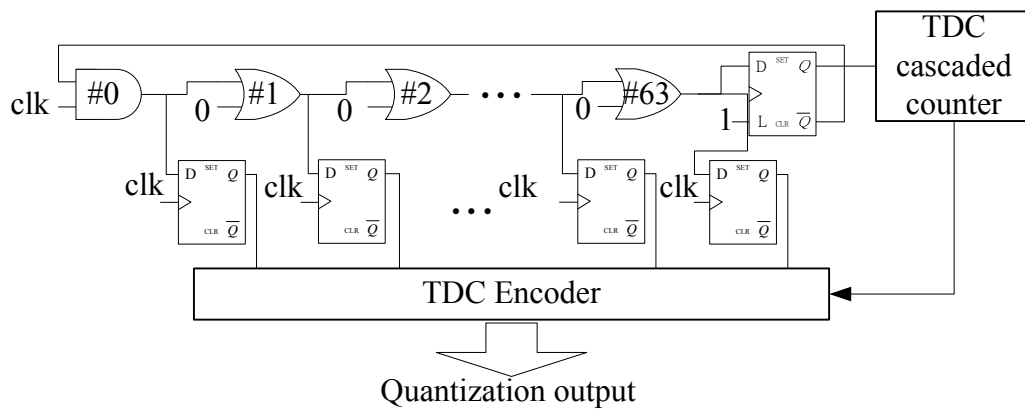
Figure 2-11: (a) Structures, and (b) behavior of the proposed semi-synchronous clock generator (SSCG) with TDC and SSC circuits. (c) TDC circuit with 64 stages (clk is the clock that divides input clock by 2). (d). SSC circuit with 127 stages.

2.5.3 Implementations Results

A platform of software-defined radio was constructed for rapid verification of the proposed proposal. To transmit and record real wireless, XilinxDSP Development Kits with on-board 14-bit analog-to-digital converters (A/Ds), 14-bit digital-to-analog converters (D/As) and (2-Million gates) field programmable gate array (FPGA) are

connected to an in-house 2.4 GHz RF module with 20 MHz bandwidth. At the transmitter part, the transmitted data is produced by the MATLAB module and stored in memory. The signals are then transmitted using the in-house RF front-end. The proposed method is mapped onto FPGA (Xilinx Virtex-II) on the receiver side for wireless measurements. Due to the toolchain limitations, the proposed SSCG does not port to FPGA. The emulation of FD ADC is realized by conventional ADC and FFT. The output of conventional ADC directly transforms to frequency domain via FFT. As shown in Fig. 2-1(b), the proposed symbol synchronizer uses gated clock to control the operation timing of FFT. Finally, the hardware-description language (HDL) of the proposed symbol synchronizer can be realized as soon as the architecture with a fixed-point evaluation has been created.

The proposed design is then implemented by Taiwan Semiconductor Manufacturing Company (TSMC) 65-nm one-poly six-metal layer (1P6M) CMOS technology. The total gate count is 84.881K to occupy 76.336 um^2 and to consume 5.2mW at 1.0-V supply voltage and 80-MHz clock rate. The matched filter banks occupy 70.35% of total gate count and the three modules of sorter, constraints checker and candidate filter only need 14.89%. A 640-byte ROM, applied in LUT, requires 2.4% of total gate count. In addition, the proposed SSCG requires 3.03K gates only. Figure 2-12 displays the post-layout simulation of SSCG with 20 MHz input clock

and N_f=4. According to Equation (2.41) with $\alpha = 1$, the approximate high-speed clock is 82.1 MHz and the frequency offset is 2.63% (referred to 80 MHz), being much less than 15% timing margin. The output range of SSCG can be 43 MHz ~ 680 MHz. Table 2-2 summarizes the implementations of the proposed sequential searcher.

Table 2-2 Summary of the Proposed Implementation

Technology	65-nm 1P6M CMOS
OFDM System Clock	20 MHz
Working Clock	~ 80 MHz (4X)
Max. Operating Clock	106 MHz
SSCG Input Range	600 KHz ~ 40 MHz
SSCG Output Range	43 MHz ~ 680 MHz
# of Gate Count	84.881K
Area	76.336 um^2
Power Consumption	5.2 mW @ 1.0 V
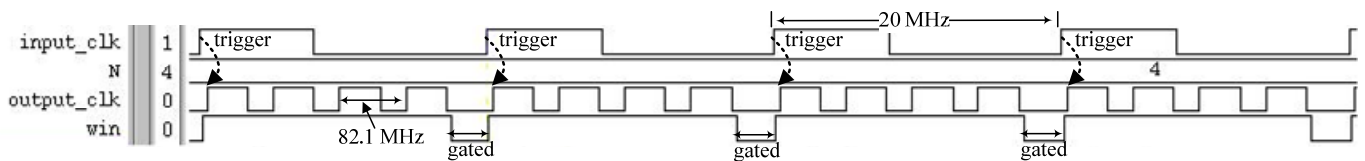
Figure 2-12: Post-layout simulation of the proposed SSCG with 20 MHz input clock and 82.1 MHz output clock (being 2.63% offset) for N_f =4 and α=1.

Finally, the proposed approach is compared to three symbol synchronizers [59]-[61] which are based on TD-ADC architecture. In order to eliminate the factors of implementation technology (i.e. silicon technology) and system parameters (i.e. number of stream, preamble length, and quantization bits), the comparisons are based on the normalized complexity. With the 65-nm technology, the normalized area is defined as [62]

$$\text{Normalized Area} = \text{Area} / (\text{Technology} / 65\text{nm})^2 / N_{stream} / L \qquad (2.42)$$

where N_{stream} is the number of stream and L is the preamble length in the implementation system. The area for symbol synchronization in research [60] is 1.43=(0.49*2+0.12+0.23+0.1) mm^2. Thus, the normalized area is 1510.4≈(1430000/ (250/65)^2)/1/64) um^2. The cells and gate count usually are similar in different technology. Therefore, the normalized cells is calculated as

$$\text{Normalized Cells} = \text{Cells} / N_{stream} / L \qquad (2.43)$$

, and the normalized gate count is

$$\text{Normalized Gate Count} = \text{Gate Count} / N_{stream} / L \qquad (2.44)$$

The cells for symbol synchronization in research [59] is 27847=(3688+5766+18393). According to the Equation (2.42), the normalized cells of research [59] are 435.11≈ (27847/64/1). Since the synchronizer in [61] provides the information of number of quantization bits, the normalized gate count can be redefined as

$$\text{Normalized Gate Count} = \text{Gate Count} / N_{stream} / L / Q \qquad (2.45)$$

Where Q is the number of quantization bits of the input data. The gate count for symbol synchronization in research [61] is 44.4k=(62.4K-4K-14K). Therefore, the normalized gate of research [61] is 216.59≈(44400/41/1/5) since only 41 samples of partial preamble are used to decrease the implementation complexity. For our approach (synchronizer for 4x4 MIMO-OFDM), the area, cells, and gat count are 76336 um2, 26.813K, and 84.881K, respectively. Then, the normalized area is 1192.8=(76336/4/16) um^2, the normalized cells is 418.95≈(26813/4/16), and the normalized gate count is 132.63≈ (84881/4/16/10). We summarize the comparison of implementation complexity in Table 2-3. Our work is the lowest hardware cost in terms of (normalized) area, cell and gate count from Table 2-3. The reason might be the hardware elements are more efficiently reused in our implementation with symbol-rate processes. In spite of the low implementation complexity, the cost of one additional preamble is required for our method. However, it can be avoided because our method is significantly tolerant of CFO, which makes initial synchronization easier and more flexible.

Table 2-3 Comparisons of Symbol Synchronizers

	ADC type	Method	System Specs. (IEEE 802)	Preamble length / utilized length (N)	Performance (Successful detection Prob. at SNR= 0dB)	Implementation Complexity		
						Tech (nm)	Freq. (MHz)	Original/Normalized
[59]	TD	Auto+ matched filter	11a	(L) 64/64	93%	250	20	cell:62.686K /435.11
[60]	TD	Auto+ matched filter	16d	(S) 64/64	-	250	20	area:3370K /1510.9
[61]	TD	matched filter	15.3a	165/41	93.5%	180	132	gate:62.4K /216.59
This work	FD	matched filter + Sequential Search (K=3)	11a/n /ac	(S) 16/16	96.5%	65	80	cell:26.813K /418.95 area:76.336K /1192.8 gate:84.881K /132.63
Note 1. normalized area (um^2) = area/(tech/65)^2/N/stream#, normalized cell = cells /N/stream#, normalized gate = gates/N/stream#/Q-bits								
Note 2. Q-bits are equal to 5 and 10 in the research [57] and our work, respectively.								

2.6 Summary

This chapter builds a low-complexity symbol-rate sequential searcher for OFDM symbol synchronization which is based on FD-ADC techniques. Searching with simple matched filter detection over multiple preambles, the proposed method is significantly tolerant to CFO and works properly at low SNR to make initial

synchronization easier and more flexible. By using symbol-rate processes, the

hardware sharing successfully accomplishes low-complexity implementations. The

main cost of the proposed searcher is to require one additional preamble. Hence, this

work is attractive to very high throughput (VHT) wireless LAN and Multi-Gbps

WPAN specifications using FD-ADC techniques.
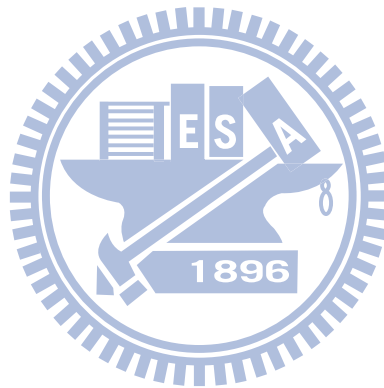
Chapter 3

FD Channel Estimation and

Equalization with Single-FFT

Architecture for SCBT System

Without a CP, most SC transmissions can not adopt frequency-domain equalizer (FDE) directly. This chapter utilizes frequency-domain channel estimator (FD-CE) and decision-feedback aliasing canceller (DF-AC) to produce single-FFT SC-FDE. In this way, SCBT can be decoded using sphere decoder of MIMO-OFDM modems to support multi-mode and backward compatibility under an acceptable complexity in IEEE 802.11 VHT. An N-point FFT is sufficient to measure channel frequency responses (CFR) from L-sample preambles ($L \leqq N/2$). And then, M-bit block codes ($M \leqq L$) are decodable over frequency domains with DF-AC's help. Simulations and

measurements imply that this work can ensure adequate performance, even if there is no CP existed against the distortions of multipath propagation.

In most of the wireless broadband applications like WiMax, Wifi, UWB and WRAN, compensation for multi-path fading is highly pointed in order to make systems work properly. With the help of a CP SISO OFDM and MIMO OFDM systems can be easily integrated. In addition, this can help estimate channels and equalize packets over frequency domains directly. Although SCBT without any CP gains throughput, it causes FFT aliasing in FDE—FDE can not assure sufficient performance directly. Thus, one of the major challenge for multi-mode integrations is to make equalizers as compact as possible, i.e., consolidation of non-CP SCBT, SISO OFDM and MIMO OFDM. Reconfigurable and scalable architectures [63-[64] with heterogeneous units are good solutions to support such operations. However, multiple equalizers are built in designs. A single-carrier frequency-domain equalizer (SC-FDE), being an attractive solution, is developed to eliminate FFT aliasing without a circular property in some approaches [34-[35], e.g., overlap-and-save and overlap-and-add methods. Yet, additional DFT units were included. The user defined formats [65-[67], inserting CP into single-carrier datum against the multipath propagation, were created to improve performance. SC-FDEs with a pair of FFT and IFFT for IEEE 802.16 [64] and IEEE 802.15.3a with an impulse option [69] were developed to demodulate

SCBT with CP over time domains. In the case of single-carrier transmissions with

pseudo noise (PN) spreading, a block-based SC-FDE with both DFT and IDFT for

HIPERLAN-2 [70] was utilized to yield an additional 3-dB gain, and it was also

demodulated in the time domain.

The objective of this chapter is to derive single-FFT processes for supporting

multi-mode and backward compatibility under an acceptable complexity in

MIMO-OFDM modems, such as IEEE 802.11 VHT, with a non-CP SCBT. Figure 3-1

displays the block diagram of the proposed SC-FDE, where the sphere decoder (SD)

[71]-[73] is widely adopted in MIMO-OFDM modems. All equalizations and

decoding are performed over the frequency domain. An N-point FFT is sufficient to

process L-sample preambles and M-bit block codes ($M \leq L \leq N/2$).

The remainder of this chapter is organized as follows. The system assumptions

with problem statements are addressed in Section 3.2. The proposed single-FFT

processes are described in Section 3.3. Performance evaluations are presented in

Section 3.4. Implementations and complexity are discussed in Section 3.5. Finally,

Section 3.6 presents our conclusions.
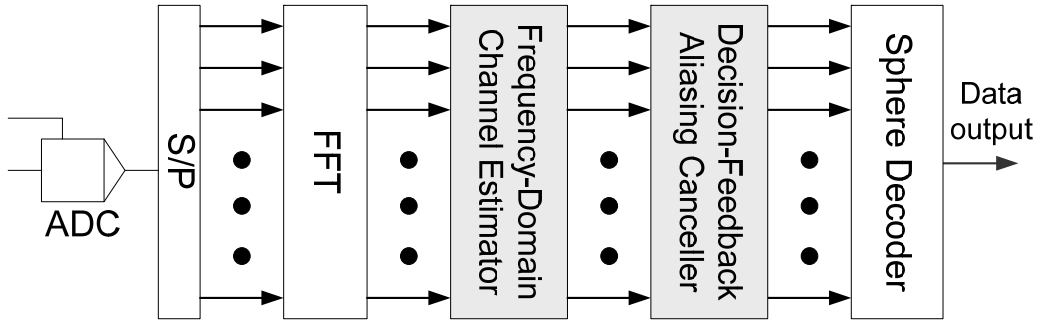
Figure 3-1: The block diagram of FD-ADC based OFDM receivers

3.1 System Assumptions

3.1.1 System Descriptions

Indoor frequency-selective fading, e.g., IEEE [55] and JTC [74], is assumed to roughly span two symbols of L-sample preambles and M-bit block codes. The proposed packet format of non-CP SCBT is that datum without FEC are encoded by block code (K_b code sets contain M bits), modulated by QPSK and synchronized via L-sample preambles ($L \geq M$). The jth received signal can be expressed as

$$\mathbf{r}_j = \mathbf{H}_L \mathbf{s}_j + \mathbf{H}_U \mathbf{s}_{j-1} + \mathbf{n}_0 \tag{3.1}$$

where $\mathbf{r}_j$ is the jth $2L \times 1$ received vector, $\mathbf{n}_0$ is $2L \times 1$ complex additive white Gaussian noise (AWGN) vector with variance σ_n^2, and $\mathbf{s}_j$ is the jth $L \times 1$

68

transmitted symbol, e.g., preambles, SC block codes, or multi-carrier datum with *N-L*

zeros. $\mathbf{H}_{2L \times 2L}$ is the circulant Toeplitz matrix with the first column being $\mathbf{h}$ and

$\mathbf{h} = [h_0, h_1, \cdots, h_{2L-1}]$ denotes a channel impulse response (CIR). Both $\mathbf{H}_L$ and $\mathbf{H}_U$

are the lower triangle (including diagonal entries) matrix and upper triangle matrix of

$\mathbf{H}_{2L \times 2L}$, respectively.

$$\mathbf{H}_{2L \times 2L} = \begin{bmatrix} h_0 & h_{2L-1} & \cdots & \cdots & h_1 \\ h_1 & h_0 & \ddots & \ddots & \vdots \\ \vdots & h_1 & \ddots & h_{2L-1} & h_{2L-2} \\ \vdots & \vdots & \ddots & h_0 & h_{2L-1} \\ h_{2L-1} & h_{2L-2} & \cdots & h_1 & h_0 \end{bmatrix} \quad (3.2)$$

3.1.2 Problem Statements

Linear convolution of two finite sequences is commonly conducted by multiplying the

fast Fourier transforms of these two zero-padding input sequences. In SISO-OFDM

and MIMO-OFDM systems, the CFR can be obtained from the FFT of the received

symbol with CP divided by the FFT of the transmitted sequences [75].

$$R_k = H_k \cdot X_k + n_k \Rightarrow \hat{H}_k \approx \frac{R_k}{X_k}, \ k \in \{0, 1, \cdots, N-1\} \quad (3.3)$$

where *N* is the FFT size, X_k is the kth element of the frequency response of

transmitted sequence, H_k is the kth element of real CFR, and $\hat{H}_k$ is the kth element

of estimated CFR. In frequency-selective fading, the CFR is not an identity matrix.

One problem associated with single-FFT processes for non-CP SCBT is to extend the FFT size in order to be enough to cover the entire packet. For a finite FFT size, it is impossible to gain a linear convolution of non-CP symbols and channel directly. Another consideration is that most zero-forcing equalizers are adversely affected by noise enhancement due to CFR with zeros or very small values (deep fading) [74].

3.2 The Proposed Single-FFT Processes

3.2.1 Frequency-Domain Channel Estimator

Based on the received vector in Equation (3.1), the linear convolution of the jth symbol and the CIR can be deconstructed into two parts: one is *body*, denoted by $\mathbf{H}_L \mathbf{s}_j$, and the other is $\mathbf{H}_U \mathbf{s}_j$, caused by *interblock interference* (IBI). In receivers, the body part of the current symbol convolved with the CIR is mixed with the IBI term of previous symbols in each FFT window. These two components can be separated for linear convolution over the time domain, namely *preamble reconstruction*. Taking all possibilities of QPSK modulations, the preambles (training symbols) are multiplied by complex coefficient. If "1" is the basis, the other three cases, i, -1, and $-i$ can be written as $c_2 \cdot 1$, $c_3 \cdot 1$, and $c_4 \cdot 1$, where c_2 is i, c_3

is -1, and c_4 is $-i$. Two useful combinations of convolved vectors are

$$\begin{cases} \mathbf{y}' = c_1 \cdot \mathbf{H}_L \mathbf{b} + c_2 \cdot \mathbf{H}_U \mathbf{b} \\ \mathbf{y}'' = c_3 \cdot \mathbf{H}_L \mathbf{b} + c_4 \cdot \mathbf{H}_U \mathbf{b} \end{cases}, \quad c_1 \neq c_3 \text{ or } c_2 \neq c_4 \qquad (3.4)$$

where $\mathbf{b}$ is the $L \times 1$ base vector of modulated preambles. Via Equation (3.1), the

received signals can be rewritten as

$$\begin{cases} \mathbf{r}' = \mathbf{y}' + \mathbf{n}' = c_1 \cdot \mathbf{H}_L \mathbf{b} + c_2 \cdot \mathbf{H}_U \mathbf{b} + \mathbf{n}' \\ \mathbf{r}'' = \mathbf{y}'' + \mathbf{n}'' = c_3 \cdot \mathbf{H}_L \mathbf{b} + c_4 \cdot \mathbf{H}_U \mathbf{b} + \mathbf{n}'' \end{cases} \qquad (3.5)$$

and the body part and the IBI term can be found by

$$\begin{cases} \mathbf{H}_L \mathbf{b} = \dfrac{c_4 \cdot \mathbf{r}' - c_2 \cdot \mathbf{r}''}{c_1 c_4 - c_2 c_3} + \dfrac{-c_4 \cdot \mathbf{n}' + c_2 \cdot \mathbf{n}''}{c_1 c_4 - c_2 c_3} \\ \mathbf{H}_U \mathbf{b} = \dfrac{c_1 \cdot \mathbf{r}'' - c_3 \cdot \mathbf{r}'}{c_1 c_4 - c_2 c_3} + \dfrac{-c_4 \cdot \mathbf{n}' + c_2 \cdot \mathbf{n}''}{c_1 c_4 - c_2 c_3} \end{cases} \qquad (3.6)$$

In Equation (3.6), each second term is also AWGN. To reduce AWGN effects, $\mathbf{H}_L \mathbf{b}$

and $\mathbf{H}_U \mathbf{b}$ can be obtained as

$$\begin{cases} \mathbf{H}_L \mathbf{b} = \dfrac{c_4 \cdot E[\mathbf{r}'] - c_2 \cdot E[\mathbf{r}'']}{c_1 c_4 - c_2 c_3} = \dfrac{c_4 \cdot \mathbf{y}' - c_2 \cdot \mathbf{y}''}{c_1 c_4 - c_2 c_3} \\ \mathbf{H}_U \mathbf{b} = \dfrac{c_1 \cdot E[\mathbf{r}''] - c_3 \cdot E[\mathbf{r}']}{c_1 c_4 - c_2 c_3} = \dfrac{c_1 \cdot \mathbf{y}'' - c_3 \cdot \mathbf{y}'}{c_1 c_4 - c_2 c_3} \end{cases} \qquad (3.7)$$

where $E[\mathbf{r}']$ and $E[\mathbf{r}'']$ can be individually calculated through averaging the two

sets of the received preambles that collect two specific combinations of current and

previous symbols defined in Equation (3.5). After averaging $\mathbf{r}'$ and $\mathbf{r}''$ and solving

$\mathbf{H}_L \mathbf{b}$ and $\mathbf{H}_U \mathbf{b}$, the CFR can be measured via one-tap division. The frequency

response is

$$\hat{\mathbf{H}}_N[k] = \frac{\mathbf{Y}_N[k]}{\mathbf{B}_N[k]} \tag{3.8}$$

where $\mathbf{Y}_N = \mathbf{F}_N([(\mathbf{H}_L\mathbf{b})^T \quad (\mathbf{H}_U\mathbf{b})^T]^T)_{ze}$, $\mathbf{B}_N = F_N(b)_{ze}$, $\mathbf{F}_N$ is an $N \times N$ Fast Fourier matrix with entries given by $\mathbf{F}_{p,q} = e^{2\pi pqi/N}$, $(\bullet)_{ze}$ represents zero padding for the length of N and $N \geq 2L$. Furthermore, $c_4 \cdot \mathbf{y}' - c_2 \cdot \mathbf{y}''$ and $c_1 \cdot \mathbf{y}'' - c_3 \cdot \mathbf{y}'$ are the functions of preamble reconstruction.

3.2.2 Decision-Feedback Aliasing Canceller

Based on decision feedback, the jth received datum (in frequency domains) can be rewritten as

$$\mathbf{R}'_j = \mathbf{R}_j - \mathbf{F}_N(\mathbf{H}_U\hat{\mathbf{s}}_{j-1})_{ze} = \mathbf{F}_N(\mathbf{H}_L\mathbf{s}_j)_{ze} + \mathbf{F}_N(\mathbf{n}_0)_{ze} \tag{3.9}$$

where $\mathbf{R}_j \triangleq \mathbf{F}_N(\mathbf{r}_j)_{ze}$ and $\hat{\mathbf{s}}_{j-1}$ is the previous decoded symbol. Similar to MIMO detections, if a maximum-likelihood (ML) decision [76] is applied to decode datum over the frequency domain, the maximum a priori equals

$$\hat{\mathbf{s}}_j = \arg \min_{\mathbf{d}_j \in \mathbb{C}} \left| \mathbf{R}'_j - \mathbf{F}_N(\mathbf{H}_L\mathbf{d}_j)_{ze} \right|^2 \tag{3.10}$$

where $\mathbb{C}$ indicates the code set and $\mathbf{d}_j$ is an *M*-bit block code. Reducing the complexity of implementations and sharing with a MIMO-OFDM modem, an ML decision is replaced by SD. Although CFR $\hat{\mathbf{H}}_N$ is estimated using linear convolution with a preamble reconstruction, the body part and the aliasing term of each ideal code

set must be separated for decoding references. Instead of re-transforming to time

domains for $\mathbf{H}_L \mathbf{d}_j$ and $\mathbf{H}_U \hat{\mathbf{s}}_{j-1}$, a separation operator $\tilde{\mathbf{G}}$ is constructed to extract

$\mathbf{F}_N \left(\mathbf{H}_L \mathbf{d}_j \right)_{ze}$ via the linear convolution of $\mathbf{d}_j$ and $\mathbf{h}$.

$$\begin{aligned} \mathbf{F}_N \left(\mathbf{H}_L \mathbf{d}_j \right)_{ze} &= \tilde{\mathbf{G}} \mathbf{F}_N \left(\mathbf{h} \otimes \mathbf{d}_j \right)_{ze} \\ &= \tilde{\mathbf{G}} \mathbf{D}_H \mathbf{F}_N \left(\mathbf{d}_j \right)_{ze} \end{aligned} \tag{3.11}$$

$$\mathbf{F}_N \left(\mathbf{H}_U \hat{\mathbf{s}}_j \right)_{ze} = \mathbf{D}_H \mathbf{F}_N (\hat{\mathbf{s}}_j)_{ze} - \mathbf{F}_N \left(\mathbf{H}_L \hat{\mathbf{s}}_j \right)_{ze} \tag{3.12}$$

where $\otimes$ is the linear convolution and $\mathbf{D}_H = diag \left(\hat{\mathbf{H}}_N [0], \hat{\mathbf{H}}_N [1], \cdots, \hat{\mathbf{H}}_N [N-1] \right)$

is a diagonal matrix containing the CFR. After the channel estimation, multiply

$\mathbf{F}_N \left(\mathbf{d}_j \right)_{ze}$ by $\mathbf{D}_H$, and pass through the separation operator $\tilde{\mathbf{G}}$ —A new coefficient

$\mathbf{F}_N \left(\mathbf{H}_L \mathbf{d}_j \right)_{ze}$ is produced for sphere decoding. In the time domain, the body part is

easily derived by taking the first L of linear convolution.

$$\mathbf{H}_L \mathbf{d}_j = \mathbf{G} \cdot \left(\mathbf{h} \otimes \mathbf{d}_j \right), \quad \mathbf{G} = \begin{bmatrix} \mathbf{I}_{L \times L} & \mathbf{0}_{L \times (N-L)} \\ \mathbf{0}_{(N-L) \times L} & \mathbf{0}_{(N-L) \times (N-L)} \end{bmatrix} \tag{3.13}$$

Then separation operator $\tilde{\mathbf{G}}$ can be obtained by Equations (3.11) and (3.13).

$$\tilde{\mathbf{G}} = \mathbf{F}_N \mathbf{G} \mathbf{F}_N^{-1} \tag{3.14}$$

Each entry value of $\tilde{\mathbf{G}}$ is constant because the matrices of $\mathbf{F}_N$, $\mathbf{G}$ and $\mathbf{F}_N^{-1}$ are

fixed. After cancellation of the aliasing term $\mathbf{F}_N (\mathbf{H}_U \hat{\mathbf{s}}_{j-1})_{se}$ of the previous decoded

symbol $\hat{\mathbf{s}}_{j-1}$, $\mathbf{s}_j$ is decodable over frequency domains. In the case of decoding the 1st

data symbol, $\mathbf{F}_N (\mathbf{H}_U \hat{\mathbf{s}}_{j-1})_{se}$ is acquired prior from the packet header.
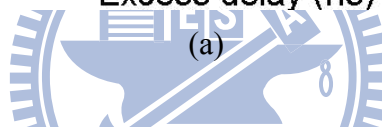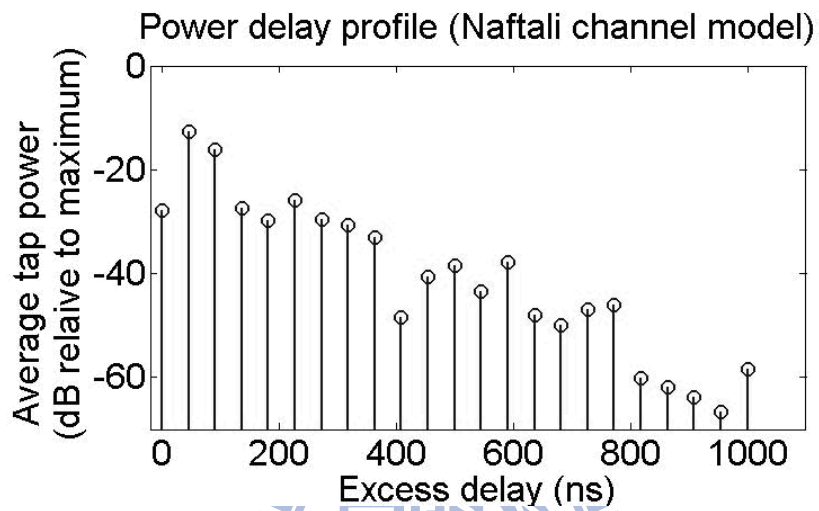
3.3 Performance Evaluations

The WiFi systems and a linear block codes are used to evaluate the proposed SC-FDE (without FEC), where the FFT size is 64 and the number of preambles is 56. Each preamble, modulated by BPSK, is spreading with 11-chip Barker code (L=11) [2]—two useful combinations of preambles are $\{c_1=1, \ c_2=1\}$ and $\{c_3=1, \ c_4=-1\}$. Only one antenna is utilized to receive the non-CP SCBT in the MIMO-OFDM modem. The basis of our performance is the packet error rate (PER) that is required to be 8% in frequency-selective fading. Figure 3-2 displays the power delay profiles of JTC and IEEE 802.11 (Naftali model: Rayleigh fading with phase distributed uniformly) channel models, which are used to measure the system performance in multipath environment. The packet length is 1024 bytes, encoded by linear (8, 4) code [72] with BPSK modulation and complementary code keying (CCK) [2] with QPSK modulation, respectively. The generator matrix of a linear (8, 4) code is given by

$$\mathbf{H}_{(8,4)} = \begin{bmatrix} 1 & 0 & 1 & 0 & 1 & 0 & 1 & 0 \\ 1 & 1 & 0 & 0 & 1 & 1 & 0 & 0 \\ 1 & 0 & 0 & 1 & 1 & 0 & 0 & 1 \\ 1 & 1 & 1 & 1 & 0 & 0 & 0 & 0 \end{bmatrix} \tag{3.15}$$

The minimum hamming distance is 4. In WiFi systems, each CCK codeword (8-bit orthogonal block code) is composed of four phases φ_1, φ_2, φ_3 and φ_4 of

$\{0, \pi/2, \pi, 3\pi/2\}$ (*M*=8).

Power delay profile (Naftali channel model)

(a)

Power delay profile (Naftali channel model)

(b)

Power delay profile (JTC Office B)

(c)
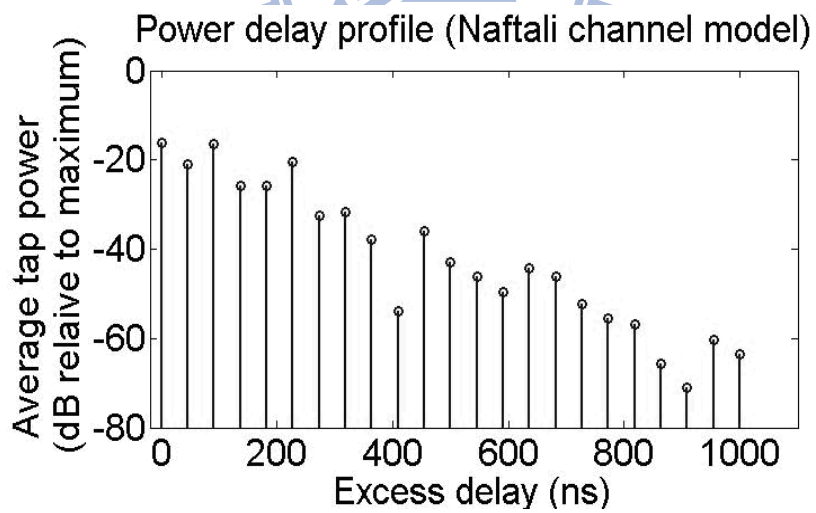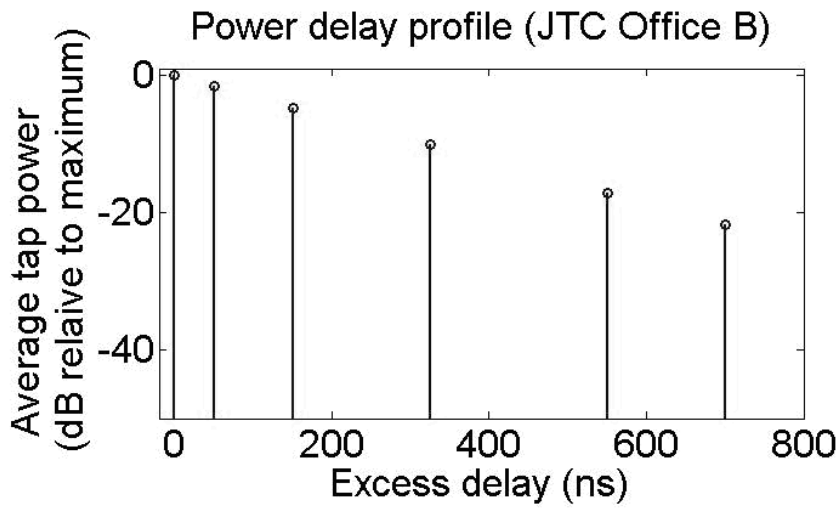
Power delay profile (JTC residential C)
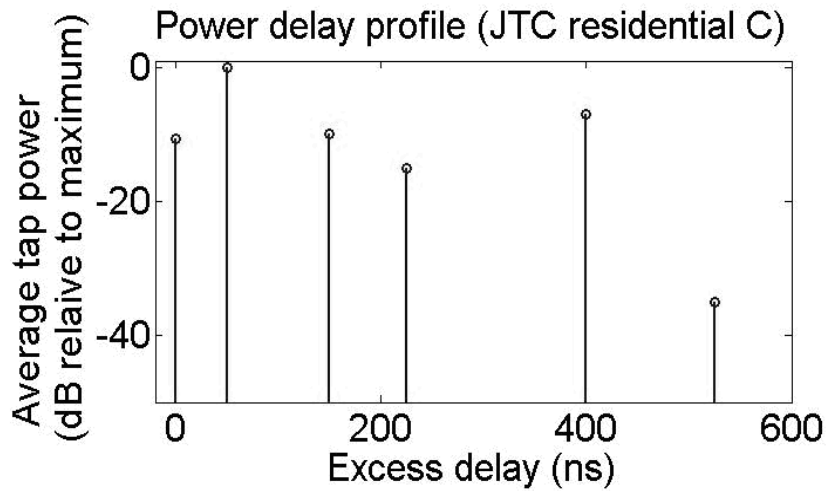
(d)

Figure 3-2: Power delay profiles for IEEE and JTC channel models. (a) and

(b) two random cases of IEEE model (RMS delay spread is 100 ns). (c) JTC

indoor office B model. (d) JTC indoor residential C model

Figure 3-3 plots the PER of the linear (8, 4) code in both JTC and IEEE 802.11

fading channels. Compared with the case of AWGN, our SNR losses are around 3.6

dB ~ 5.6 dB, depending on fading environments. In Fig. 3-4, the proposed scheme has

improved performances compared with some time-domain extents [78]–[79]. The

simulation results of channel model of JTC indoor office A indicates that the proposed

scheme performs better than previous study [78], because the nonlinear equalization

employs the sphere decoding with the search of minimum Euclidean distance over

transmitted symbols. In the case of JTC indoor residential B, a CFO of 50 ppm with

1-ppm and 2-ppm residual errors caused by automatic frequency control (AFC) is

induced in systems. In contrast with the ICI equalizer [79], this proposal also yields an

improvement of 20-dB, indicating that the impact of residual CFOs does not make

significant performance degradation. By transferring RF signals to MATLAB via

USB for real-time measurements before VLSI implementations, XilinxDSP

Development Kits with on-board 14-bit A/Ds, 14-bit D/As and FPGA (2-million gates

and 50 MHz) are connected to an in-house 2.4 GHz 2x2 RF module with 20-MHz

bandwidth to transmit and record real wireless packets. In this way, a

software-defined radio (SDR) platform is shown in Fig. 3-5. The received EVM of

QPSK is about -21 dB.
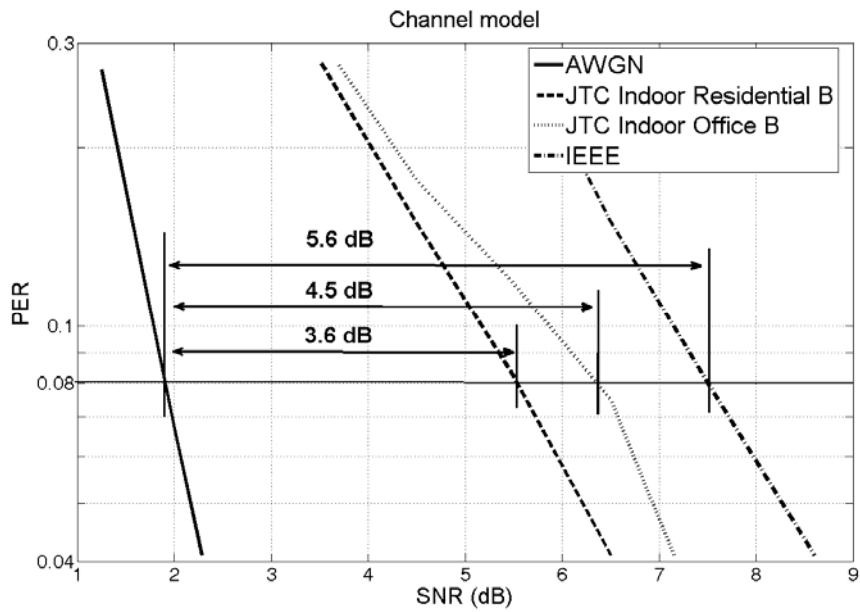
Figure 3-3: Simulation of the linear (8, 4) code in IEEE and JTC fading
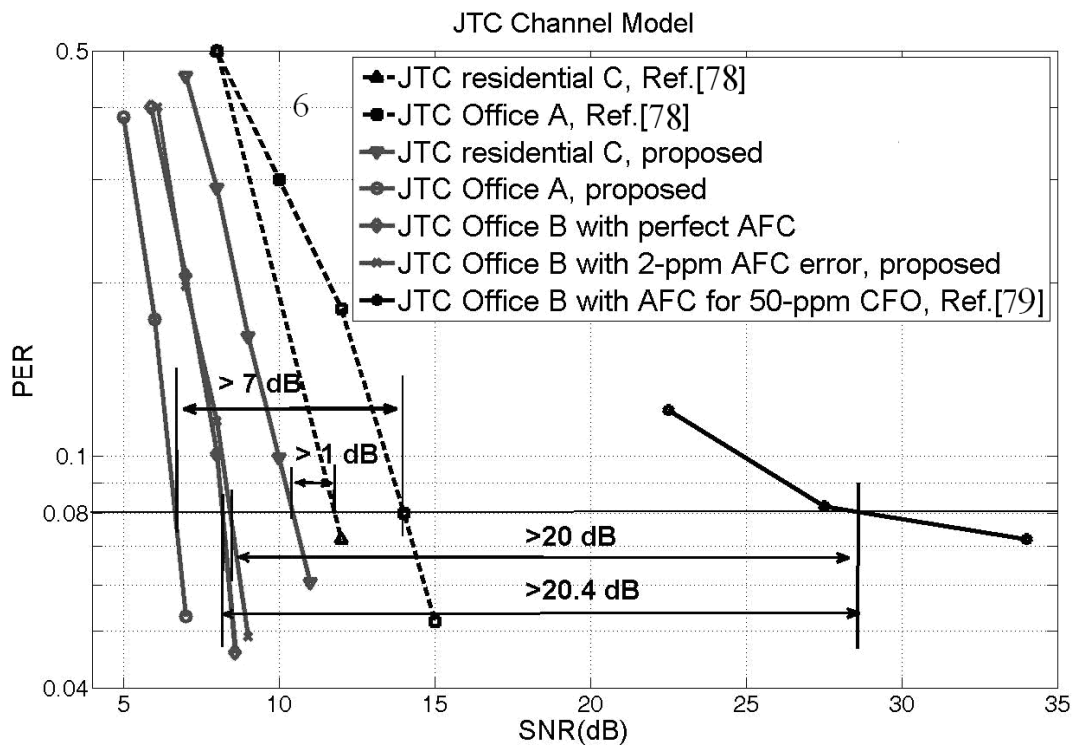
Figure 3-4: Simulation of CCK in JTC fading － office A, residential C

and office B with residual CFOs.
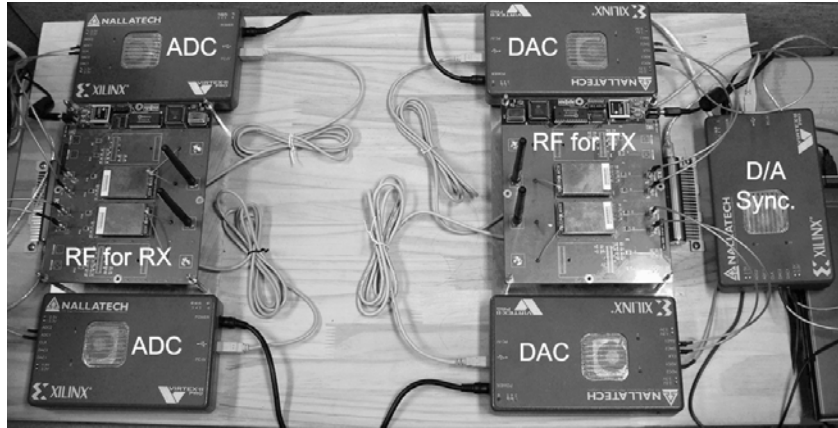
Figure 3-5: SDR platform for SCBT measurements.

3.4 Implementation and Complexity

Figure 3-6 and 3-7 show the block diagrams of the proposed FD-CE and single-FFT

SC-FDE with DF-AC, respectively. Five key modules are derived in the FD-CE: (1) a

preamble reconstruction with pattern recognition for pre-processing linear

convolution before FFT; (2) a look-up table (LUT) for storing the ideal frequency

responses of preamble; (3) complex multipliers with conjugate output for calculating

the linear convolution; and, (4) two averages for reducing AWGN effects. The

single-FFT SC-FDE with DF-AC (Fig. 3-7) contains five major building blocks: (1)

an DF-AC to eliminate the FFT aliasing of non-CP symbols; (2) a sphere decoder to

decode datum over the frequency domain without noise enhanced; (3) an LUT to save

ideal frequency responses of *M*-bit block codes as decoding references; and, (4)

complex multipliers (shared with FD-CE) to generate new references for sphere

decoding.
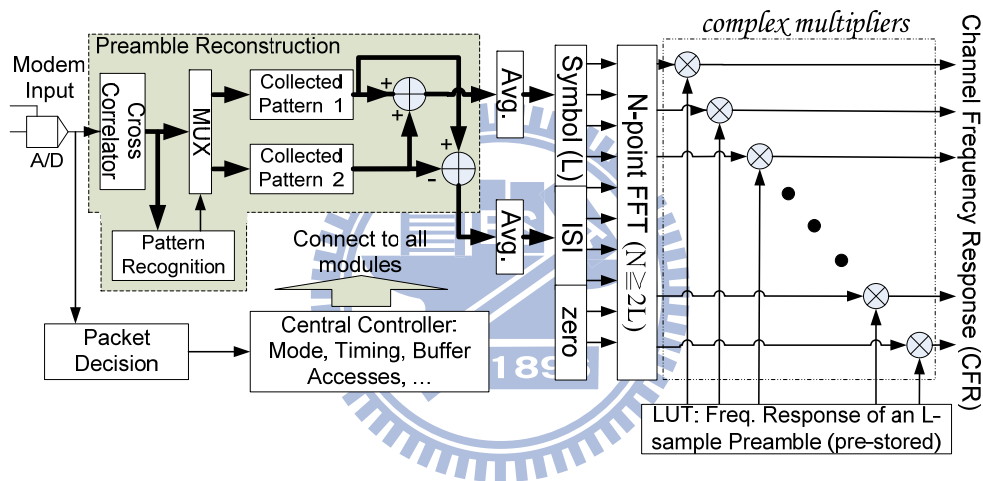
Figure 3-6: Block diagram of the proposed FD-CE.
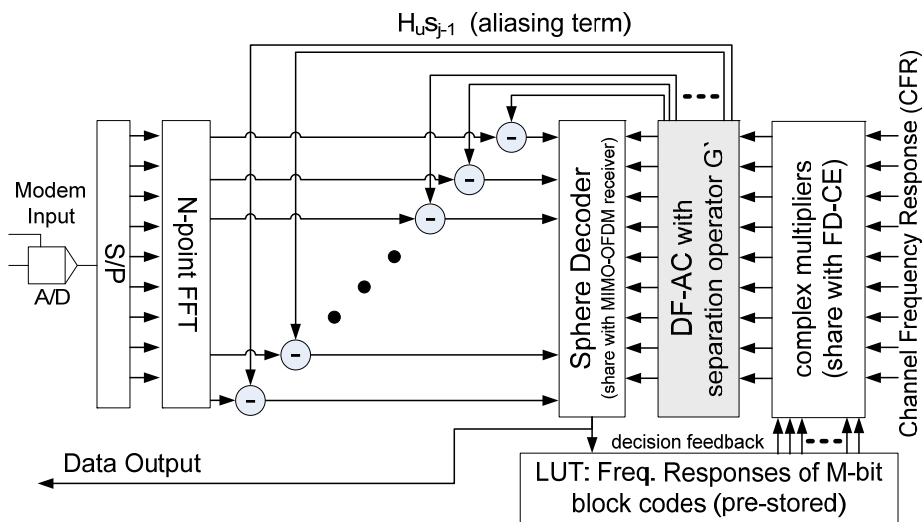
Figure 3-7: Block diagram of the single-FFT SC-FDE with DF-AC

3.4.1 Sphere Decoder with SCBT Decoding

The decoding problems in both modes (SCBT and MIMO OFDM) can be formulated as Maximum-likelihood (ML) search, which can be efficiently solved through SD algorithm. In terms of tree traversal behavior, the classical SD algorithm is a type of depth-first branch and bound (B&B) algorithm that approaches to the solution of ML detection via two stages: preprocessing of QR decomposition, and tree search. In contrast with the classical SD, three parts of our SD are different when SCBT decoding is performed, which are the preprocessing, metric computation and tree structure. The main overhead of such SD is the control unit to deal with all data paths in implementations. The detail procedures of the SD for MIMO detection and SCBT decoding are recalled as follows:

Symbol definitions: $\mathbf{x}$ is the M_T-dimensional transmitted signal vector ($\mathbf{x} \triangleq \begin{bmatrix} x_1 \ x_2 \ \cdots \ x_{M_T} \end{bmatrix}^T$), $\mathbf{y}$ is the M_R-dimensional received signal vector ($\mathbf{y} \triangleq \begin{bmatrix} y_1 \ y_2 \ \cdots \ y_{M_R} \end{bmatrix}^T$), $\mathbf{H}$ is $M_T \times M_R$ channel matrix, and $\mathbf{x}^{(i)} \triangleq \begin{bmatrix} x_i \ x_{i+1} \ \cdots \ x_{M_T} \end{bmatrix}^T$.

a). Depth-first SD with MIMO detection

1) Pre-compute the QR decomposition on $\mathbf{H}$ by QR operations ($\mathbf{H} = \mathbf{QR}$);

2) For each data sub-carrier from each antenna:

   i.   Compute $\mathbf{y}'$ ($\mathbf{y}' = \mathbf{Q}^H \mathbf{y}$) by complex multiplier banks;

   ii. Perform depth-first tree search by SD engines [47] which search the solution of $\hat{\mathbf{x}} = \arg \min_{\mathbf{x} \in \mathbb{Z}_Q^M} |\mathbf{A} - \mathbf{B}|^2$, where $\mathbf{A} = \mathbf{y}'$ and $\mathbf{B} = \mathbf{R}\mathbf{x}$. The initial radius of sphere decoder is infinite and the metric computation at level i is

$$\Phi\left(\mathbf{x}^{(i)}\right) = \left| \mathbf{y}'_i - \sum_{j=i+1}^{M_T} \mathbf{R}_{ij}\mathbf{x}_j - \mathbf{R}_{ii}\mathbf{x}_i \right|^2 \qquad (3.16)$$

b). Depth-first SD with SCBT decoding

1) Pre-compute the body term ($\mathbf{F}_N\left(\mathbf{H}_L\mathbf{d}_j\right)_{ze}$) and aliasing term ($\mathbf{F}_N\left(\mathbf{H}_U\mathbf{d}_j\right)_{ze}$) by complex multiplier banks;

2) Compute $\mathbf{y}'$ ($\mathbf{y}' = \mathbf{F}_N(\mathbf{r}_j)_{ze} - \mathbf{F}_N(\mathbf{H}_U\hat{\mathbf{s}}_{j-1})_{ze}$) by point-to-point subtraction;

3) Perform depth-first tree search by SD engines [47] which search the solution of $\hat{\mathbf{s}}_j = \arg \min_{\mathbf{d}_j \in \mathbb{C}} |\mathbf{A} - \mathbf{B}|^2$, where $\mathbf{A} = \mathbf{y}'$ and $\mathbf{B} = \mathbf{F}_N(\mathbf{H}_L\mathbf{d}_j)_{ze}$ ($\mathbf{B}$ is pre-calculated in the pre-processing step). The initial radius of sphere decoder is infinite and the metric computation at level i is

$$\Phi\left(\mathbf{x}^{(i)}\right) = |\mathbf{y}'_i - \mathbf{B}_i|^2 \qquad (3.17)$$

where $\mathbf{B}_i$ is the ith element in signal vector $\mathbf{B}$.

The preprocessing in SCBT mode is to calculate the body term ($\mathbf{F}_N\left(\mathbf{H}_L\mathbf{d}_j\right)_{ze}$) and aliasing term ($\mathbf{F}_N\left(\mathbf{H}_U\mathbf{d}_j\right)_{ze}$) while the preprocessing in MIMO mode is QR

decomposition. All of them can be performed by the shared multiplier banks. **B** represents the multiplication result of two matrices in step a.2.ii while it is a frequency-domain signal vector in step b.3 and the metric computation of Equation (3.17) only needs complex subtractions. Hence a classical SD ALU [51] for the metric computation in MIMO-OFDM mode enables to apply for SCBT decoding directly. The tree structure, e.g., a parent node branching to child nodes, is also different in the two modes, as plotted in Figs 3-8(a) and 3-8(b). For the typical SD search tree in N_q-QAM MIMO detection, Fig. 3-8 (a) shows the tree structure that each parent node may extend Q possible child nodes. Figure 3-8 (b) displays the tree structure of SCBT decoding where each parent node can only extend one child node except the root node. When a leaf node is reached, the upper bound (radius) is updated. If the partial Euclidean distance of current node is larger than the upper bound, a dead end is declared and the next start node of backward recursion is always one of the child nodes of root. The SD search engine does not require special extensions because the behavior of tree punching of SCBT decoding still follows the depth-first B&B paradigm. Hence, the main overhead of such SD is to design a control unit to deal with all data flows.
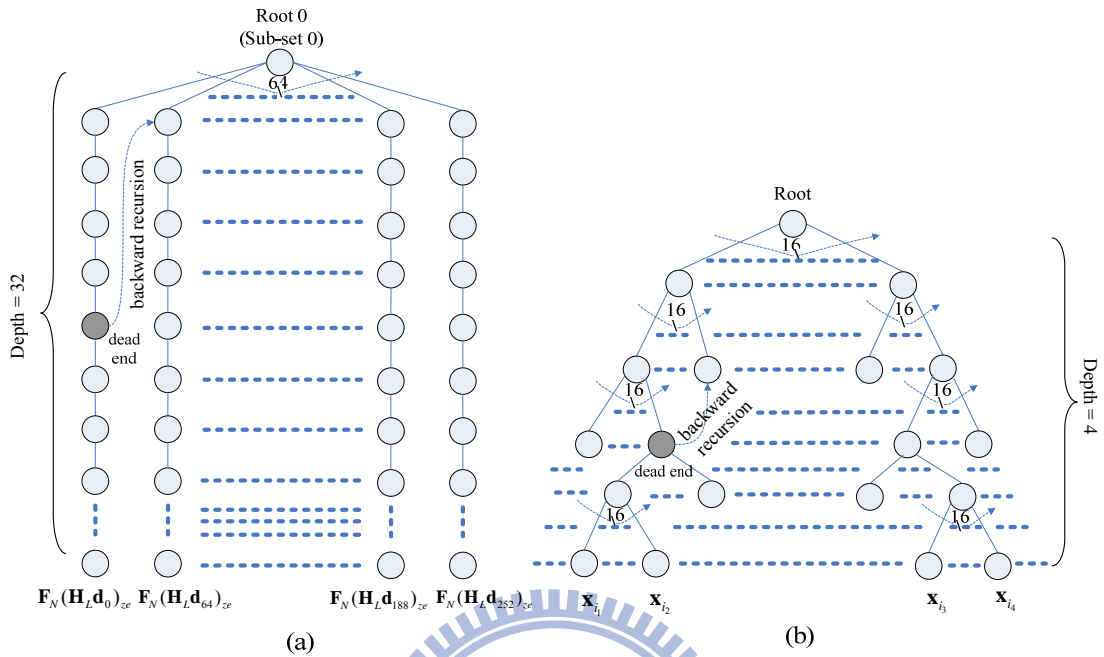
Figure 3-8: Tree structures of SD search in MIMO-OFDM and DSSS-CCK
modes. (a) DSSS-CCK search tree. (b) MIMO-OFDM search tree for 4x4
16-QAM

3.4.2 Detail VLSI Architecture

Figure 3-9 displays the detail architecture of a 4x4 MIMO-OFDM modem with

the proposed SC-FDE supporting two kinds of packet formats in WiFi systems: (1)

DSSS-CCK and (2) MIMO-OFDM. The MIMO-OFDM modem was implemented via

hardware-description language (HDL) and mapped on FPGA of a XilinxDSP

Development Kit. In Fig. 3-9, one of the four FFTs based on variable-length FFT

architecture [80] supports 32 and 64 points, transferring the reconstructed data to the

frequency domain. The preamble reconstruction extracts both body and ISI terms of

Barker code to reconstruct linear convolution before FFT. By multiplying the

frequency response of reconstructed data with the reciprocal of the frequency

response of an ideal preamble (Barker code; pre-stored in ROM1), the channel

frequency response (CFR) is extracted. Once the CFR is obtained, the ALU uses the

four complex multiplier banks to calculate $\mathbf{D}_H \mathbf{F}_N \left(\mathbf{d}_j \right)_{ze}$ and

$\mathbf{F}_N \left(\mathbf{H}_L \mathbf{d}_j \right)_{ze} = \tilde{\mathbf{G}} \mathbf{D}_H \mathbf{F}_N \left(\mathbf{d}_j \right)_{ze}$ for all $\mathbf{d}_j$, where $\mathbf{d}_j$ is the frequency response of an

ideal CCK code and $\tilde{\mathbf{G}}$ is the matrix operator (both saved in the ROM2). For all

CCK codes, each output of $\mathbf{D}_H \mathbf{F}_N \left(\mathbf{d}_j \right)_{ze}$ and the body ($\mathbf{F}_N \left(\mathbf{H}_L \mathbf{d}_j \right)_{ze}$) and aliasing

terms ($\mathbf{F}_N \left(\mathbf{H}_U \mathbf{d}_j \right)_{ze}$) are stored in SRAM1 and SRAM2, respectively. If the received

signals are data symbols, CE flag is set to 0. Then, the received signals subtract from

an aliasing term with the feedback code index in SRAM2 to get the body term of the

received signals. The sphere decoder with four SD engines [51] decodes the body

term of received signals and feeds back the decision for next decoding. In the

MIMO-OFDM mode, two long preambles are received to estimate the matrices of

CFR by the four (parallel) channel estimators and then decomposed via the QR

operations (**H=QR**). CE flag is set to 0 if the received signals are MIMO-OFDM

symbol **Y**. The pre-processing of **Y** ($\mathbf{Q}^H \mathbf{Y}$) is performed using complex multiplier

banks and then is recorded in SRAM1. Finally, the decoding is done via the same SD

engines with $\mathbf{Q}^H\mathbf{Y}$ and $\mathbf{R}$.

The symbol duration of each Barker code and CCK code are 1000 ns and 720 ns,

respectively. In Fig. 3-9, the bottlenecks of our data path are the computations of

$\mathbf{D}_H\mathbf{F}_N\left(\mathbf{d}_j\right)_{ze}$ and $\mathbf{F}_N\left(\mathbf{H}_L\mathbf{d}_j\right)_{ze}$. Basically, we need 32*256 and 32*32*256 complex

multiplications to measure $\mathbf{D}_H\mathbf{F}_N\left(\mathbf{d}_j\right)_{ze}$ and $\mathbf{F}_N\left(\mathbf{H}_L\mathbf{d}_j\right)_{ze}$. To reduce the decoding

complexity, the code set with zero phase ones has been calculated $-$ only 32*64 and

32*32*64 complex multiplications are required. The other three phases of

$\mathbf{D}_H\mathbf{F}_N\left(\mathbf{d}_j\right)_{ze}$ and $\mathbf{F}_N\left(\mathbf{H}_L\mathbf{d}_j\right)_{ze}$ can be found by multiplying zero phase codes with

phases $\pi/2$, π and $3\pi/2$. It is also noted that $\widetilde{\mathbf{G}}$ is the circular matrix formulated

as

$$\tilde{\mathbf{G}} = \begin{bmatrix} \tilde{g}_0 & \tilde{g}_{N-1} & \cdots & \tilde{g}_2 & \tilde{g}_1 \\ \tilde{g}_1 & \tilde{g}_0 & \tilde{g}_{N-1} & & \tilde{g}_2 \\ \vdots & \tilde{g}_1 & \tilde{g}_0 & \ddots & \vdots \\ \tilde{g}_{N-2} & & \ddots & \ddots & \tilde{g}_{N-1} \\ \tilde{g}_{N-1} & \tilde{g}_{N-2} & \cdots & \tilde{g}_1 & \tilde{g}_0 \end{bmatrix}, N = 32 \tag{3.18}$$

where $\tilde{g}_0 = 0.5$, $\tilde{g}_i = 0$ when index i is even, and $\tilde{g}_j = a_j + b_j i$ and $\tilde{g}_{N-j} = a_j - b_j i$

when $1 \le j \le 15$. Each element $\tilde{g}_j$ at row i has a conjugate element $\tilde{g}_{N-j}$ at row

$(N+i)_N$, where $(\bullet)_N$ is denoted as modulo operation. A complex multiplier with

additional conjugate output (Fig. 3-10) is created to handle this work. Taking a matrix

multiplication of $\widetilde{\mathbf{G}}\bullet\mathbf{V}$ ($\mathbf{V}$ is a N-dimensional vector), the element $\tilde{g}_j$ at row i and

the element $\tilde{g}_{N-j}$ at row $(N+i)_N$ multiply the same element in $\mathbf{V}$ and the computation rule is depicted by Fig. 3-11. As a result, the computing complexity of $\mathbf{F}_N \left(\mathbf{H}_L \mathbf{d}_j \right)_{ze}$ is reduced to 9*32 complex multiplications and the amount of the required complex multiplications is 9*32*64 for all CCK codes. In our implementation, the matrix multiplications of $\mathbf{D}_H \mathbf{F}_N \left(\mathbf{d}_j \right)_{ze}$ and $\mathbf{F}_N \left(\mathbf{H}_L \mathbf{d}_j \right)_{ze}$ are performed via four complex multiplier banks (8 complex multipliers per bank). If the four complex multiplier banks (parallel) process 32 complex multiplications at 50 MHz, the processing time of ($\mathbf{D}_H \mathbf{F}_N \left(\mathbf{d}_j \right)_{ze}$ and $\mathbf{F}_N \left(\mathbf{H}_L \mathbf{d}_j \right)_{ze}$) is 12.8 us or 640 cycles or 13 Barker codes. Because the AGC and synchronizations consume 16 Barker codes in our designs (AGC: 2 Barker codes, timing recovery: 10 Barker codes and phase recovery: 3~4 Barker codes), the available preambles for preamble reconstruction is 27 (=56-16-13). All storages (Fig. 3-9) represent the elements with word length of 10 bits. ROM1 is 80 bytes to store the reciprocal of the frequency response of an ideal Barker code, and ROM2 is 7680 bytes in which the 5120 and 2560 bytes are used to record the frequency responses of 64 ideal CCK codes with zero phase and the separator operator $\widetilde{\mathbf{G}}$, respectively. ROM3 is 80 bytes to store the reciprocal of long preamble. After calculating $\mathbf{D}_H \mathbf{F}_N \left(\mathbf{d}_j \right)_{ze}$ and body/aliasing terms of all CCK codes, the outputs are saved in SRAM1 (5120 bytes) and SRAM2 (10240 bytes), respectively. Due to the decoding latency of MIMO detection, the clock rate of

SD or K-best SD are up to 200 MHz supporting the 4x4 64-QAM MIMO-OFDM

transmission. For WiFi systems with 4x4 MIMO OFDM and 64 QAM, four SD

engines are required to parallel decode data at 150 MHz － one SD engine with 150

MHz clock rate can meet the decoding latency <720 ns in DSSS-CCK mode (because

the CCK symbol duration is 720 ns). CCK codes can be partitioned into four sub-sets

and decoded using four parallel SD engines, as shown in Fig. 3-12. The parallel

decoding procedure decreases the decoding latency to 40 cycles (or slows down the

clock rate to 100 MHz). Hence, the clock rate and the number of SD engines are

dominated by MIMO detection. The detailed descriptions of SD engines are stated in

the following part.
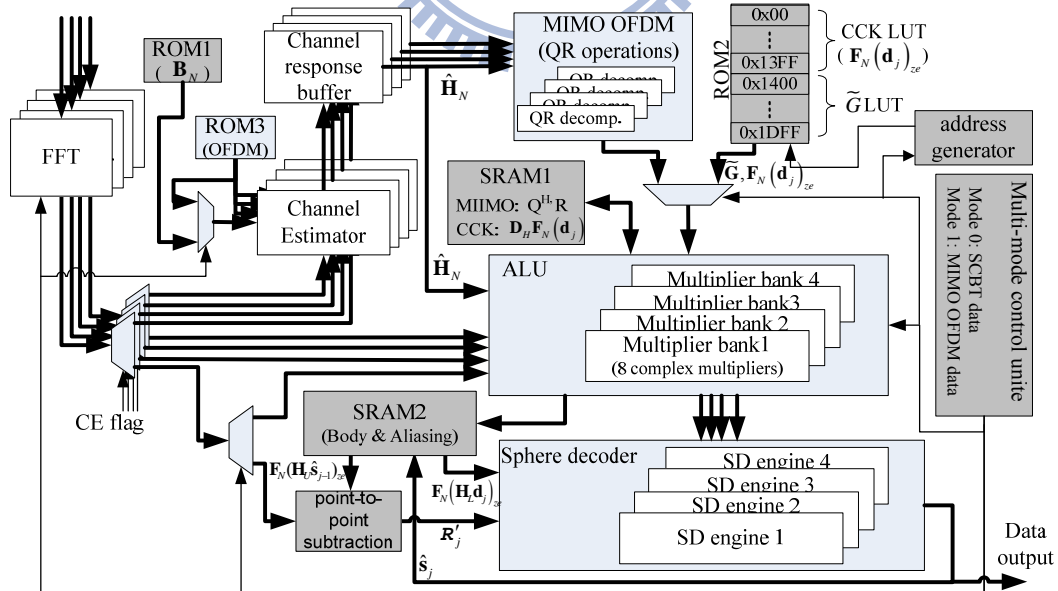
Figure 3-9: Detail architecture and complexity of a 4x4 MIMO-OFDM

modem with the proposed SC-FDE
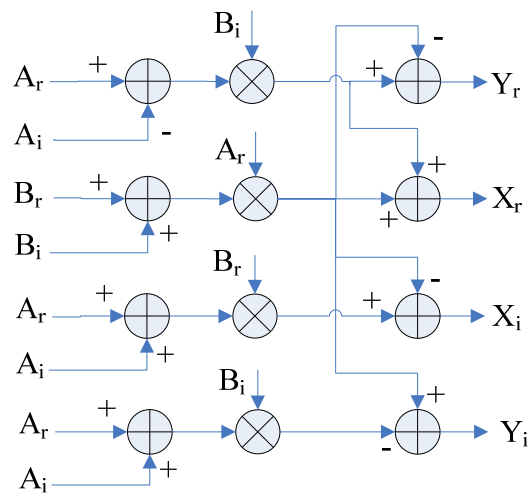
Figure 3-10: Complex multiplier with an additional conjugation output

$$Y = Y_r + Y_i j = (A_r + A_i j) \times (B_r + B_i j) \quad \text{and} \quad X = X_r + X_i j = (A_r + A_i j) \times (B_r + B_i j)^*.$$
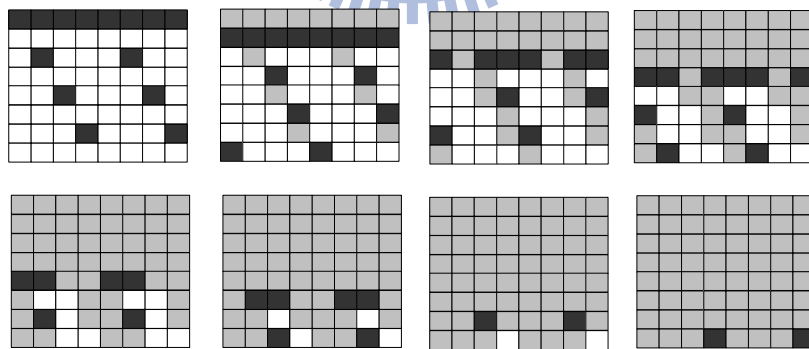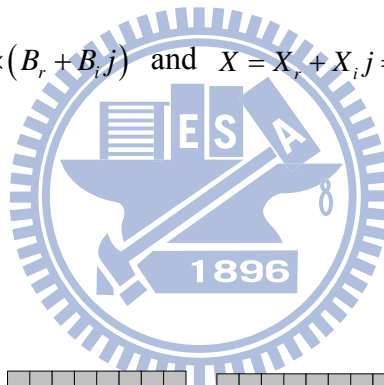
Figure 3-11: The rule of signal multiplications of $\tilde{\mathbf{G}}$; dark squares for the elements being currently computed, and light squares for the elements after calculated).
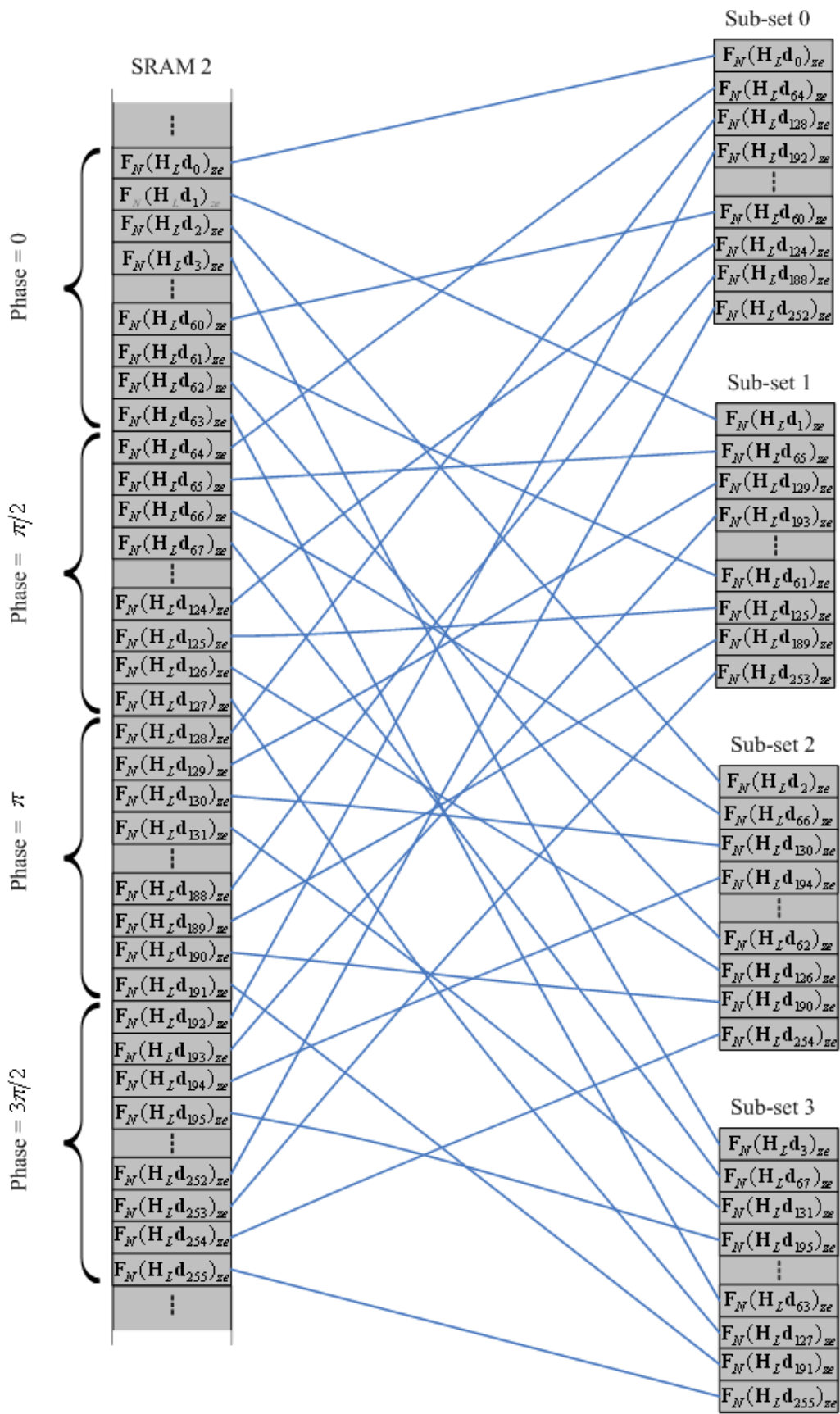
Figure 3-12: CCK mapping on four sub-sets for parallel SD searching

3.4.3 Complexity Summary

The hardware complexity is summarized in Table 3-1. The 0.3% for combination logics, 33.3% for SRAM and 99% ROM are only used in DSSS-CCK mode, which indicates the additional cost making a 4x4 MIMO-OFDM modem support non-CP SCBT is memory (SRAMs and ROMs). Although the total ROM size for the DSSS-CCK mode is 7760 bytes, the major cost of ROMs is just the address decoder. Most combinational logics are shared with MIMO-OFDM and DSSS-CCK modes, e.g., channel estimators, FFTs, complex multipliers and SD engines. Hence, the additional complexity compared with conventional multi-mode systems is acceptable.
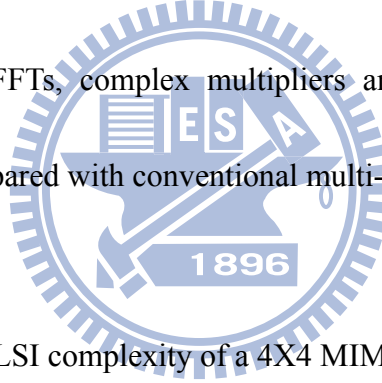
Table 3-1 The VLSI complexity of a 4X4 MIMO OFDM modem

Modules	# of Gates (K)	Ratio	Modes
Channel estimator	22	1.5%	Shared
Complex multipliers	3.5*32=112	7.7%	Shared
Sphere decoder	260x4=1,040	71.3%	Shared
QR operations	70*4=280	19.2%	MIMO-OFDM
Preamble reconst.	5	0.3%	SC-FDE
SRAM	**Size (bytes)**	**Ratio**	**Modes**
SRAM1	10,240	66.7%	Shared
SRAM2	5,120	33.3%	SC-FDE
ROM	**Size (bytes)**	**Ratio**	**Modes**
ROM1	80	1%	SC-FDE
ROM2	7,680	98.%	SC-FDE
ROM3	80	1%	MIMO-OFDM

3.5 Summary

The contributions of this chapter are to design and implement the proposed FD-CE and DF-AC for providing the equalization and decoding of non-CP SCBT over frequency domains. Only one N-point FFT ($M \leq L \leq N/2$) is required to make the SC-FDE integrate with an MIMO-OFDM modem efficiently, ensuring IEEE 802.11VHT multi-mode and backward compatibility. Evaluations of a linear (8, 4) code and Wi-Fi in frequency-selective fading indicate that all results satisfy 8% PER to assure adequate performance within acceptable complexity. Moreover, this work is also corresponded to Giga-bit wireless specification discussed in IEEE 802.15.3c to support OFDM and non-OFDM packet accesses.

Chapter 4

A Cluster-based Pre-pruning Scheme for Low Complexity K-best Algorithm
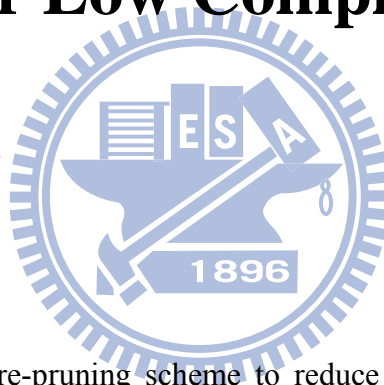
This chapter proposes a pre-pruning scheme to reduce the search space of K-best algorithm. Based on the property of multilevel structure in N_q-QAM constellation, the scheme adopts a cluster-based search to find the reliable constellation points according to the ZF detection results. The set of reliable constellation points then becomes the search space for K-best algorithm and the set size is adaptively chosen according to the accuracy of ZF detection. For the simulation with frequency selective fading, PER loss derived from MLD algorithm and the number of average search nodes used in K-best algorithm are used to evaluate the performance and complexity,

respectively. Compared to the conventional K-best algorithm with the same K value, the proposed work achieves the same performance with fewer search nodes (75%~85% of the conventional K-best algorithm). Moreover, a performance gain (0.25 dB) can be obtained for the case of K=12 when less reduction of search nodes is adopted (84.56%~89.7% of the conventional K-best algorithm). Hence, this work is attractive for those receivers equipping with both K-best and ZF detectors.

Recently, multiple-input multiple-output (MIMO) architecture has been adopted widely in many wireless communication systems because of its high spectrum efficiency. To exploit more spectrum efficiency, larger number of antennas and/or higher order QAM constellations are often employed, which leads a challenge to design the signal detection methods with acceptable complexity and sub-optimal performance.

Various approaches are explored to detect MIMO signals [36]. For linear detection approaches, Zero-Forcing (ZF) or Minimum Mean Square Error (MMSE) uses the inverse of estimated channel response to extract the desired signals. Both of these two approaches are simple to implementation, but with significantly performance degradation caused by enhanced noise. The ordered successive interference cancellation (OSIC) algorithms, e.g., V-BLAST [37], ZF-SQRD and MMSE-SQRD show better performance than linear detection methods, but they

suffers from the error propagation problem [36]. Another category follows the principle of maximum likelihood (ML) and performs with optimal or near-optimal performances. The exhaust searching method, called maximum likelihood detection (MLD), gains the optimal performance with the intractable computation complexity [38]. The sphere decoder (SD) method [39], having the same performance as MLD, attempted to reduce the search space by searching the candidates that lie within the radius. However, SD method is not suitable for real time detection and VLSI implementation since the detection throughput is not a constant depended on the channel realization and SNR condition. On the other hand, K-best algorithm [40] has a fixed computation complexity favored by the pipelined VLSI implementation. Meanwhile, its performance can be very close to SD but with a large K value. Therefore, a number of methods for low complexity K-best algorithms are proposed in the literature. For example, the K-best SE detector uses the ZF detection as an initial estimation [41], the work [42] utilizes the ZF detection to obtain an efficient path extension algorithm with the approximate path metrics, and the method [43] performs K-best search with multiple quadrant detection.

Many current wireless standards specify minimum error rates to insure all standard-compatible receivers can provide acceptable system performance for practical applications [5], [81]. For the ill-conditioned channel or low SNR

environments, the SD and K-best can provide the best performance. However, it may

be unnecessary to adopt those optimal or near optimal algorithms over a good channel

in the case of acceptable performance requirement. Therefore, the solution of the

MIMO receiver supporting both K-best and ZF algorithms has been proposed in the

work [82] to provide just-acceptable error rate (JAER) performance. The average

computational cost can be minimized by adaptive algorithm switch according to the

estimated channel state information. However, the VLSI implementation cost of such

approach increases due to the implementation of two algorithms.

To reduce the increasing implementation cost, this work utilizes the ZF detection

to reduce the complexity of K-best algorithm. A cluster-based pre-pruning scheme is

proposed for reducing the search nodes in conventional K-best algorithm by

employing the ZF detection results with the multilevel structure of N_q-QAM

constellation. This work adopts a cluster-based search to find out the candidate

constellation points that close to the ZF estimation results (the clusters are defined

according to the multilevel structure of N_q-QAM constellation). The candidate

constellation points are then detected by the conventional K-best algorithm while

other residual points in the QAM constellation will be pruned from the K-best search

tree. The set size of candidate points is adaptively changed with the error distance

between ZF estimation and its sliced one. Therefore, fewer search nodes can be

achieved in this work when the same K is used in conventional K-best algorithm. Furthermore, the proposed cluster-based pre-pruning scheme operates likes a front-end signal processing for conventional K-best algorithm. The K-best algorithm used in this work can be easily replaced by other existing K-best algorithms with only slight modification of path extension rule for the found candidate points. Hence, this work is very attractive to the low complexity MIMO applications, which might needs to further reduce the computation complexity of existing K-best algorithms.

The organization of this chapter is described as follows. Section 4.2 reviews the background of MIMO signal detection. Section 4.3 depicts the proposed adaptive cluster-based algorithm for low complexity K-best algorithm. The performance and complexity simulations are presented in Section 4.4. Finally, conclusions are drawn in Section 4.5.

4.1 Background

4.1.1 MIMO System Model

Considers a MIMO-OFDM system with N_T transmit antennas and N_R receive antennas. Let $\mathbf{x} = \left[x_1, x_2, ..., x_{N_T} \right]^T$ ($[\cdot]^T$ means transpose) be the transmitted symbol vector, and

each x_i is chosen independently from *N*-QAM constellation points. For a quasi-static Rayleigh fading channel, the baseband equivalent received vector **y** can be modeled as

$$\mathbf{y} = \mathbf{Hx} + \mathbf{n} \tag{4.1}$$

where $\mathbf{y} = \left[y_1, y_2, ..., y_{N_R} \right]^T$ denotes the received signal vector in the multi-dimensional received signal space, $\mathbf{n} = \left[n_1, n_2, ..., n_{N_R} \right]^T$ indicates an independent identical distributed (i.i.d.) complex zero-mean Gaussian noise vector with variance σ^2 per dimension, and **H** represents the $N_R \times N_T$ MIMO channel matrix with independent elements of h_{ij} representing the representing the complex transfer function from *i*-th transmitted antenna to *j*-th received antenna. For presentation purposes, the channel matrix H is considered to be perfectly estimated at the receiver and is of full rank.

4.1.2 Multilevel Structure of the N-QAM Constellation

For N_q-QAM constellation, it can be naturally partitioned into four *N*/4-QAM ones. Then, those *N*/4-QAM partitions can be recursively partitioned into four sub-partitions until each sub-partition only including one constellation point. As shown in Fig. 4-1, each partition can calculate a corresponding pseudo-symbol, which is the mean value of its four corresponding pseudo-symbols in the next (lower) level

[83]

$$a_{l,s} = 0.25 \sum_{a_{l-1,k} \in A_{l-1}^s} a_{l-1,k} \tag{4.2}$$

where $a_{l,s}$ is the s-th pseudo-symbol at the l–th level, and A_{l-1}^s is the subset of A_{l-1}

such that $\bigcup_k A_{l-1}^k = A_{l-1}$ and $A_{l-1}^k \bigcap A_{l-1}^n = \varnothing$ where $k, n = 1, \cdots, N_{l+1}$ and $k \neq n$.

A_{l-1} is the set of all pseudo-symbols at the next level, which is defined as

$$A_{l-1} \triangleq \left\{ a_{l-1,1}, a_{l-1,2}, \cdots, a_{l-1,N_l} \right\} \tag{4.3}$$

where $N_l \triangleq N 4^{1-l}$. For the lowest level (l=1), A_1 is exactly A and

$a_{l-1,1} = a_k, k = 1, \cdots, N$. In this work, the group (set) of constellation points locating in

the same QAM partition is called the cluster. Since each cluster mean is equal to the

pseudo-symbol of corresponding partition, this work uses cluster mean to replace

pseudo-symbol for more meaningful expression in the following derivations.
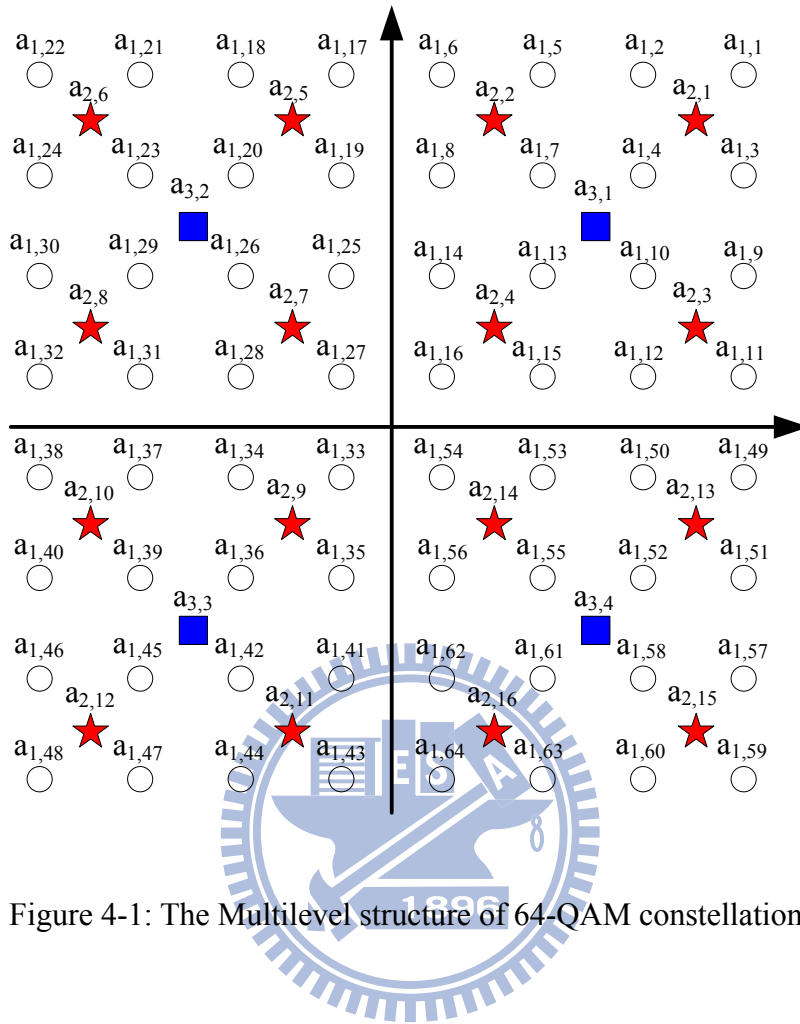
Figure 4-1: The Multilevel structure of 64-QAM constellation.

4.1.3 Conventional K-best Algorithm

By the preprocessing of QR-decomposition, the MIMO detection problem can be

expressed as [40]

$$\hat{\mathbf{x}} = \arg\min_{\mathbf{x} \in \Omega^{N_T}} \left\| \mathbf{y}' - \mathbf{R}\mathbf{x} \right\|^2 \tag{4.4}$$

where $\mathbf{y}' \triangleq Q^H \mathbf{y}$, $\mathbf{R}$ is an $N_T \times N_T$ upper triangular matrix with real diagonal entries r_{ij},

$\mathbf{QR} = \mathbf{H}$, $\left\| \cdot \right\|^2$ is the operation to calculate Euclidean distance and Ω is the set of

N-QAM constellation points. Equation (4.4) can be rewrote as

$$\hat{\boldsymbol{x}} = \arg\min_{\boldsymbol{x}\in\Omega^{N_T}} \sum_{i=1}^{N_T} \left\| y_i' - \sum_{j=i}^{N_T} r_{ij} x_j \right\|^2 \tag{4.5}$$

Instead to calculate the full Euclidean distance in Equation (4.5), K-best algorithm reduces the computation complexity by only calculates the partial Euclidean distance (PED) recursively at each dimension as

$$T_{i-1}(x_{i-1}) = T_i(x_i) - \left\| e_i(x_i) \right\|^2 \tag{4.6}$$

where $\left\| e_i(x_i) \right\|^2$ is the distance decrement, which is obtained by

$$e_i(x_i) = y_i' - \sum_{j=i}^{N_T} r_{ij} x_j \tag{4.7}$$

According to Equation (4.6), K-best algorithm adopts a breadth-first tree search to find the optimal solution of Equation (4.4). Each layer of the tree reveals one of the transmitted symbols (x_i) and each node in the tree corresponds to a distance metric ($T_i(x_i)$). Similar to the sphere decoder, only those possible transmitted symbol vectors that are inside a hyper-shpere (C) will be searched. The value of C is obtained by calculating the full Euclidean distance between received signal and an initial estimation, i.e. decision with zero-forcing [39]. The search process begins from root node with the initial distance $T_{N_t}(x_{N_t}) = C$ and travels down to the leaves with final metric $T_1(x_1)$. During the searching, the node with negative $T_i(x_i)$ is pruned and disabled for further expanding. Moreover, only K nodes with the largest value of

distance metric are kept in each layer. The path from root to the lead node that has the largest $T_1(x_1)$ is the decoding result.

4.2 The Proposed Algorithm

As mentioned above, N_q-QAM constellation has a nature multilevel structure. As shown in Fig. 4-2, the multilevel structure can be represented by a cluster tree. Each tree node is the cluster mean corresponding to a certain partition in the QAM constellation and the leaf nodes also represent the constellation points. Then, the proposed cluster-based detection scheme adopts a breadth-first tree search to find out the survivor leaf nodes and filter out the unreliable leaf nodes that locate far away the correct transmitted symbols. The survivor leaf nodes are preserved to be the search set for more accurate but more computation-consuming detection algorithm, i.e. K-best algorithm. Those unreliable leaf nodes are pre-pruned from k-best search tree before k-best algorithm is performed. Therefore, the proposed method includes two stages: 1). pre-pruning stage with cluster-based detection to roughly obtain the set of reliable constellation points; 2). detail matching stage with the k-best algorithm to find the exactly detection result among the set found by pre-pruning stage. In the subsequent sub-sections, the process of the two stages will be detailed.
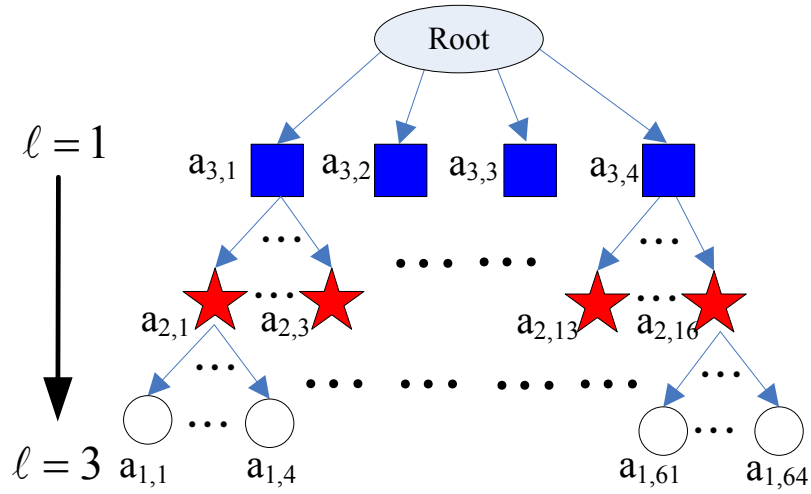
Figure 4-2: The cluster-based search tree corresponding to the multilevel structure of 64-QAM constellation

4.2.1 Pre-pruning via Cluster-Based Detection

The basic idea of this stage is to obtain a roughly collection of reliable constellation points via a computation-effective algorithm, e.g., ZF detection. The ZF detector recovers the transmitted signal vector with the channel matrix as

$$\tilde{\mathbf{x}} = \mathbf{H}^\dagger \mathbf{y} = \mathbf{x} + \mathbf{H}^\dagger \mathbf{n} \tag{4.8}$$

The ZF requires very little computation complexity, but it can not provide an accurate estimation. The proposed method finds the candidate clusters that include or close to the ZF estimation result $\tilde{\mathbf{x}}$. The decision of candidate clusters can be more tolerant to the inaccurate estimation $\tilde{\mathbf{x}}$ since the distance between each cluster mean is larger

103

than that between each constellation points.

For the first layer ($\ell = 1$) of the cluster search tree, only the phase of the ZF estimation result is used for searching candidate clusters since the first level cluster nodes just locate in four quadrants of I-Q plane, respectively. Hence, the phase detection rule can be described as

$$\Lambda_j = \begin{cases} \{a_{1,1}, a_{1,2}, a_{1,4}\}, & 0 \le \theta(\hat{x}_j) < \pi/2 \\ \{a_{1,1}, a_{1,2}, a_{1,3}\}, & \pi/2 \le \theta(\hat{x}_j) < \pi \\ \{a_{1,1}, a_{1,3}, a_{1,4}\}, & -\pi/2 < \theta(\hat{x}_j) \le 0 \\ \{a_{1,2}, a_{1,3}, a_{1,4}\}, & -3\pi/2 \le \theta(\hat{x}_j) < -\pi/2 \end{cases} \quad (4.9)$$

where $\tilde{x}_j$ is the i-th dimension element of $\tilde{\mathbf{x}}$, $\theta(\bullet)$ is the phase operation, Λ_j is the set of first level cluster candidates of x_j, and $a_{1,k}$, $k = 1, \cdots, 4$, are the first level cluster mean in the upper right, upper left, lower left and lower right quadrants of the I-Q plane, respectively. Then, only the cluster candidate in set Λ_j are allowed to extend their child clusters (at level 2) for next level cluster matching. Since the phase detection can be achieved by checking the sign of the I and Q components of $\tilde{\mathbf{x}}$, this process can be much less complex than calculating the squared Euclidian distance. However, the phase detection scheme is only applied in first level cluster matching. The reason is that the decision boundaries of higher level clusters are too small which makes the higher level cluster matching sensitive to the inaccurate phase estimation caused by the ZF detector.

When the layer number ℓ is larger one (i.e., $\ell = 2$), the cluster tree search is

based on the Euclidean distance metric between the ZF estimation result $\tilde{x}_j$ and each cluster mean at current layer. For current layer, only the nodes that extended from upper layer (parent nodes) need to be calculated the metric. The nodes at current layer with P_j smallest metric values are selected as the candidate nodes for cluster tree searching at next layer. According to the j-the dimension error distance (Δ_j), P_j is adaptively calculated by

$$P_j = P_{\min} + \left\lfloor \left(\Delta_j / \Delta_{sum} \right) \cdot P_{th} \right\rfloor \tag{4.10}$$

where $P_{\min}$ is the minimum candidate cluster number for each dimension, P_{th} is the overall extra-candidate cluster number for all dimension, and Δ_{sum} represents a summation of all error distance at each dimension. The j–th dimension error distance (Δ_j) is defined as

$$\Delta_j = \left\| \tilde{x}'_j - \tilde{x}_j \right\| \tag{4.11}$$

where $\tilde{x}'_j = Q_s \left(\tilde{x}_j \right)$ and $Q_s(\bullet)$ is a function of QAM slicer, which quantizes each element of $\tilde{x}_j$ to the nearest constellation symbol. Meanwhile, the total error distance Δ_{sum} can be obtained by

$$\Delta_{sum} = \sum_{j=1}^{N_T} \Delta_j \tag{4.12}$$

In general, ZF detection can provide trustworthy estimation when the SNR is high or channel condition is good. If ZF estimation result is credible, P_j is expected to smaller, i.e., $P_j \approx P_{\min}$. It means P_{th} should be adaptive adjustment according to the

105

ZF estimation result. Therefore, P_{th} is defined as

$$P_{th} = \left(\Delta_{sum}/\Delta_{th}\right)\cdot P_{extra} \tag{4.13}$$

where P_{extra} is the basis of overall extra-candidate cluster number for all dimension,

and Δ_{th} is a overall error distance threshold. Then, Equation (4.10) can be rewritten

as

$$P_j = P_{min} + \left(\Delta_j/\Delta_{th}\right)\cdot P_{extra} \tag{4.14}$$

The tree search stops until the leaf nodes are reached. The candidate leaf nodes that

extended from the survivor nodes at upper layer can be viewed as the constellation

points that nearby the transmitted symbol, i.e. the black points in the Fig. 4-3.

4.2.2 Detail Matching with K-Best Algorithm

For the detail matching stage, a conventional K-best algorithm is performed in the

received signal space to obtain the final estimation result with more accurate detection

performance. As shown in Fig, 4-3, the search set of the K-best algorithm becomes

the set of candidate constellation points obtained by the cluster-based tree searching.

The search set of the K-best algorithm consists of all symbols of N_q-QAM

constellation for each layer. It also means all nodes of each layer need to be calculated

their PED. However, only K PED calculation results can affect the decision of the

survivor paths in the next layer. In order to decrease the redundant PED calculations,

the k-best algorithm only calculates the PED with the nodes that close to the transmitted symbol candidate (candidate leaf nodes in cluster-based detection). The algorithm steps of the K-best algorithm with cluster-based pre-pruning are presents as follows:

1) Compute the ZF output $\hat{x}$, and then calculate the radius (radius = $\left\| \mathbf{y} - \mathbf{H}\hat{\mathbf{x}} \right\|^2$) for K-best algorithm.

2) Pre-pruning stage using cluster-based detection. For each dimension $j = 1, \cdots, N_T$,

    i) According to Equation (4-9), perform phase detection to obtain the candidate nodes in first layer ($\ell = 1$).

    ii) Calculate P_j according to Equation (4-14).

    iii) For $1 < \ell < N_T$, breadth search candidate cluster nodes with P_j smallest Euclidean distance metric values at each layer of cluster tree.

3) Detail matching stage using K-best algorithm, For each K-best search tree layer $j = 1, \cdots, N_T$

    i) Extend paths from the upper layer according to the leaf candidate nodes found in the cluster-based detection

    ii) Delete the extended paths whose metrics are larger than the radius calculated in step1.

    iii) If the number of remaining paths is larger than K, sort the extended paths in ascending order based on the Euclidean distance metric and select the K paths with smallest metric values as the candidate paths at current layer. Otherwise all the remaining paths are candidate paths.

For the step 3.i, it can be observed that the path extension process is different to the conventional K-best algorithm which extends all QAM constellation points. However, the other two sub steps (3.ii and 3.iii) are the same as conventional K-best algorithm. It means that the K-best algorithm used in this work can be easily replaced by other existing K-best algorithms with only slight modification of path extension rule for the found candidate points.

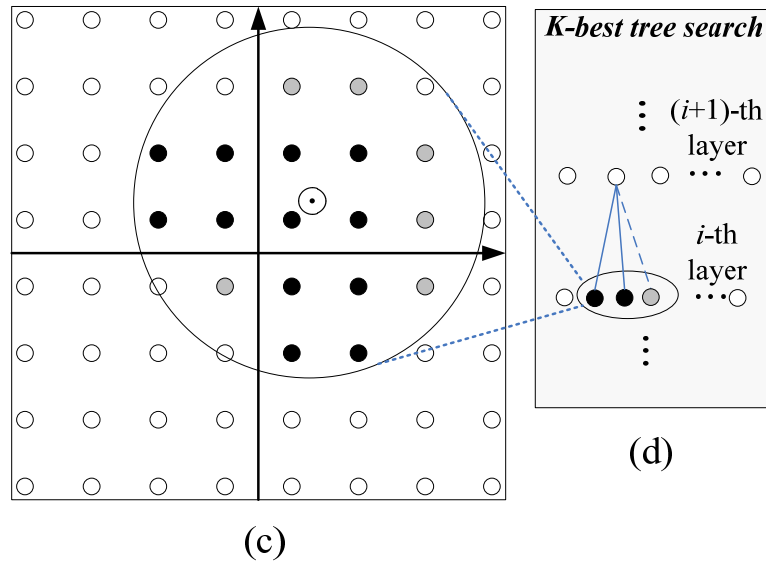(a)   (b)

(c)

(d)
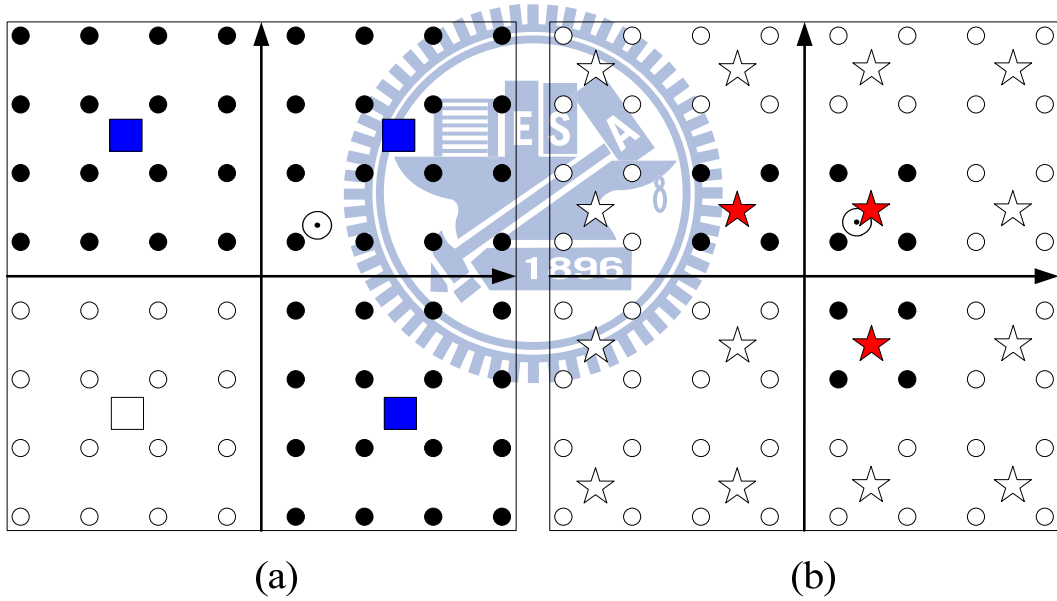
Figure 4-3: The behavior of cluster-based detection where the black points are the candidate points at that stage. (a) after the first-level detection. (b) after the second-level detection (c) the conventional K-best algorithm searches both of the gray and the black nodes in the search radius. (d) The path extension procedure in this work, where the solid lines represent the valid path extension and the dash line represents the invalid path extension due to the pre-pruned in cluster-based detection.

4.3 Simulation Results

To reveal the feasibility in MIMO-OFDM systems, our method is simulated in IEEE 802.11n/ac (4x4 MIMO OFDM) platform. The basis of our performance is the packet error rate (PER) that is required to be 8% in IEEE TGn Channel model [52]. The simulations are assumed that the channel is static during a packet period and the

channel state information is available at the receiver.

From the Equation (4.14), it can easily see that Δ_{th} will dominate the candidates

cluster number, which directly decides the size of search space for K-best algorithm in

the detail matching state. In order to find a suitable value of Δ_{th}, the cumulative

distributed function (CDF) of error distance between ZF estimation result and its

sliced one is evaluated in Fig. 4-4, including three cases of overall, correct, and wrong

detections. The CDFs shows the ZF detection becomes unreliable when error distance

is larger than 1. Therefore, Δ_{th} is suggested to be 1 to avoid the wrong ZF

estimations degrading the overall PER performance.

Figure 5 and 6 presents the performance and computation complexity in terms of PER

and the number of average search nodes. The default configurations of the proposed

method are set as $P_{\min} = 4$, $P_{extra} = 12$, except for the simulations of Δ_{th}=0.8 with

K=24 and Δ_{th}=0.6 with K=12, which uses $P_{\min} = 6$ and $P_{extra} = 16$ to gain more

robust perfomance. In Fig. 4-6, the MLD PER performance is performed by the

sphere decoding algorithm. The simulation results show that the conventional K-best

algorithm can achieve near-MLD performance with K=24, and about 0.65 dB SNR

loss (compared to ML) with K=12. Base on the same K values, the proposed method

with $\Delta_{th} = 0.8$ presents the similar performance with fewer average search nodes.

For example, the proposed method at SNR 22 dB only requires 84.56% and 85.06%

search nodes of the conventional K-best algorithm with K=12 and 24, respectively.

Moreover, the percentages of search node further decreases to 75%% and 78.03%

when SNR up to 30 dB. The reason is ZF estimation will become more accurate (Δ_j

becomes smaller) when SNR increases. Then P_j is adaptively decreased which leads

to a smaller search space for K-best algorithm. Table 4-1 summarizes the performance

degradation at PER = 10%, 8% and 1%, and the corresponding complexity reduction

compared to K-best algorithm with K=24. The PER performance and the number of

search nodes is a tradeoff in the proposed method. Compared to the proposed method

with $\Delta_{th} = 0.8$ and K=12, 11.83%~14.42% of search nodes can be further reduced

when Δ_{th} is relaxed to 16. However, the SNR loss derived from MLD increases to

1.1 dB at PER 8%. Finally, the proposed method with the $\Delta_{th} = 0.6$ and K=12 can

improve 0.25 dB SNR gain but with less search nodes compared to the K-best

algorithm using same K value at PER 8%. The reason is our method reduces the

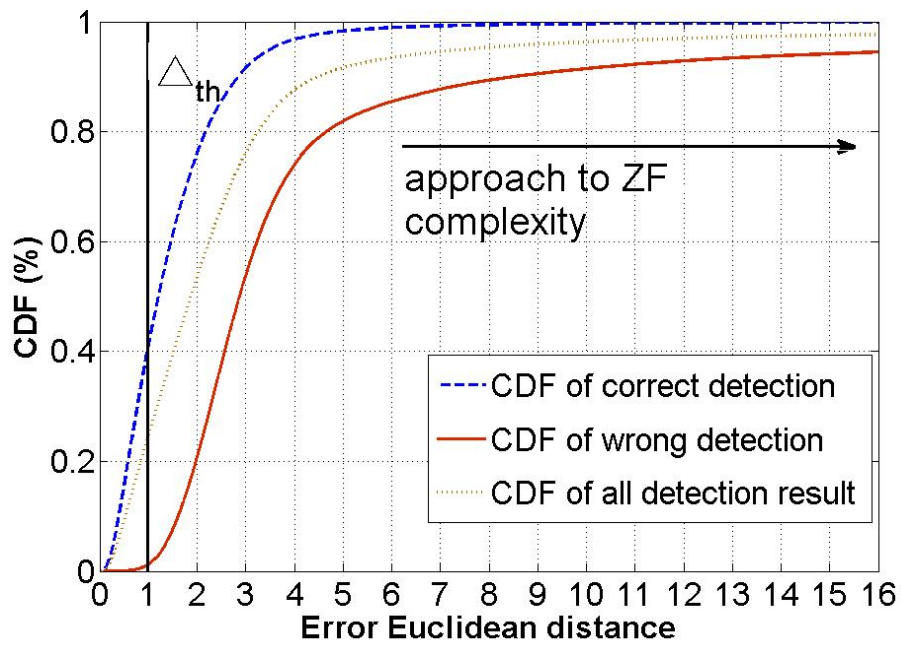probability of irreducible path selection errors in the conventional K-best algorithm

[84].

Figure 4-4: CDF of error distance between ZF estimation result

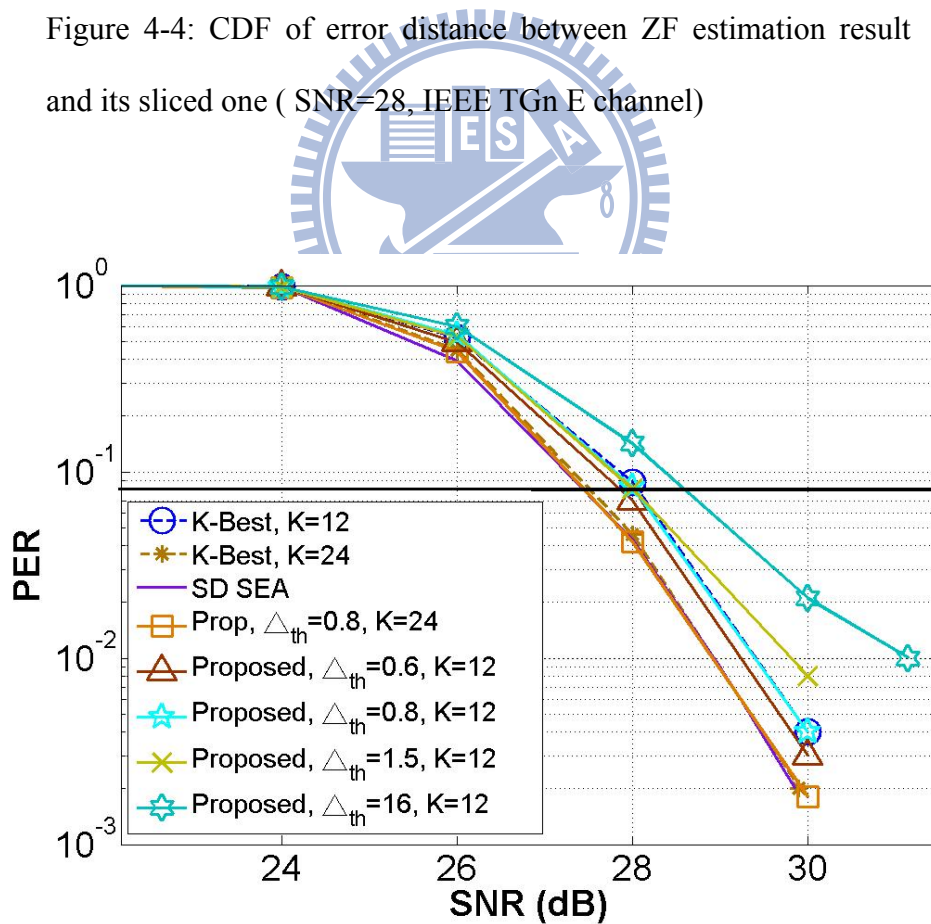and its sliced one (SNR=28, IEEE TGn E channel)

Figure 4-5: PER performance with 4x4 64-QAM in IEEE TGn E
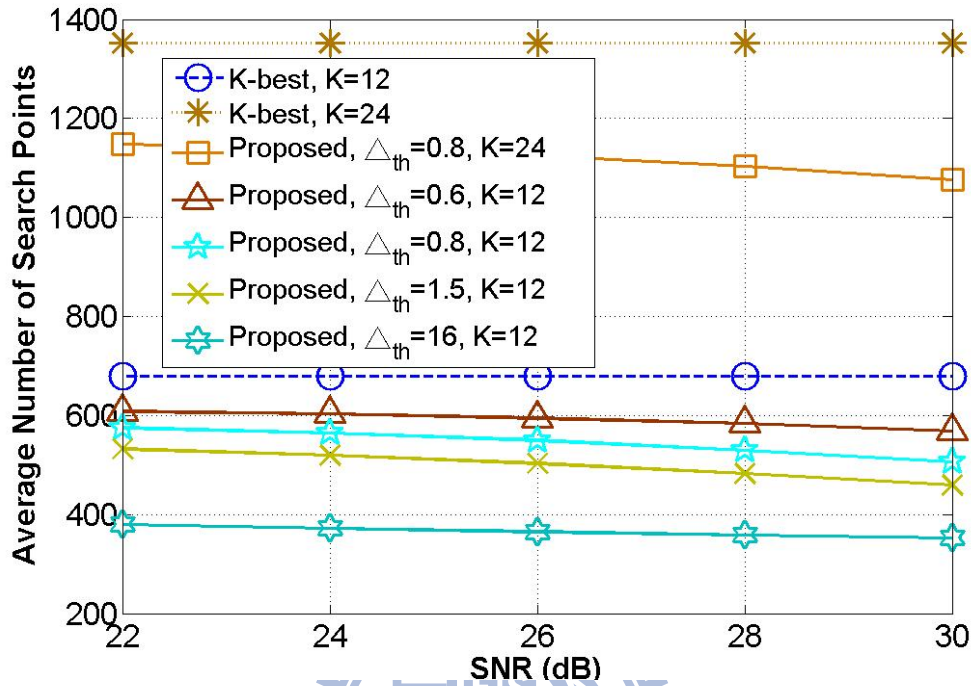
channel with 100-ns.

Figure 4-6: Comparison of complexity in terms of the number of

search points for 4x4 64-QAM K-best search tree in IEEE TGn E

channel with 100-ns

Table 4-1: Performance and Complexity Comparisons

Approach (parameter)	Deviation from ML at PER X%			Complexity compared with K-best (K=24)
	PER=10%	PER=8%	PER=1%	
K-Best with K = 24	<0.1 dB	<0.1 dB	<0.1 dB	100%(1352)
Proposed (Δ_{th}=0.8 K=24)	<0.1 dB	<0.1 dB	<0.1 dB	78.03%(1055) ~85.06%(1150)
K-Best with K =12	0.65 dB	0.6 dB	0.5 dB	50.3% (680)
Proposed (Δ_{th}=0.8 K=12)	0.6 dB	0.55 dB	0.5 dB	37.72%(510)~42.53%(575)
Proposed (Δ_{th}=0.6 K=12)	0.35 dB	0.35 dB	0.3 dB	42.53%(575)~45.11%(610)
Proposed (Δ_{th}=1.5 K=12)	0.59 dB	0.55 dB	0.95 dB	34.02%(460)~39.30%(530)
Proposed (Δ_{th}=16 K=12)	1.15 dB	1.15 dB	2.25 dB	25.89%(350)~28.11%(380)

4.4 Summary

This work provides a further complexity reduction way for those receivers equipping with both K-best and ZF detectors. Using ZF detection result, a cluster-based pre-pruning scheme is proposed to reduce the computation complexity of conventional K-best algorithm. Simulation results show the proposed algorithm reduces the search space while still providing near MLD performance with a marginal PER loss compared to conventional K-Best algorithm. Moreover, the cluster-based pre-pruning scheme is easily applied to most existing K-best algorithm with only slight modification of path extension rule. Hence, this work is also very attractive to the low complexity MIMO applications, which might needs to further reduce the computation complexity of existing K-best algorithms.

Part II MAC Layer:

Development/Deployment of an

IEEE 802.11s System
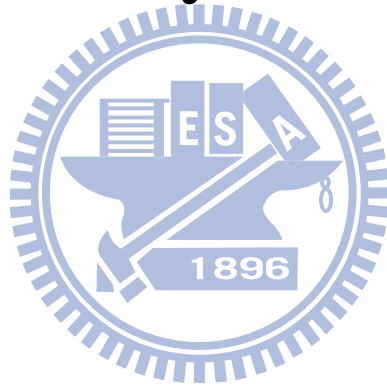
Chapter 5

Design and Implementation of

IEEE 802.11s Mesh
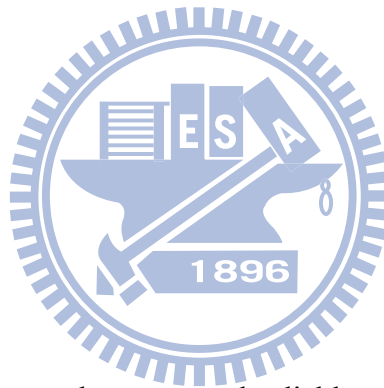
Wireless mesh networking, as a low-cost and reliable technology for rapid network deployment, has attracted considerable attention from academia and standardization in the industry. The IEEE 802.11s standard defines a wireless LAN mesh [8] (WMNs) using the IEEE 802.11 medium access control and physical layers, and is one of the most active standards with increasing commercial opportunities. The standard has drawn numerous research and commercial interests in recent years. Unlike ad hoc networks and sensor networks that are motivated by military or crisis applications, WMNs introduce the commercial applications such as the last-mile wireless access or

home wireless networking. WMNs can largely reduce the cost and complexity of network deployment by multi-hop relaying.

Prior studies, such as the mesh on XO-laptop for One Laptop per Child (OLPC) [44] and the open80211s project for Linux, evaluated the network performance of the IEEE 802.11s mesh. However, no studies examine system architectures and mesh stability. The system proposed in this chapter is developed based on the draft D2.03 of IEEE 802.11s, and extends the functions of commercial off-the-shelf WLAN chipsets. The proposed extension is a pure software solution that integrates with a WLAN driver. Considering the portability of the proposed solution and the stability of the software during the system development phase, this chapter proposes a modularized design that separates mesh functions into a driver and a user-space program. Using this system prototype, this chapter establishes a real testbed and further investigates design and implementation issues that influence system performance. Results show that transmitting mesh broadcast-type control frames over a multihop wireless mesh without acknowledgment can cause network stability problems. In a 16-node interference-intensive grid topology, for example, 14 percent of path request messages are lost, and not all routing paths are found even when broadcasting at the most reliable data rate (i.e., 1 Mb/s). Therefore, this study evaluates the feasibility of replacing unacknowledged broadcast with multiple acknowledged unicasts for mesh

broadcast-type control messages. Another issue is the serious interference between

mesh nodes sharing the same channel. To reduce this interference, the study also

examines the effectiveness of transmitting packets using a single radio interface

switching between multiple channels.

The rest of this chapter is organized as follows. The next section briefly presents

the key features of IEEE 802.11s. We then discuss the design and implementation

issues of a WLAN mesh. We then present the experimental results, and the final

section provides the conclusion.

5.1 Network Architecture
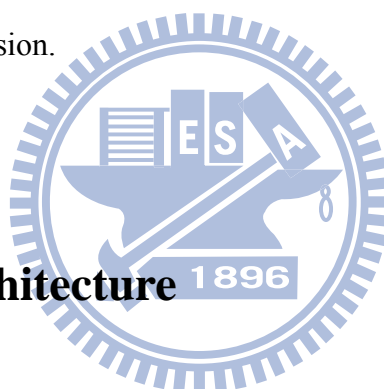
IEEE 802.11s [14] defines an IEEE 802.11-based WMN that supports broadcast and

unicast delivery over a self-configured multihop link-layer topology. As Fig. 5-1

shows, an IEEE 802.11s mesh network contains three types of nodes: the mesh point

(MP), mesh access point (MAP), and mesh portal (MPP). The MP is the basic mesh

unit that provides topology construction, routing, and data forwarding. This type of

node can also be designed as a terminal device for end users to directly connect with

peer MPs and access the mesh. Non-mesh IEEE 802.11 stations (STAs) must first

associate with a MAP, which is an MP capable of IEEE 802.11 access point (AP)

functions, before accessing a mesh. An MPP is an MP integrated with gateway

functions to interoperate with external IEEE 802 LANs. The MP, MAP, and MPP are

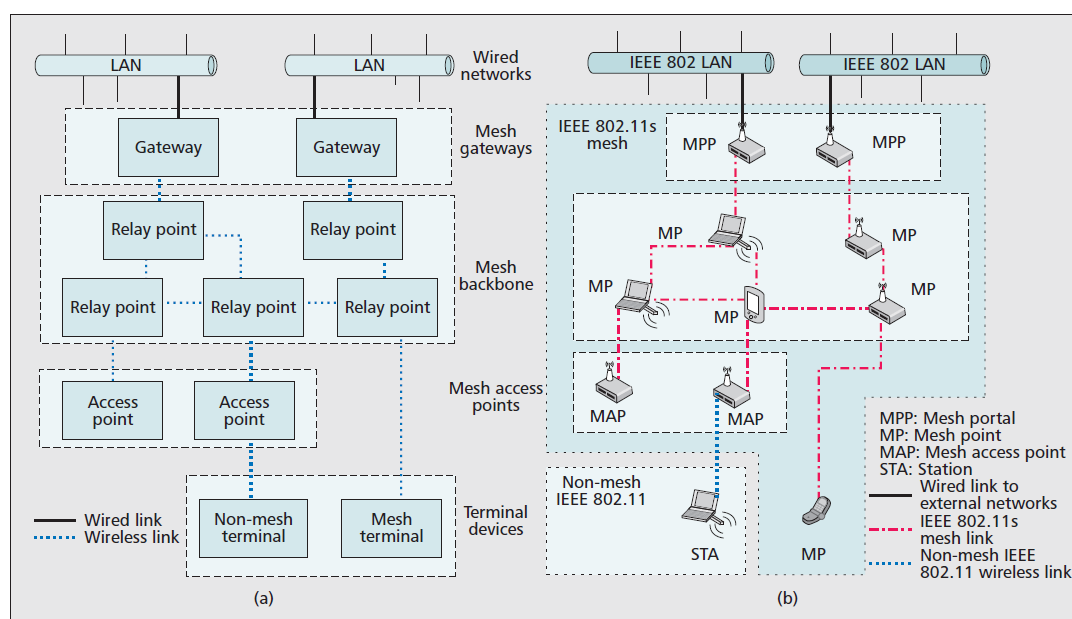all logical components, and some of them can be physically collocated.

Figure 5-1: A logical view of a wireless mesh network and its mapping to IEEE

802.11s: a) a generic mesh network; b) an IEEE 802.11s

5.2 Mesh Functions

Network Link Construction

The IEEE 802.11s standard specifies the boot sequence procedure for an MP joining a

mesh network based on the procedure for an STA associating with an AP in a

conventional non-mesh WLAN. First, an MP performs an active or passive scan to obtain a list of existing MPs in each channel. Next, the MP uses the *mesh peer link management* protocol to associate with an MP matching its own preferences. This protocol behaves like the conventional IEEE 802.11 association procedure. The only difference is that the mesh peer link management protocol uses several new management frames. These frames encapsulate mesh-specific information, such as a mesh identifier, while removing unrelated parameters, such as a service set identifier (SSID). After a successful association with a neighboring MP, the MP becomes a member of an IEEE 802.11s mesh network.

IEEE 802.11s introduces the unified channel graph (UCG), which presents one mesh sharing the same preferences in the same channel, to handle several meshes spanning different channels. When forming a new mesh, the initial MP randomly decides a channel precedence value and embeds that value in the management frames. After the channel scan, other MPs select the channel with the highest precedence as their operating channels. This procedure forms a UCG called the *simple channel unification* protocol. To resolve multiple UCGs in different channels due to spatial division and the needs of channel switching, such as radar detection, IEEE 802.11s proposes a *channel graph switch* protocol. In this protocol an MP sets a waiting timer and broadcasts a mesh channel switch announcement. The announcement contains the

waiting period and a precedence value of the candidate channel. When the timer

expires, the MPs receiving the announcement switch to a candidate channel with the

highest precedence.

<u>Routing</u>

IEEE 802.11s defines a *path selection* framework that flexibly allows vendors to

implement proprietary routing metrics and protocols to meet special needs. The

communication between two MPs begins with the construction of a routing path.

Then the data frames are transmitted along with the routing path via neighboring MPs.

Hybrid Wireless Mesh Protocol (HWMP) is the mandatory routing protocol

recommended by IEEE 802.11s. This protocol comprises an *ondemand* routing

procedure to construct a path between two arbitrary nodes and a *proactive* extension

to speed up the initial connection. The on-demand routing procedure is derived from

Ad Hoc On-Demand Vector (AODV) [80], but it works on the link layer and adopts a

radio-aware metric called the airtime link metric. This metric considers the actual

transmission quality in terms of transmission error and data rate. To construct a

routing path from one node to another (e.g., from node s to node t), s broadcasts a

path request message (PREQ) into the mesh. Upon receiving the PREQ, t responds to

s with a path response message (PREP) through unicast transmission. The reverse

routing path from *t* to *s* is first built after *t* receives the PREQ, and the desired routing path from *s* to *t* is created after *s* receives the PREP. Once established, this path can be used before it times out.

The proactive extension of HWMP actively forms a *routing tree* rooted at an MP by periodically broadcasting root announcement messages. Under the HWMP, a unicast packet without a valid on-demand routing path can be transmitted to the root first. The root then forwards the packet along the tree to its destination. Meanwhile, an on-demand routing procedure is performed between the source and destination to create a direct routing path. This help from the root may reduce latency before the direct ondemand routing path is established [86].
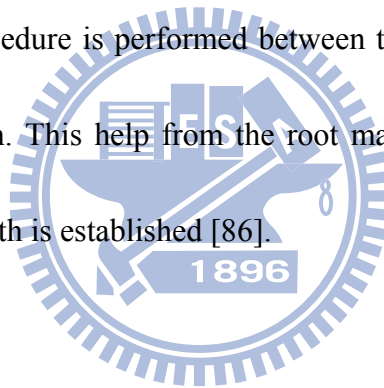
Interworking

IEEE 802.11s also defines an interworking procedure to handle the communication between two terminals in which at least one is bridged by an MPP. A terminal bridged by the MPP is called a *proxied entity*. IEEE 802.11s assumes that an MPP can learn all proxied entities it bridges. In addition, every mesh node has a proxy table that maintains the relation between a proxied entity and its MPP.

To transmit a packet from a mesh node *s* to a proxied entity *t*, the interworking procedure on *s* first performs the HWMP to issue a PREQ to request the path to *t*. If

no MP responds to the query (e.g., the proxied entity has not been learned), the packet

is forwarded to one or more MPPs and then bridged to their attached external

networks. Otherwise, the corresponding MP, *b*, replies to s with the PREP. Then *s*

inserts the relation, *b* bridges *t,* into its proxy table. Once the relation exists, the

packet can be delivered from s to *b,* and then b bridges the packet to *t*.

Data Frame Format

IEEE 802.11s introduces a mesh header subfield in the beginning of the frame body to

address multihop transmissions. When convoying packets whose source and

destination are both inside the mesh, the subfield indicates that the 4-address format in

the frame header is used. The frame header includes the MP addresses of the next-hop

receiver, transmitter, destination, and source, and is processed by MPs as it would be

in a wireless distribution system (WDS). Otherwise, the subfield contains two

additional addresses to encapsulate the addresses of proxied entities. When a packet

enters or leaves a mesh, the sender and receiver addresses are enveloped into or

recovered from the subfield.

Flooding Control

The fact that an MP blindly retransmits broadcast frames to its neighbors may cause

endless flooding due to the loop structure of a mesh topology. To avoid infinite rebroadcasting, the source MP first tags a 32-bit incremental sequence number, called the Mesh Sequence Number field, on each frame before transmitting it. Other MPs can use this field and the source MP address as a unique signature to avoid duplication. The source MP also transmits the Mesh Time to live field, a counter decreased per hop with each frame to limit its longevity. This field acts as a backup mechanism to detect duplication for rollover sequence numbers and limited recording space.

5.3 Design and Implementation Issues of An IEEE 802.11s Mesh

This section first presents the software architecture that considers both portability of the proposed solution and system stability for future extensions. Second, this section discusses the design and implementation issues of the transmission reliability of mesh broadcast-type control frames

5.3.1 Software Architecture

To improve the portability of the IEEE 802.11s software package, a modularized design is required. The proposed design separates *platform-independent* functions

such as HWMP routines from the kernel and implements them as a Linux daemon program, called a path selection daemon. This approach simplifies the development of HWMP algorithms and provides greater flexibility in changing routing algorithms. The user-space daemon also improves system stability since it reduces the chance of kernel crash during the system development stage.

Time-critical functions are implemented in the kernel and *hooked* in the IEEE 802.11 driver. The *boot sequence module* performs the boot sequence procedures to associate the device with an IEEE 802.11s network. The *data forwarding module* relays multihop data and triggers the path selection daemon to construct a routing path when necessary. Last, the *action frame handler module* translates the MAC-layer control frames into module-specific commands and activates other modules to process these commands. Figure 5-2 illustrates the proposed software architecture for the IEEE 802.11s nodes.

To support IEEE 802.11s, the WLAN driver is extended with two components, the mesh manager and the mesh data forwarder (the dotted boxes in Fig. 5-2), for the mesh control plane and data plane, respectively. The mesh manager is responsible for establishing and maintaining links with neighboring STAs. It records the associated STAs in the mesh neighbor table and removes an entry from the table if it does not receive a beacon from that STA for a certain period. When a control frame such as a

routing message is received, it is passed to the action frame handler module to check if the frame comes from an associated neighbor. If the frame is from a validated neighbor, it is then forwarded to the userspace path selection daemon. The daemon updates the routing tables, including the path selection table and proxy table in the kernel space, and issues the corresponding control frames to its neighbors via the action frame handler module and transmission (TX) handler if necessary.

For the data plane, the data forwarding module either dispatches a received data frame to the upper layers of the protocol stack while the node is the destination, or relays it to the next hop. To relay a data frame, the data forwarding module updates the next-hop MAC addresses of the frame by referencing the path selection table, and then the proxy table if the destination is not inside the mesh. The TX handler then transmits the data frame. If not found in both tables, the frame is forwarded to the root and invokes on-demand routing. If the node is the destination or the node (i.e., MAP or MPP) that bridges the frame to the destination on the external network, a data frame is posted to the upper layer of the protocol stack. Finally, an open-source link-layer bridge module, called an Ethernet Bridge, processes the remaining task of bridging traffic between different interfaces. It is also noted that only MPPs have the IEEE 802.3 part, and only MPPs and MAPs have the bridge part.
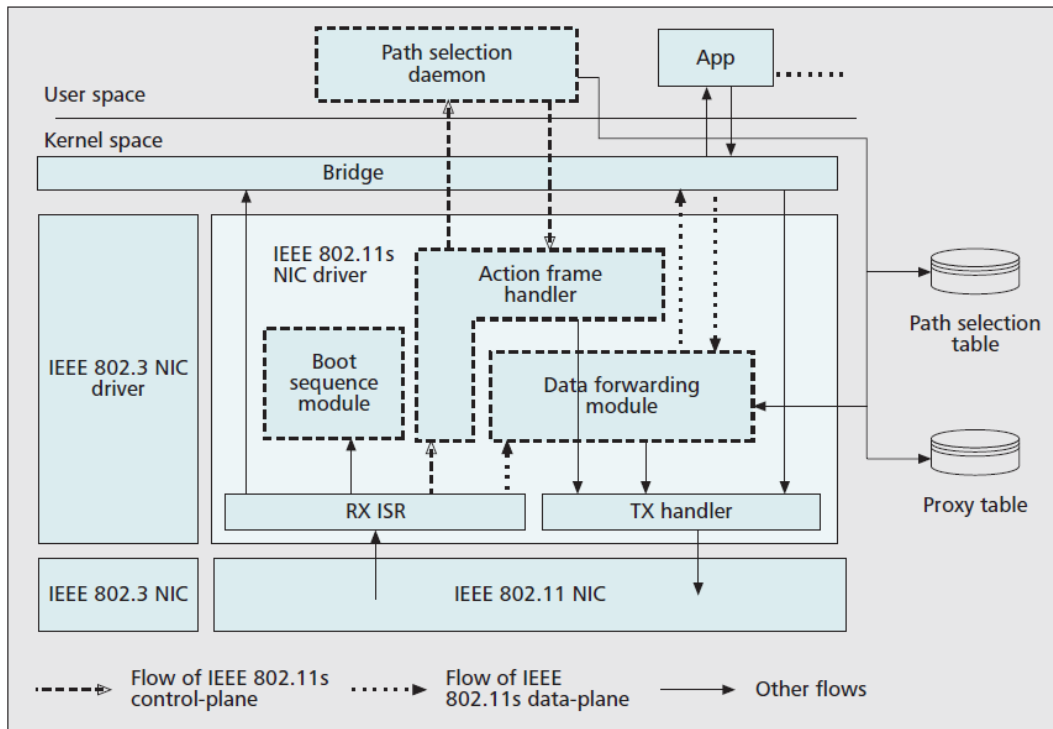
Figure 5-2: The proposed software architecture and the control/data plane flows. The modules in bold text are the IEEE 802.11s extensions.

5.3.2 Transmission Strategies for Mesh Broadcast-Type Control Frames

In the wireless environment, a sender has difficulty detecting a collision on the receiver side. This results in the need for acknowledgment (ACK) and retransmission mechanisms to reduce the packet loss side-effect. However, the IEEE 802.11 broadcasting scheme, called conventional broadcasting in this article, has no ACK. As a result, conventional broadcasting is unreliable and packet loss is high in an

interference-prone environment. Packet loss is cumulative in multihop transmissions, which brings a new challenge to the wireless mesh since some of the IEEE 802.11s control frames are broadcast-type. Thus, the frequent loss of these broadcast-type control frames may result in unstable mesh topology and network.

To improve the transmission reliability of broadcast-type control frames, possible IEEE 802.11-compatible solutions either blindly broadcast the same frame multiple times, called the multiple-broadcast scheme, or unicast it to each neighbor individually, called the multiple-unicast scheme. Both schemes reduce packet loss at the expense of using more wireless resources. The multiple-broadcast scheme might use less wireless resources than the second scheme because it does not require ACK frames, certain inter-frame spaces (IFSs), and retransmissions. However, it must use more robust coding and modulation (i.e., a lower transmission rate) [87] so that the broadcast frames are more likely to be received by all neighbors. On the other hand, the multiple-unicast scheme is able to adopt a higher transmission rate for each individual neighbor. The ACK frames used by this approach also improve transmission reliability.

The proposed design handles the mesh broadcast-type control frames and other broadcast-type frames separately. The mesh broadcast-type control frames (e.g., the routing request frames) are directly generated by the mesh protocols. The other

broadcast-type frames come from upper layers of the protocol stack (e.g., Dynamic

Host Configuration Protocol [DHCP] discovery). The latter are normally less

important, and may inherit different characteristics from applications and services.

Therefore, this study leaves the response to the loss of these kinds of broadcast-type

frames to upper-layer protocols and applies the conventional broadcasting approach.

The transmission reliability of mesh broadcast- type control frames significantly

influences the construction and stability of a mesh network. In addition, the number of

broadcast-type control frames depends on the scale of the mesh, and is relatively

small compared to that of broadcast- type data frames. Therefore, this study applies

and evaluates the multiple-broadcast and multiple-unicast schemes only for mesh

broadcast-type control frames.
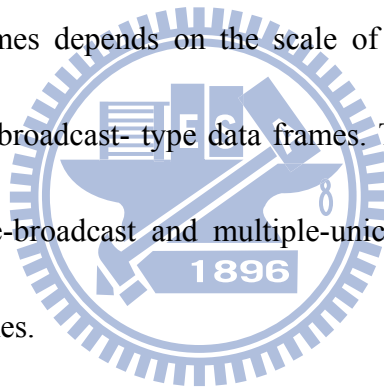
5.4 Development/Testbed Platforms

The testbed used in this chapter implements a WLAN mesh system on both Realtek

RTL8186 and Realtek RTL8192SE+RTL8196B platforms for all STAs, MAPs, and

MPPs. Both of this two platforms runs an embedded Linux (v. 2.4.18). RTL8186

platform is a commercial system-on-a-chip embedded with an Ethernet, a single-radio

802.11b/g   controller,   and   a   180   MHz   32-bit   MIPS   processor.   While

RTL8192SE+RTL8196B platform is a two chip solution, where RTL8192SE is an 802.11b/g/n 2 × 2 (2 transmitters, 2 receivers) Multi-Input Multi-Output (MIMO) WLAN IC integrated with an Ethernet interface and RTL8196B is a 330 MHz 32-bit MIPS processor.

5.5 Experiment of Broadcasting Strategies

5.5.1 Experiment configuration
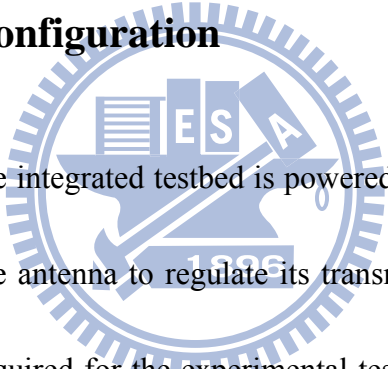
Figure 5-3(a) shows that the integrated testbed is powered by a battery, where a fixed attenuator is attached to the antenna to regulate its transmission power. This greatly reduces the actual space required for the experimental testbed, and makes it possible to conduct small-scale mesh experiments in the laboratory. The traffic generator injects the desired experimental patterns, and the data rate and testbed topology vary in different experiments. Figure 5-3(b) shows the testbed configuration.

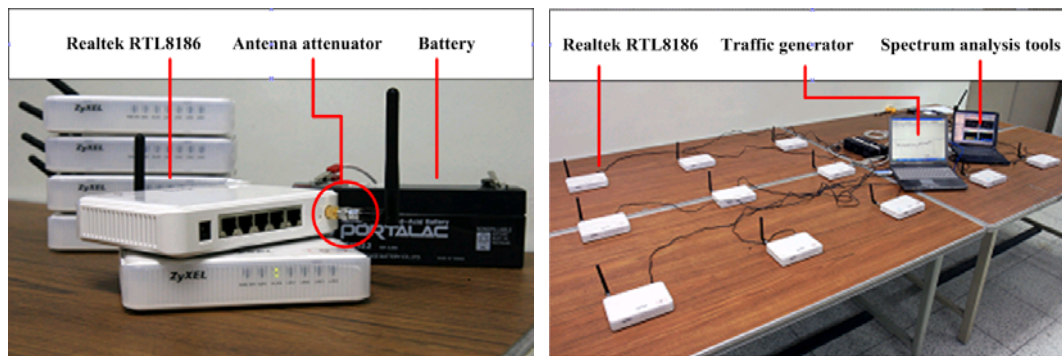Figure 5-3: Illustration of the testbeds: a) experimental mesh node platforms where the Realtek RTL8186 is used in ZyXEL P-330W; b) an experimental deployment.

5.5.2 Evaluation of Broadcasting Strategies

Both the multiple-broadcast and multiple-unicast schemes produce more reliable transmissions than conventional broadcasting. Unlike the multiple- broadcast scheme, which has to broadcast packets using the minimal transmission rate, the multiple-unicast transmission may apply higher and different data rates for individual nodes. The experiments in this section evaluate these two schemes in terms of reliability, routing construction success ratio, latency, and channel utilization.

Figure 5-4(a) depicts the packet error rate (PER) of a one-hop transmission under different IEEE 802.11b/g data rates. The results present the link quality baseline for the following experiments. The results are based on broadcasting 100-byte packets.5

Both the sender and receiver are connected by a 20 dB attenuator, and the distance between each unit is fixed at 70 cm. The received signal strength of each MP ranges from −70 to −80 dBm, which is a common reference value for Wi-Fi network deployment.6 During these tests, a spectrum analyzer detected two APs in the neighboring channels with received signal strengths of −71 and −75 dBm. The signal causes adjacent channel interference (ACI) and increases the PER in wireless transmissions. Under the same channel quality, including signal strength and ACI, the 11b PHY delivers a slower data rate and also lower PER, while the 11g PHY gives higher ones, as Fig. 5-4(a) indicates. Thus, a common practice is to use 11b PHY when the channel quality drops and 11g PHY when it clears up. Experimental results also show that the PER increases significantly when the data rate exceeds 36 Mb/s. To help the multiple-broadcast and multiple-unicast schemes utilize wireless resources more efficiently, the following experiments manually select a maximum of 36 Mb/s for the data rate.

Figure 5-4(b) illustrates the degradation of broadcast reliability for increasing hop counts in a chain topology. Three schemes (i.e., conventional broadcast, multiple-broadcast, and multiple-unicast) are evaluated with various data rates. The packet arrival ratio measured in this experiment represents the percentage of broadcast packets successfully received by the measuring node. The conventional

broadcast scheme at 36 Mb/s has the worst performance in all six configurations. The

two-broadcast scheme significantly improves reliability when using the same data rate.

The result of the multiple-broadcast scheme at 36 Mb/s is comparable to the

conventional broadcast scheme at lower data rates (1 Mb/s and 11 Mb/s) when the

broadcast repetition increases to three. Naturally, the multiple-unicast scheme presents

the best reliability in all configurations, even at 36 Mb/s.
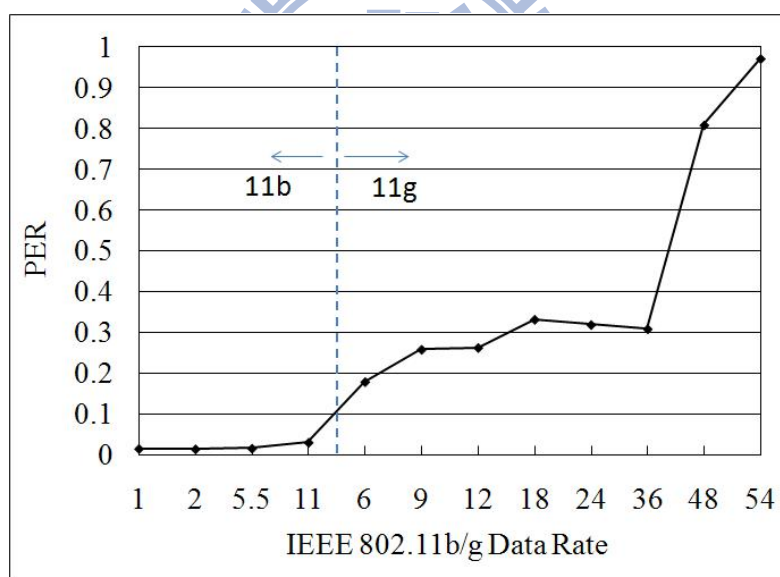
(a)
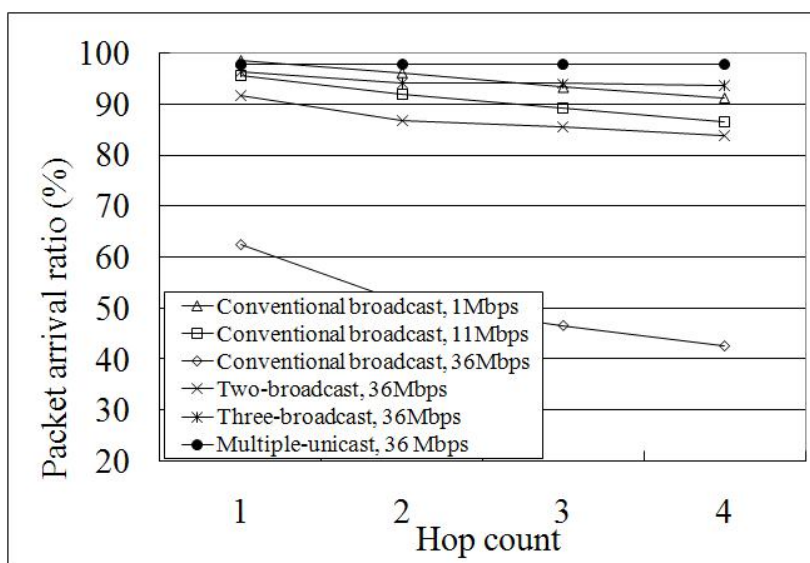
(b)

Figure 5-4: a) The relation between PER and data rate in our experimental deployment; b) packet arrival ratio for different broadcasting strategies in chain topologies.
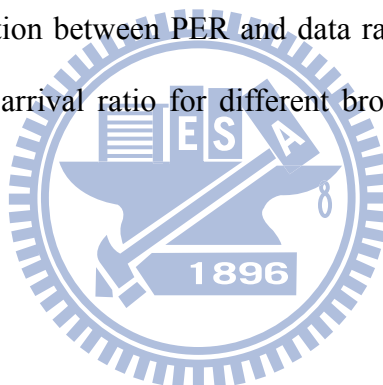
To determine the feasibility of these three schemes, this study investigates the routing construction success ratio in an n × n grid topology, as Fig. 5-5(a) shows. The routing construction is a typical function that uses mesh broadcast-type control frames in the IEEE 802.11s path selection framework. The success ratio is measured by counting successful routing trials, that is, when the source node (SRC) correctly receives a PREP from the destination node (DST). To reflect unicasting behavior in the real world, this study also measures the multiple-unicast scheme using the

134

RTL8186 auto-rate mode, automatic rate fallback (ARF) [88]. Figure 5-5(b) shows these experimental results. The success ratio of conventional broadcast with the most reliable data rate (i.e., 1 Mb/s) lowers to 86 percent in the largest experimental grid. However, the multiple-unicast scheme at 36 Mb/s keeps above 90 percent success ratio in all network sizes. Furthermore, the same scheme using the auto data rate is superior to all other schemes. Even in the 16-node grid, it shows a 98 percent success ratio for routing construction. Examining the distribution of auto data rates reveals that only 40 percent successfully received frames are delivered with 11g data rates (12~54 Mb/s), and 60 percent of the frames are sent at more reliable 11b data rates (1, 2, 5.5, and 11 Mb/s). In other words, the high reliability of using auto data rate comes from transmitting many frames with more robust modulations.

To investigate the side-effects caused by these schemes, this study measures latency and channel utilization during the experiments above. This study defines latency as the time interval starting when SRC issues a broadcast-type PREQ and ending when it receives the corresponding PREP. The experimental results in Fig. 5-5c indicate that the latency curves of all configurations are similar, with only small differences. Even for the largest grid, the slowest routing construction time (the multiple-unicast scheme using the auto data rate) is only 8 ms slower than the fastest time, the conventional broadcast at 11 Mb/s, at 40 ms. These results demonstrate that

an increased delay is acceptable for routing construction.

This study defines the channel utilization as the percentage of wireless media time occupied by all nodes on flooding the mesh broadcast-type control frames. This study investigates the root announcement messages, which are periodical mesh broadcast-type control frames maintaining a mesh routing tree, to assess the average channel utilization of mesh broadcast-type control frames in an IEEE 802.11s network. The total occupied media time includes the time spent on PHY layer headers, MAC layer headers, payload, and IFSs. Figure 5-5(d) depicts the calculated channel utilization. Due to the large proportion of low-speed 11b frames, the multiple-unicast scheme using auto data rate consumes more wireless resources than other configurations. However, since this is a small fraction (less than 3 percent), this overhead helps maintain the routing structure of a WLAN mesh. The results above reveal that the multiple-unicast scheme is the most suitable scheme for the transmission of mesh broadcast-type control messages in our testbed. In real-world deployment, however, the PER can change unpredictably, and a larger mesh scale may lead to unacceptable latency. Therefore, a sophisticated broadcasting strategy considering actual runtime conditions deserves further study.
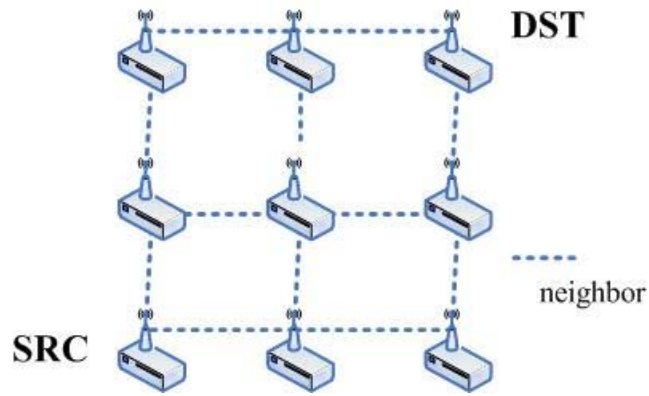
(a)
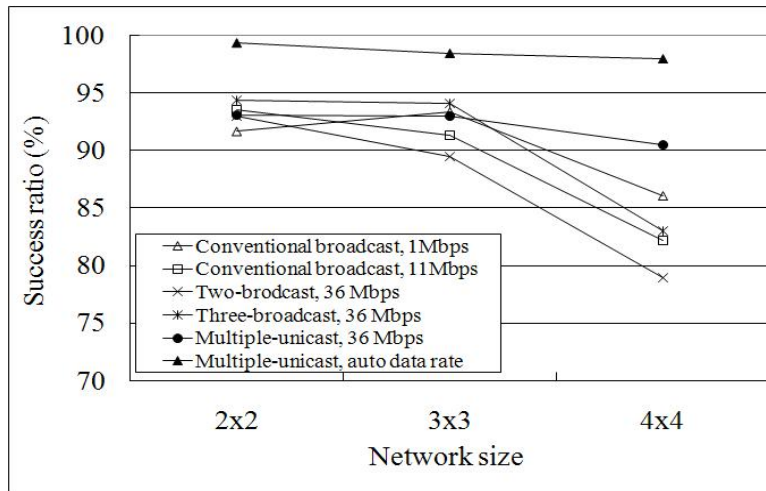
(b)
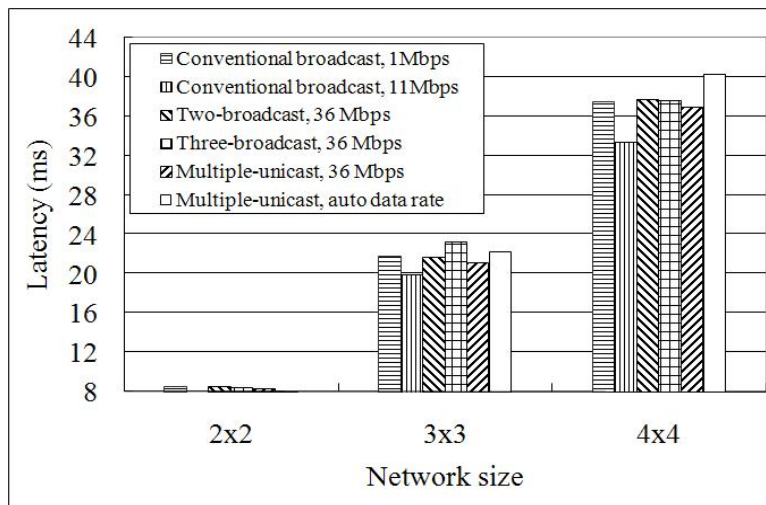
(c)
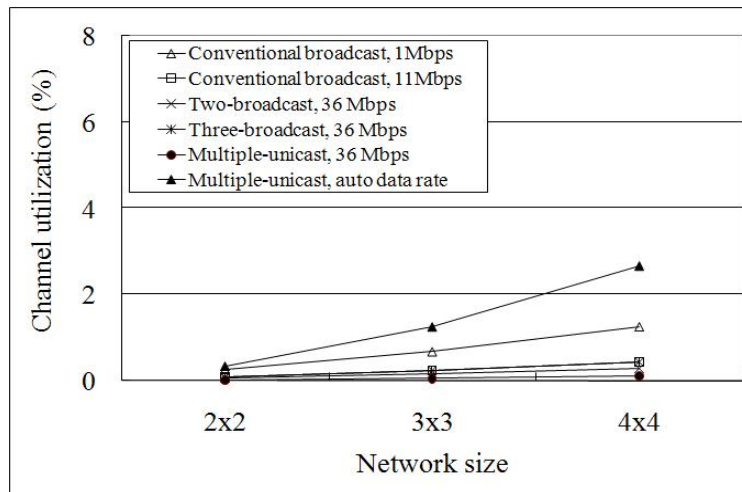
(d)

Figure 5-5: Experiments for routing establishment: a) the n × n grid topology; b) the success ratio, which is 98 percent when adopting the multiple-unicast scheme using auto data rate during 600 trials; c) the latency to establish a routing path; d) the channel utilization to maintain the routing tree.

5.6 Summary

This study presents the design and development of a WLAN mesh system conforming to the latest IEEE 802.11s draft amendment. Without costly hardware modifications, the proposed solution is a pure software extension for commercial off-the-shelf WLAN chipsets. This study constructs an experimental testbed, and evaluates issues

such as the transmission reliability of mesh broadcast-type control messages and multichannel transmissions. Experimental results demonstrate that the delivery of mesh broadcast-type control messages, such as routing construction frames, using the multiple acknowledged unicast scheme improves mesh stability from an 86 to a 98% success ratio in a grid topology with 16 nodes.

Chapter 6

Indoor Deployment of IEEE

802.11s Mesh Networks
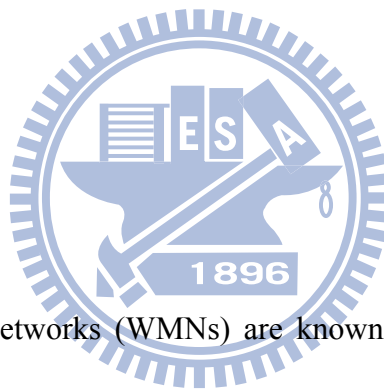
Emerging wireless mesh networks (WMNs) are known for their fast and low cost deployment. Many WMN testbeds have been developed for academic research purposes and commercial trials [8], [45]-[51]. There are generally two categories of testbeds built by previous work. The first category is implemented in a well-controlled laboratory environment, such as a shielding room. One of the most well-known lab testbeds is the ORBIT project [89]. The benefit of this category is that the strictly-controlled environment reduces the unexpected effect from external error sources, like the wireless signal generated by the widespread wireless devices and noise emitted by microwave ovens [90]-[91]. However, the disadvantage of this

approach is that the scale of experiments, constrained by time and laboratory space, is usually quite small. Therefore, the results from lab testbeds can indeed validate an idea under the clean environment, but are not general enough to be applied to all configurations in real-world deployment.

The second category of WMN testbed is the field trial. Most previous studies on this category build the testbed outdoors, e.g., in an urban or rural area. The devices used in an outdoor environment are usually commercial products [46], [47] and [51] because they must sustain harsh open-air conditions for extended periods of time. The advantage of this approach is that the results collected from a large-scale outdoor testbed are undoubtedly a good reference to real-world outdoor deployment. The disadvantage is that the results can vary greatly with highly changeable channel conditions and traffic loading. Meanwhile, the outdoor results might not be applicable to indoor, small-scale WMNs. Outdoor WMNs typically aim to provide last-mile or community wireless access, and hence need to deploy dozens to hundreds of STAs. To guarantee link capacity and signal quality, neighboring STAs should be within line-of-sight and equipped with directional antennas. Unlike outdoor WMNs, however, indoor WMNs provide wireless access coverage to a single building, especially important for old buildings without Internet facilities. The scale of an indoor WMN is much smaller, and its devices are much cheaper, e.g., plastic case without waterproof

consideration. In addition, signal decay is more serious in indoor WMNs due to non-line-of-sight deployment. Noise sources are also different from the ones in outdoor environment [91]. As a result, deployment guidelines obtained from outdoor testbeds could not be applied to indoor WMNs.

Indoor and outdoor WMNs possess distinguishable attributes and limitations. To the best of our knowledge, only a little previous work focuses on indoor WMNs [45]. Therefore, this chapter combines the deployment methodologies of laboratory and field testbeds to make observations and provide guidelines for indoor IEEE 802.11s WMN deployment. Specifically, 802.11s mesh entities of this study are implemented on a chipset complying with IEEE 802.11n [5]. First, we constructed a laboratory testbed. The experimental results of this testbed provide a basic benchmark for field deployment. Then, we deployed a testbed in a three-floor field environment, and conducted numerous experiments to investigate the effect of different configurations on complex channel conditions. Disagreeing with previous research, the results of this study indicate that RTS/CTS can improve throughput by up to 87.5%. Moreover, compared with the IEEE 802.11b/g, 802.11n achieves better fairness for multi-stream or multi-hop communications. Experimental results also suggest that a longer beacon interval, e.g. 500 ms, can improve channel efficiency for a denser deployment. On the other hand, sparser deployments should use a shorter beacon interval, e.g. 100 ms, to

enhance link stability.

The rest of this chapter is organized as follows. Section 6.1 reviews previous studies and summarizes the differences of key findings among those literals. Section 6.2 describes the IEEE 802.11s testbed and experiment methodology. Section 6.3 presents experiment results. Then, Section 6.4 summarizes the lessons and guidelines learned. Finally, Section 6.5 concludes the work.

6.1 Related Works: Effect of RTS/CTS and Rate Adaptation
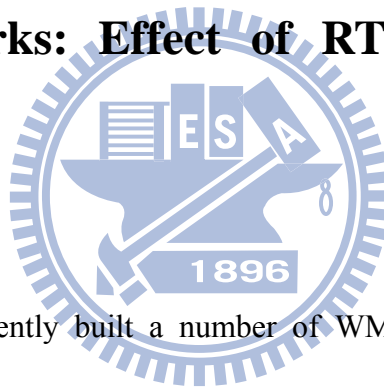
Researchers have recently built a number of WMN testbeds to evaluate the performance characteristics of WMNs in real environments. Koutsonikolas et al. [45] reported on the configurations of the TCP maximum window size and other two important MAC parameters, i.e., Request-to-Send/Clear-to-Send (RTS/CTS) and data rates, in the indoor WMN (named MAP) deployed at Purdue University. According to their observation, RTS/CTS and auto-rate adaptation (operating at 2 and 5.5 Mbps) should be enabled for 4-hop flows, and disabled for 1-hop and 2-hop flows. Sun et al. [47] also studied the impact of different MAC configurations of RTS/CTS and auto-rate adaptation (for 802.11b/g) on an indoor WMN testbed called UCSB

MeshNet. Their study focuses on performance evaluation in terms of latency and loss rate for video and voice traffic. They recommended that RTS/CTS should not be used for multimedia traffic, and that the auto-rate adaptation does not always lead to capacity improvement in bursty traffic.

In addition to studies on indoor WMN testbeds, several researchers have examined outdoor WMN testbeds. DGP [47] and FRACTEL [48] are 802.11b outdoor WMNs deployed to determine the performance of wireless networks in rural and semi-urban areas, respectively. Both of these studies indicate that external interference, generated by non-WiFi sources or from WiFi sources in adjacent channels, significantly increases the packet error rate of 802.11b long-distance links. As a result, [47] and [48] believed that RTS/CTS may not really help in such situations. Camp et al. [49] investigated a measurement study of an 802.11b outdoor WMN testbed (named TFA) and highlighted the importance of measurements in accurately planning mesh networks. They also demonstrated that the RTS/CTS scheme has an overall negative effect on per-node throughput with minimal gains in fairness, while a static rate limiting scheme yields a fair multi-hop throughput distribution even with heavily loaded traffic. In addition, Arjona et al. [46] evaluated the feasibility of singe-radio mesh technology and its competitiveness with cellular networks on an 802.11g outdoor WMN (called Google WiFi) for urban deployment built by Google. Like [49],

they concluded that rate limitations for each user could improve the fairness of multi-hop transmissions. Their study also shows that disabling the RTS/CTS scheme might improve overall performance at the expense of causing throughput fluctuation on nodes experiencing the hidden terminal problem [92].

Table 6-1 summarizes and compares the current measurement results with prior studies on WMN deployments. Our testbed is one of the few 802.11n indoor WMNs [93] based on 802.11s. This study offers three major findings: (a) a performance comparison between 802.11n and 802.11g under multi-flow and multi-hop transmissions; (b) an analysis of the impact of beacon interval on the connectivity and throughput of the WMN testbed; and (c) the finding that RTS/CTS can increase the throughput and that the auto-rate adaptation is good for indoor deployment. The last finding does not completely agree with the observations of previous studies, which may come from different test environments and configurations. In [45], the operating data rates, i.e., 2 and 5.5 Mbps, are robust when comparing to other data rates of 802.11b/g/n. In this case, the RTS/CTS mechanism might be less helpful in transmission protection. Also, their suggestions for the using of auto-rate adaptation scheme are not representative of 802.11b/g/n systems, because the rates they used are only a small subset of 802.11b/g/n rates. Another study [47] focused on the latency and loss rate for multimedia transmissions, while the current study examines

throughput. Other studies [47], [48], [49] and [50] deal with outdoor testbeds where the deployment density is sparse, so the benefit of using RTS/CTS to reduce collision is less than its overhead. Moreover, due to line-of-sight deployment, the operating data rates of outdoor WMNs could be predictable according to long-term channel conditions.

Table 6-1: Summary and Comparison on the Previous Work

	HW/SW Tech.		Configuration recommendation		
	Platform	802.11 PHY	Beacon interval	RTS/ CTS	Auto rate
Our work (indoor)	Realtek AP + Linux	802.11b/ g/n	○	◎	◎
MAP [45] (indoor)	PC + Linux	802.11b	–	○	○
UCSB [46] (indoor)	Linksys AP + OpenWrt	802.11b/g	–	×	○
DGP [47] (rural)	Soekris + Linux	802.11b	–	△	–
FRACTEL [48] (semi-urban)	Laptop + Linux	802.11b	–	△	–
TFA [49] (urban)	PC + Linux	802.11b	–	○	×
Google WiFi [50] (urban)	Tropos device	802.11 g	–	○	×

◎: Suggested, ○: Case dependent, △: Not necessary (helpless), ×: Not suggested, –: No study.

146

6.2 IEEE 802.11s Testbed

6.2.1 Experiment Configuration

This subsection describes the environment and topology of the experiment. Based on the Realtek RTL8192SE + RTL8196B platofrm, the testbed used the WLAN mesh system mentioned in previous chapter for all STAs, MAPs, and MPPs. A two-phase deployment plan is used to establish the benchmark of the 802.11s testbed. In the first phase, the testbed was deployed in a laboratory to evaluate its basic capacity and performance for a dense deployment. Fig. 6-1(a) shows the two chain topologies with 5 MAPs in the laboratory environment, in which MAPs are placed 50 cm apart and 9 MAPs used to construct a 3-by-3 grid topology, where each grid edge is also 50 cm. Although the placement the MAPs is, the laboratory experiments could not only provide results under a controllable environment comparing with the large-scale experiments. But the results could also suggest the possible lessons for indoor WMNs. This configuration can be taken as the sample topology of the field deployment. These experiment results provide benchmarks and configuration suggestions for the field experiment. In the second phase, a 9-node, 3-by-3 grid WMN was deployed in the sixth to eighth floors of the Microelectronics and Information Systems Research

Center (MIRC) at National Chiao Tung University. Three MAPs were deployed on each floor, as Fig. 6-1(b) shows. The distance between MAPs was approximately 25 m. The resulting mesh network covered three floors of the MIRC building. Besides the experimental deployment, four access points standing by on the same channel were detected on the three floors during trials. Figs. 6-2(a) and 6-2(b) show pictures taken from the laboratory and field, respectively. We adopted the access control list (ACL) to disable undesired mesh links in the experiments. For example, mesh links are disallowed in the grid topology if two MAPs are neither horizontally nor vertically adjacent. Note that an allowable mesh link does not imply a connected link. Section 4 examines the issue of link stability. We did not use an attenuator in our experiments because the 802.11n MIMO is too sensitive to be precisely controlled with attenuators in a small laboratory space. It is also impractical to attach an attenuator to a MAP in real-world deployment.
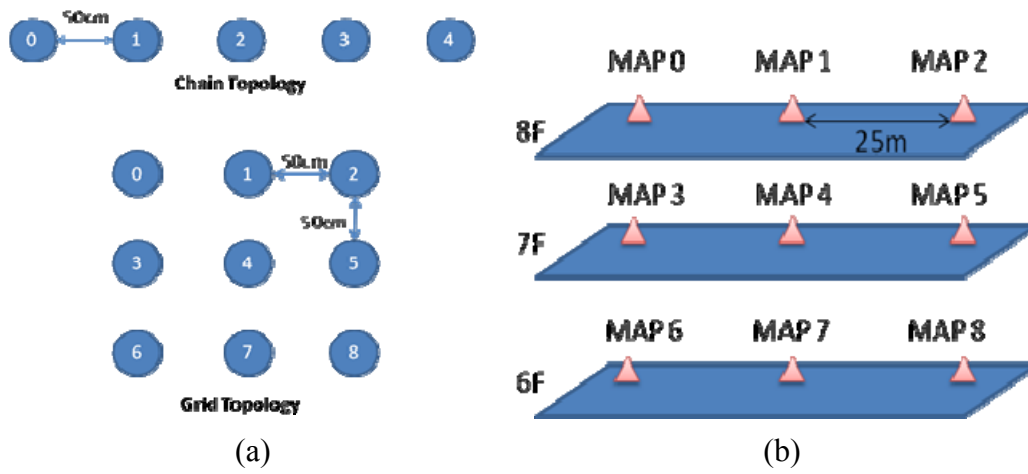
Figure 6-1: Topologies of the testbed in laboratory and field.

(a)
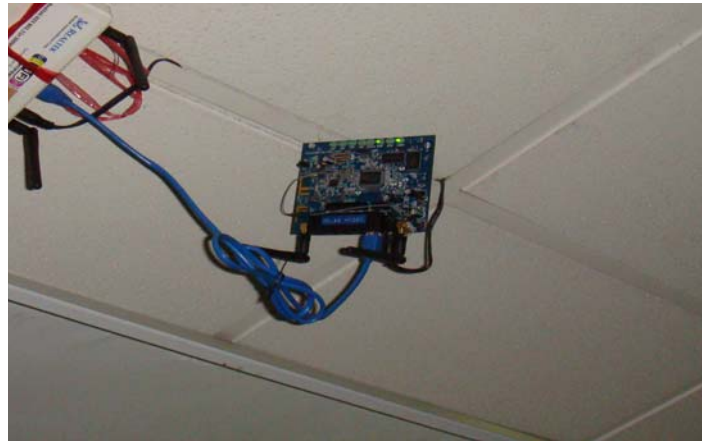
(b)

Figure 6-2. Pictures of the testbed in laboratory and field.

6.2.2 Experiment Methodology

For convenience, each MAP was equipped with the Simple Network Management

Protocol daemon (SNMPd). This makes it possible to remotely control the embedded

Linux on the STAs through the SNMP. Fig. 6-2(b) shows that a data collecting node

connects the MAP via the wire-line. Therefore, statistics can be collected directly by a

wired connection without interfering with the test traffic.

We used Netperf [94] to measure the TCP stream performance for the MAPs.

Each experiment was repeated more than five times to obtain the average results.

Because the duration of each run dominates the convergence of the results, most of

the experiments run for more than 1 h to collect enough data and satisfy the convergence. This study defines the traffic stream transmitted from the MPP to the MAPs as the downlink traffic. On the other hand, the traffic stream from MAPs to the MPP is the uplink traffic. In a single-stream experiment, only one TCP stream is transmitted at a time. In a multi-stream experiment, which demonstrates a multi-user environment, four MAPs transmit simultaneously. Because of channel quality and data rate generated by Netperf, our field experiments can barely support more than four simultaneous Netperf streams.

6.3   Experimental Results
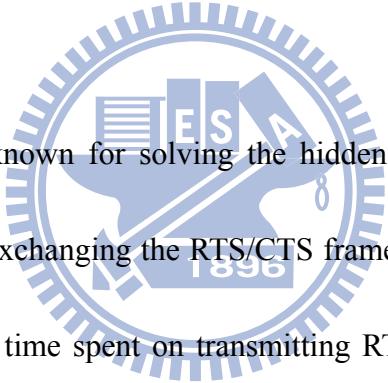
This section presents the most representative results for both laboratory and field deployments with respect to the configurations of RTS/CTS, 802.11 PHY, and beacon interval. Unlike previous deployment studies, this study examines network configuration guidelines for indoor mesh networks. Table 6-2 describes the default configurations of the testbed. Unless otherwise specified, the experiments in the following subsections follow these default configurations.

Table 6-2: Default Testbed Configurations

Parameter	Setting
PHY	IEEE 802.11n
Data rate	Auto
RTS/CTS	Off
Beacon interval	Lab: 500 ms; field: 200 ms
Basic rate	1 Mbps
Link expire timer	15 s
Access control	Allow adjacent nodes only

6.3.1 RTS/CTS

The RTS/CTS scheme is known for solving the hidden terminal problem in IEEE 802.11 WLAN. However, exchanging the RTS/CTS frames causes additional channel access overhead, including time spent on transmitting RTS/CTS with the basic data rate, i.e. 1 Mbps, regulated by the IEEE 802.11 standard, and certain inter-frame spaces (IFSs). This subsection discusses how RTS/CTS affect TCP performance in the laboratory and the field.

Fig. 6-3 illustrates the single-stream performance of both laboratory and field experiments. This figure can be viewed as the throughput benchmark for our testbed. The one-hop throughput of an 802.11n-based WMN without RTS/CTS is 22.95 Mbps. The TCP performance decreases as the hop count increases. The field results of all

cases in Fig. 6-3 are approximately 40% of the laboratory throughput values when the RTS/CTS scheme is not activated. If the scheme is activated, the field results are approximately 60% of the laboratory results.

When the RTS/CTS scheme is turned on in the laboratory experiments, Fig. 6-3 shows a decrease in TCP performance, comparing with the results of no RTS/CTS scheme. In the field experiments, however, activating RTS/CTS slightly improved the throughput. This is because all the MAPs in the laboratory experiment are located in the same collision domain. Since there is no hidden terminal problem, the RTS and CTS messages become additional overhead that frequently occupies the channel. However, when the testbed is deployed in the field, the transmission distance is not only longer, but the channel condition is also more complicated. Therefore, RTS/CTS help protect the transmissions from the hidden terminals in field trials, achieving a higher throughput.

Figs. 6-4(c) and. 6-4(d) depict the TCP performance of downlink multi-stream experiments in the field testing. In Fig. 6-4(c), the MAP2 of Fig. 6-3(b) is configured as a MPP that simultaneously transmits four TCP streams. Two of these streams are one-hop streams, while the other two traverse three hops. Note that different routing paths of the three-hop streams would result in different performance; however, to examine the real-world WMN properties, we did not put any constraint on the routing

decision. Thus, the actual paths were decided in the run-time. In the experiments for

Fig. 6-4(d), MAP4 is configured as a MPP, and therefore, all four TCP streams only

traverse one-hop. The results in Fig. 6-4(c) and 6-4(d) match the observation from Fig.

6-4(a) that RTS/CTS alleviate the hidden terminal problem and increase the TCP

throughput. Moreover, the improvement in Fig. 6-4(d) becomes more obvious, i.e.,

about 33.5% for 802.11n and 87.5% for 802.11b/g, when comparing the results in Fig.

6-3 and Fig. 6-5. This improvement may arise from the broader RTS/CTS effective

area, as the RTS/CTS initiator (the traffic source) is at the center of our deployed

floors. Fig. 6-6 shows that the throughput of the cross-floor link seems better than the

links at the same floor. This is because the distance between the cross-floor MAPs is

shorter than the neighboring MAPs at the same floor.

To summarize, the RTS/CTS scheme is recommended for indoor deployment and

higher throughput can be achieved when the RTS/CTS signal covers more

interference sources. If a WMN is deployed in the same collision domain, however,

RTS/CTS are not necessary.
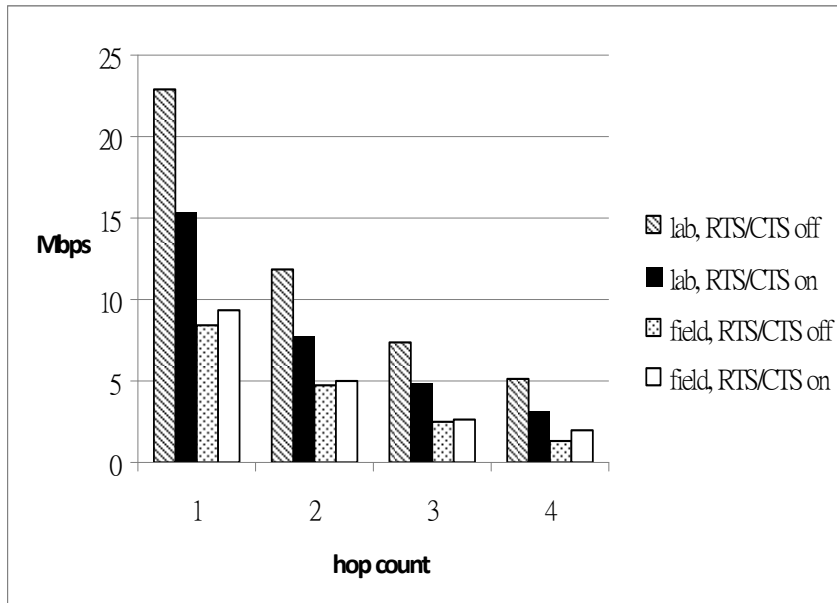
Figure 6-3: Comparison of TCP throughputs between laboratory and field experiments. Effects of enabling RTS/CTS (single-stream, chain topology).
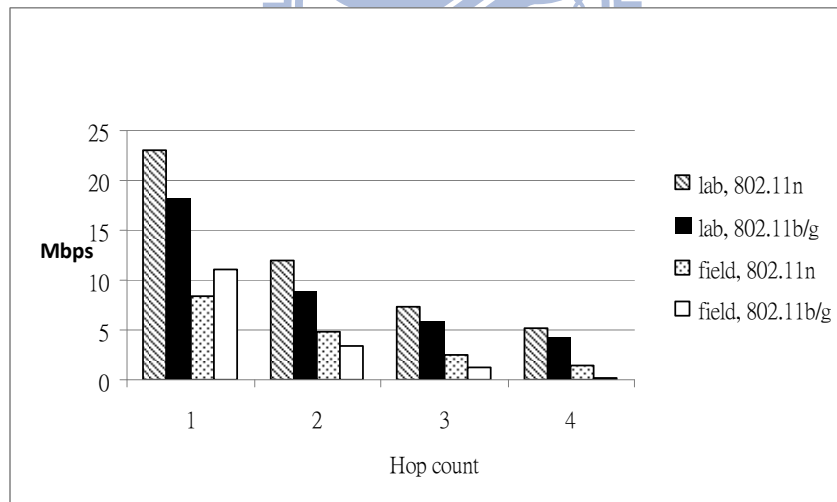
Figure 6-4: Comparison of TCP throughputs between laboratory and field experiments. Comparison of IEEE 802.11b/g/n rates (single-stream, chain topology).

Figure 6-5: Comparison of TCP throughputs between laboratory and field experiments. Effects of setting MPP's location at corner in the field (downlink multistream,grid topology).

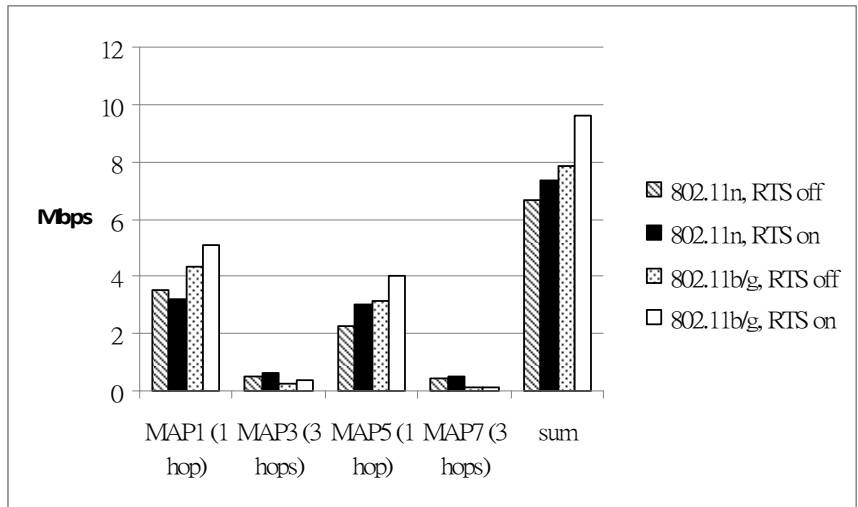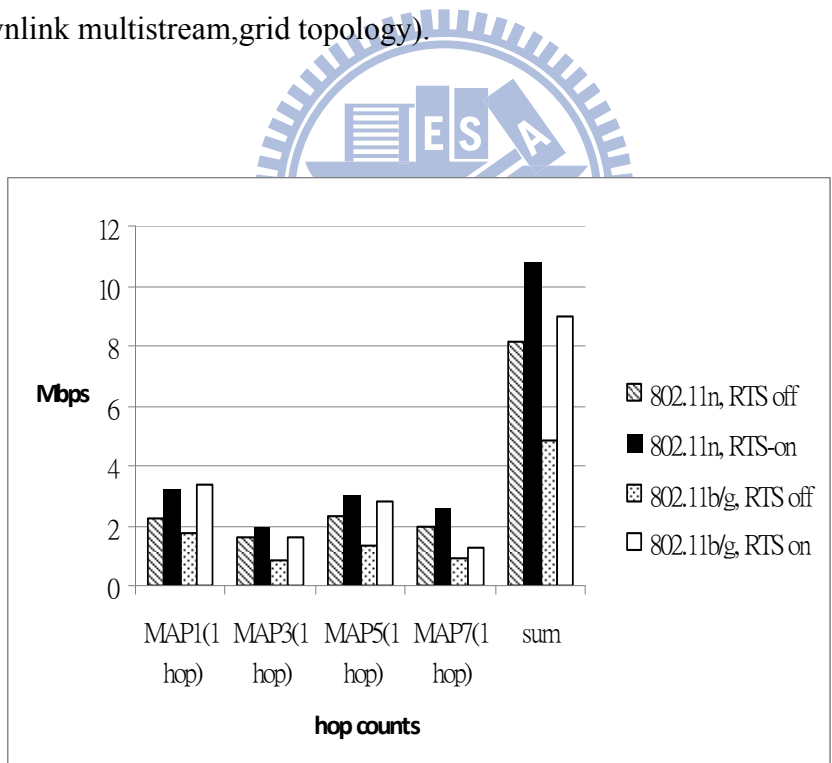Figure 6-6: Comparison of TCP throughputs between laboratory and field experiments. Effects of setting MPP's location at center in the field (downlink multistream, grid topology).

6.3.2 IEEE 802.11n vs. 802.11b/g

As mentioned in Section 6.1, most related studies examine 802.11b/g WMNs. The 802.11n standard, however, adopts different technologies that utilize a MIMO design to support higher data rates. This subsection examines the characteristics of an 802.11n-based WMN.

Fig. 6-4 compares the single-stream TCP throughput of 802.11n and 802.11b/g from 1-hop to 4-hop in both laboratory and field environments. Laboratory results show that the 802.11n outperforms 802.11b/g by 25% at all hop counts. This is reasonable because 802.11n can transmit data at higher rates than 802.11b/g. However, the results in the field experiments are not consistent at the first-hop. In Fig. 6-4 and Fig. 6-5, the performance of 802.11b/g surpasses the 802.11n for the one-hop transmissions, while these results are reversed in Fig. 6-6. We verified this inconsistency by conducting the same experiments several times, finally concluding that this fluctuation comes from the 802.11n PHY sensitivity to channel conditions and antenna position. Although 802.11n frames can be transmitted at a higher data rate, these high-data-rate frames are more likely to be dropped due to the need for

better received signal quality for successful demodulation. Therefore, channel quality fluctuations in the field leads to variations in 802.11n performance.

The phenomenon in which a channel is constantly occupied by some users is called the channel capture effect [46]. Fig. 6-7 presents the multi-stream TCP performance in a chain topology to demonstrate the channel capture effect. In this figure, the amount of data originating from the first-hop MAP in 802.11b/g is similar to that in 802.11n, i.e., the throughput ratio of 802.11b/g to 802.11n is 0.98. However, the throughput difference between 802.11b/g and 802.11n does not increase linearly as the hop count increases, i.e., the ratios for 2, 3 and 4 hops are 0.32, 0.48 and 0.65, respectively. The reason should be the channel resource used by 802.11b/g to deliver the same amount of data is higher than that in 802.11n because 802.11b/g has slower data rates. Thus, in 802.11b/g, most channel resources are spent on one-hop transmissions, and there are few remaining resources for the other hops, as Fig. 6-7 shows. In other words, the channel capture effect is more serious in 802.11b/g, and produces more unfairness in the TCP throughput.

To summarize, 802.11n does not necessarily outperform 802.11b/g because of the critical requirement of received signal quality for high data rates. However, multi-hop transmissions can take advantage of the higher data rates of 802.11n. 802.11b/g suffers from the channel capture effect, which causes significant unfairness in the

WMN. Therefore, 802.11n is still the preferred standard for an indoor WMN.
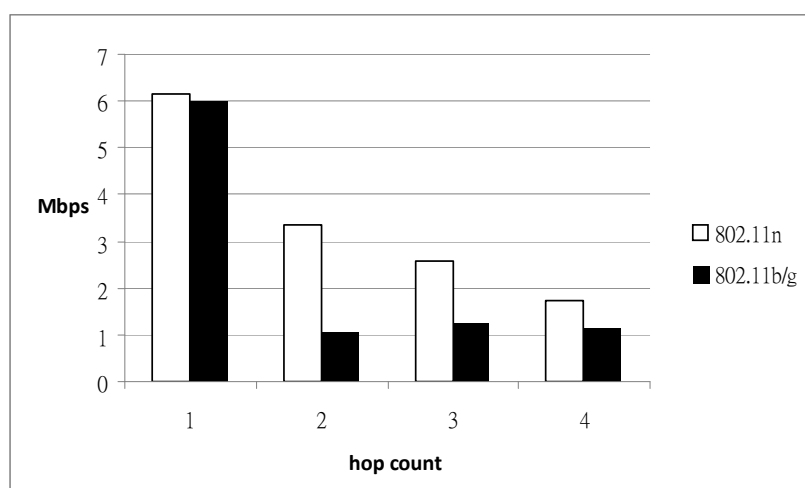
Figure 6-7: Comparison of TCP throughputs between laboratory and field experiments. Channel capture effect of IEEE 802.11b/g rates in the field (uplink multistream, chain topology).

6.3.3 Beacon Interval

As mentioned in Subsection 6.2.1, the STAs in the proposed testbed relied on received beacons to maintain links with their neighbors. In this setup, a link is deleted if no beacon is received from the neighbor for 15 s. Therefore, the periodical beacon announcement is still necessary. However, just like other IEEE 802.11 control frames, a beacon frame is transmitted at the basic data rate, i.e. 1 Mbps, and therefore

consumes a lot of channel resources. We use an extreme example to demonstrate how beacons can impact channel utilization in a WMN. Assuming that the beacon size is 250 bytes, broadcasting a beacon will occupy approximately 250 × 8 (bits)/106 (1 Mbps) = 2 ms of the channel. If the beacon interval is 100 ms and there are more than 50 MSTAs within the same collision domain, the channel could be fully occupied by beacons, i.e., 2 ms × 10 (beacons/s) × 50 (MSTAs) = 1 s. At the same time, many beacons would be lost with additional traffic competing for the channel. This study set MAP4, which is located at the center of the WMN, as the MPP, and performed multi-stream experiments in both laboratory and field environments. All of the four streams are one-hop. Fig. 6-8 shows the aggregated TCP throughput under different beacon interval settings. When the beacon interval increased to 500 ms in the laboratory experiment, there was significant improvement of 43% in uplink TCP throughput. In the field experiment, the same beacon interval increase caused 22% and 25% improvement in downlink and uplink throughput, respectively. This is because a beacon is transmitted at 1 Mbps, occupying a lot of channel access time. Prolonging the beacon interval allows more data traffic to access the channel, enhancing channel utilization. However, the downlink throughput in the laboratory experiment only improved slightly when the beacon was set to 500 ms. We think this may come from the computation limitations of the test platform to simultaneously

generate TCP data and route packets in both IP and data-link layers to four destinations.

Although Fig. 6-8 shows that increasing the beacon interval can significantly improve the throughput in laboratory and field environments, this change also affects link stability. As mentioned before, a mesh link is deleted when the MSTA does not receive a beacon from a specific neighbor for a predefined period of time, e.g. 15 s in our testbed. To illustrate how the beacon interval impacts link stability in a WMN, we counted the number of link state changes at each link. The rate of link state change can then be derived by dividing the number of link state changes by the experiment time. We recorded the link state of the WMN every 10 s for 1 h in the field experiment. Results show that the link state change rates are 0.059, 0.083, and 0.13 for beacon intervals of 100 ms, 500 ms, and 1000 ms, respectively. The link state change rates of 500 ms and 1000 ms are significantly increased. When the beacon interval was 1000 ms, we could not proceed with the field experiments because the link failed frequently. This is also the reason why we only present the TCP results of 100 ms and 500 ms.

To summarize, a longer beacon interval keeps mesh links stable in a small and dense deployment, while the link state becomes changeable in a large and sparse deployment, especially when the channel is not clean. Therefore, in a dense

deployment, the beacon interval could be set to a longer value, e.g. 500 ms, to

consume less channel resource for mesh control plane and reserve the resource for

mesh data plane. However, to maintain the link stability, a shorter beacon interval, e.g.,

100 ms, is recommended in a large and sparse deployment.
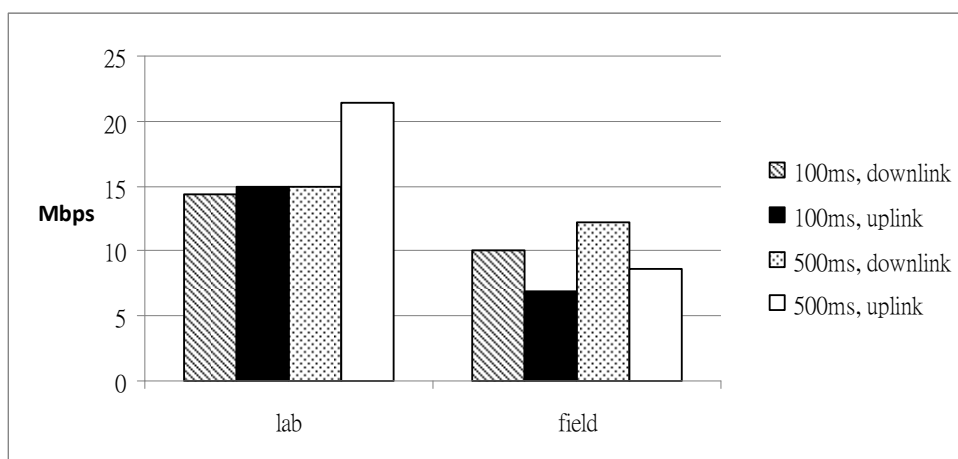

Figure 6-8: Comparison of TCP throughputs between laboratory and field

experiments. Comparison of the total throughput when setting MPP at center

in field (multi-stream, grid topology).

6.4 Lessons and Guidelines

This section summarizes the lessons learned from the experiments, including those

that are not described in Section 6.3, and provides guidelines for indoor mesh

deployment. The suggestions are itemized as follows:

1.Activate RTS/CTS in the indoor deployment

Unlike the conclusion of [46], [47] and [48], this study shows that RTS/CTS should be activated in indoor field deployment, especially when there are many interference sources and the STAs are not in the same collision domain. Nevertheless, if the WMN is deployed in the same collision domain, the RTS/CTS scheme is still not recommended as suggested in [46]. Based on our observation, RTS/CTS can effectively resolve the hidden node problem. Studies in [47] and [48] focus on long-ranged outdoor WMNs, the signal is highly interfered by the non-WiFi interference sources. Therefore, RTS/CTS cannot alleviate the interference.

2.802.11n is duggested for multi-flow, multi-hop

Although 802.11b/g performs no worse than 802.11n in one-hop transmissions in the field, the low-rate 802.11b/g frames occupy more channel resources for each hop. The first-hop node in an 802.11b/g chain topology generates almost 70% of the total throughput, producing a serious channel capture effect. Therefore, starvation may occur at STAs with a large hop count in an 802.11b/g WMN. Thus, 802.11n is still preferred for WMN deployment.

3.Beacon interval matters

The beacon interval can affect the frequency of updating the link state. However, transmitting beacons with 1 Mbps consumes much of the channel. It is a tradeoff between the link stability and the maximum throughput. We recommend setting the beacon interval at a longer value, e.g. 500 ms, in a small and dense deployment. A smaller beacon interval of 100 ms is preferred for a large and sparse deployment, especially when the channel condition is not good. This is because the link stability is also critical for the WMNs. If the link is unstable, it is possible that the MAP cannot link to any other MAPs or packets drop frequently due to link loss.
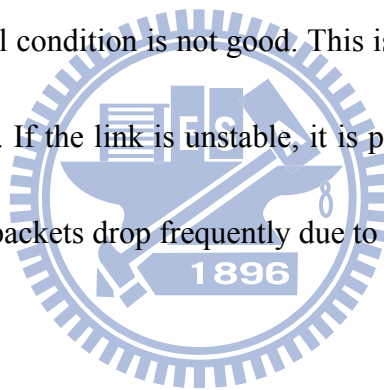
4.Fixed rate Does not help

The results from two studies on outdoor testbeds [49] and [50] imply that a fixed rate should be used to achieve better throughput. However, the channel quality in our indoor field experiments is much more variable than their outdoor, line-of-sight communication. An aggressive fixed rate might destabilize the transmissions, while a conservative fixed rate produces a poor throughput. An auto data rate mechanism allows the transmission rate to be adjusted dynamically according to the channel quality, but this adjustment mechanism must be sensitive enough to adapt to the

fluctuant channel conditions in the field.

5.Bottleneck is the channel condition

Results show that the total throughput of a multi-stream experiment is close to the single-stream, one-hop throughput. The throughput bottleneck seems to be the MSTA, and especially the MPP, where traffic streams aggregate. This result matches the findings of previous research [95]. Therefore, the MPP should be located in a position with a clear channel condition, leading to better link quality between the MPP and its neighboring STAs.
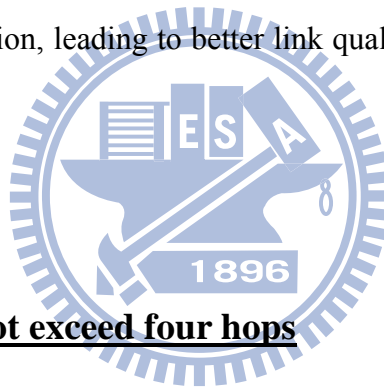
6.Hop-count should not exceed four hops

Considering the performance and the stability for the end-to-end traffic, we recommend that the hop-count should not exceed four hops.

7.Mesh size is determined by MPP's capacity and maximum hop count

Based on the item 5 and 6, the throughput performance of a WMN is highly related to the channel quality of the MPP and the hop count of the traffic flow. Therefore, the size of a WMN is determined by the MPP's capacity and maximum hop count.

8. Cross-floor links are frangible

Results show that the signal of a cross-floor link is quite unstable. Thus, the cross-floor links should be avoided.

9. Angle and direction of antenna pairs are critical

IEEE 802.11n adopts the MIMO technique to achieve higher data rates. Similar to previous findings [96], angle and direction of the antennas of the MAPs in our experiments directly affected the measured received signal strength (RSS). Because RSS is one of the criteria of data rate adjustment, antennas placement is a critical factor in networking performance.
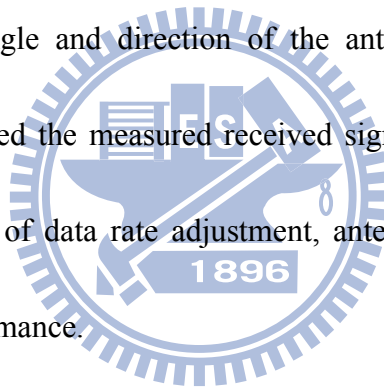
10. Avoid links with asymmetric RSS values

By changing the antenna placement, the RSS values seen by the peers in a link may have huge difference. RSS could be a factor in WMN routing metrics. If the RSS measured by the peers is asymmetric, the routing path may not be symmetric, e.g., there is another MSTA with a better RSS value measured by only one end of the peers. Previous research [97] indicates that asymmetric routing could lead to serious problems for Ad hoc On-Demand Distance Vector Routing (AODV) [98], from which

the 802.11s routing protocol is derived. Therefore, the links with asymmetric RSS values may cause asymmetric routing problems.

6.5 Summary

This study develops and evaluates an IEEE 802.11s wireless mesh network testbed for indoor environments. Based on observations, this study provides guidelines for tuning various parameters in indoor WMNs. Extensive experiments are conducted in both laboratory and field environments. Unlike previous studies, the experiment results of this study recommend activating RTS/CTS if the mesh nodes do not coexist in the same collision domain. Results also show that the 802.11b/g PHY performs no worse than 802.11n with respect to one-hop transmissions. However, 802.11b/g can cause serious unfairness because one-hop nodes constantly occupy the channel. Besides, the beacon interval should be set to a longer value, e.g., 500 ms, in a dense deployment, and set to a smaller value, e.g. 100 ms, to enhance link stability in a sparse deployment. Finally, the observations summarized in this article can provide guidance for small or medium scale indoor 802.11 WMNs.

Chapter 7
Conclusion

Based on applications of the IEEE 802.11 WLAN standards, this dissertation

addresses the designs of a compact MIMO-OFDM modem and an IEEE 802.11-based

WMN by two parts (Part I and Part II, respectively).
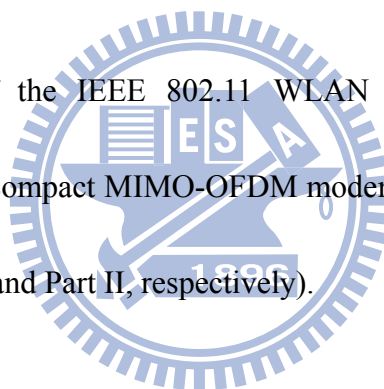
7.1 Summary

For the design of a compact MIMO-OFDM modem, a FD receiver adopted the

FD-ADC technology is proposed to support both of SC and OFDM modes over the

frequency domain. In order to realize this FD receiver, two key modules are essential

to built. The first one is the FD symbol synchronizer which needs to find the symbol

boundary with the frequency domain signal vectors generated by FD ADC. The FD

symbol synchronizer is designed with a symbol-rate sequential search algorithm and

implemented by TSMC 65-nm silicon technology. In comparisons with other existing literatures, this FD symbol synchronizer shows almost the best performance at low SNR range (i.e. 0≤SNR≤10) and the lowest implementation cost in terms of (normalized) area, cell and gate count. The main cost of the proposed synchronizer is to require one additional preamble. The second key module is the SC-FDE which needs to handles the channel estimation and data equalization/decoding in the frequency domain which receiving IEEE 802.11b (SCBT) data packets. Compared to the other approaches, the proposed SC-FDE only requires single-FFT architecture and provides good performance by ML detection. Moreover, the ML detection can adopt the sphere decoding algorithm to reduce the search complexity. The features of single-FFT architecture and SD implementation make the proposed SC-FDE integrate with the MIMO-OFDM modem efficiently. The third key module is the MIMO detection used in MIMO-OFDM modem. A pre-pruning scheme is proposed to reduce the search space of K-best algorithm. Using ZF detection result, the pre-pruning scheme performs a cluster-based search in the multilevel structure of N_q-QAM constellation to find the reliable constellation points. Compared to the conventional K-best algorithm with the same K value, the proposed pre-pruning scheme achieves the same performance with fewer search nodes. The scheme provides a further complexity reduction way not only for a low complexity K-best algorithm but also for

the receiver equipping with both K-best and ZF detectors.

For the IEEE 802.11-based WMN, complete system phases from design, implementation, and deployment are investigated in the part II of this dissertation. The WMN is developed based on the D2.03 of IEEE 802.11s and the related mesh functions of IEEE 802.11s software package are integrated to the commercial off-the-shelf WLAN chipsets. To improve the portability of the IEEE 802.11s software package, a modularized design is proposed to separate platform-independent functions (i.e. HWMP routing function) from the kernel and implement them as a Linux daemon program. To improve the transmission reliability of broadcast-type control frames, several broadcasting strategies are evaluated with a testbed in the laboratory. Experimental results show that the multiple-unicast scheme can provide the best balance between routing construction ratio, acceptable latency, and channel utilization. Then, a deployment testbed with 3-by-3 grid topology is constructed in both laboratory and field crossing three floors of the building. Disagreeing with previous research, the results of this study indicate that RTS/CTS can improve throughput by up to 87.5%. Moreover, compared with the IEEE 802.11b/g, 802.11n achieves better fairness for multi-stream or multi-hop communications. Experimental results also suggest that a longer beacon interval, e.g. 500 ms, can improve channel efficiency for a denser deployment. On the other hand, sparser deployments should

use a shorter beacon interval, e.g. 100 ms, to enhance link stability. Finally, the observations summarized in Chap 7 can provide guidance for small or medium scale indoor 802.11 WMNs.

7.2 Future Work

At the end of this dissertation, several analyses are suggested to be further study to make current research results become more complete and stronger. The first one is the analysis of VLSI architecture of FD symbol synchronizer. Since the proposed architecture uses higher clock speed to achieve more hardware sharing, the tradeoff between silicon area and power consumption should be further analyzed. The second one is the computation complexity of the proposed pre-pruning K-best scheme can be analyzed deeply and compared with other advance K-best algorithms. To extend the related research topics, a number of open issues are also summarized as follows:

1. For the evolution of IEEE 802.11 WLAN standards, the next generation WLAN communication systems are defined in the amendments of IEEE 802.11ac and IEEE 802.11ad. IEEE 802.11ac can be viewed as the BW extension version from IEEE 802.11n. Therefore, most IEEE 802.11n receiver modules can still be reused with slight modifications to the IEEE 802.11ac receiver architecture. However, IEEE 802.11ad enables the multi-Gbps Wi-Fi via a new 60G PHY. The longer

preamble length (i.e. Golay codes) and symbol block size (i.e. Reed Solomon code in SC mode) significantly increase the complexity of the proposed frequency-domain synchronization and equalization. Moreover, high sampling rate also leads critical VLSI implementations. To realize the FD receiver in IEEE 802.11ad will be therefore a very challenge topic in the future research efforts.

2. In this dissertation, we design a single-channel WMNs. The robustness of routing protocol is what we consider firstly. Therefore, the broadcasting strategies for broadcast-type control frames are evaluated. However, the co-channel interference avoidance is another important issue which significantly degrades the network capacity. The multi-channel WMNs may suppress the effect of co-channel interference, but it introduces the adjacent channel interference and makes protocol complex. Recently, the MIMO spatial multiplexing scheme has been applied to reduce the con-channel interference. Moreover, the new coming standard, IEEE 802.11ac, invites the scheme of multi-user (MU)-MIMO, which allows multiple receivers transfer data to single transmitter in up-link way or single transmitter transfers data to multiple receivers in down-link way. This scheme can significantly reduce the co-channel interference and increase the system capacity in single-channel WMN. Therefore, the integration of MU-MIMO scheme into our WMN becomes an emergent and meaningful topic. It also needs

to highlight that this topic includes interference mulling, MU-MIMO scheduling and fairness problem, which should be designed with cross-layer over physical, media access control (MAC), and even application layers.

3. Mobile communication systems have also evolved rapidly in the last decade. The 3rd Generation Partnership Project (3GPP) has submitted the Long Term Evolution-Advance (LTE-A) to International Telecommunication Union Telecommunication Standardization Sector (ITU-T) as a candidate 4G system in late 2009. One of the new concept in LTE-A is the coordinated multipoint (CoMP) transmission, which enables Multiple base stations cooperate to determine the scheduling, transmission parameters, and transmit antenna weights for a particular user equipment. Unlike the conventional synchronization algorithm focus on point-to-point transmission, the synchronization in CoMP becomes an interesting topic since the received data may come form multiple cooperative stations.

Reference

[1] *IEEE Standard for Wireless LAN Medium Access Control (MAC) and Physical Layer (PHY) Specifications, Nov. 1997. P802.11.*

[2] *Wireless LAN Medium Access Control (MAC) and Physical Layer (PHY) Specifications, IEEE Std 802.11b, 1999.*

[3] *Wireless LAN Medium Access Control (MAC) and Physical Layer (PHY) Specifications, IEEE Std 802.11a, 1999.*

[4] *Wireless LAN Medium Access Control (MAC) and Physical Layer (PHY) Specifications, IEEE Std 802.11g, 2003.*

[5] *Wireless LAN Medium Access Control (MAC) and Physical Layer (PHY) specifications: Enhancements for Higher Throughput, IEEE Std 802.11n, 2009.*

[6] D. Falconer, and S. L. Ariyavisitakul, A. Benyamin-Seeyar, and B. Eidson, "Frequency domain equalization for single-carrier broadband wireless systems," *IEEE Commun. Mag.*, vol. 40, pp. 58-66, Apr. 2002.

[7] Z. Wang, X. Ma, and G. B. Giannakis, "OFDM or single-carrier block transmissions?," *IEEE Trans. Commun.*, vol. 52, pp. 380-394, March 2004.

[8] I. F. Akyildiz, X. Wang, and W. Wang, "Wireless Mesh Networks: A Survey," *Comp. Net.*, vol. 47, no. 4, 2005, pp. 445–87.

[9] R. Bruno, M. Conti, and E. Gregori, "Mesh Networks: Commodity Multihop Ad Hoc Networks," *IEEE Commun. Mag.*, vol. 43, no. 3, Mar. 2005, pp. 123–31.

[10] Y-D. Lin and Y-C. Hsu, "Multihop Cellular: A New Architecture for Wireless Communications," in *Proc. IEEE INFOCOM*, vol.3, no., pp.1273-1282 vol.3, 26-30 Mar 2000.

[11] J. Bicket et al., "Architecture and Evaluation of an Unplanned 802.11b Mesh Network," in *Proc. ACM Mobi-Com*, 2005.

[12] A. Raniwala and T. Chiueh, "Architecture and Algorithms for an IEEE 802.11-based Multi-Channel Wireless Mesh Network," in *Proc. IEEE INFOCOM*, vol.3, no., pp. 2223- 2234 vol. 3, 13-17 March 2005.

[13] K. Ramachandran et al., "On the Design and Implementation of Infrastructure Mesh Networks," in *Proc. IEEE Wksp. Wireless Mesh Net.*, 2005.

[14] *IEEE P802.11s/D2.03, "Wireless LAN Medium Access Control (MAC) and Physical Layer (PHY) Specifications ― Amendment: Mesh Networking," Nov. 2008*.

[15] A. Baschirotto, R. Castello, F. Campi, G. Cesura, M. Toma, R. Guerrieri, R. Lodi, L. Lavagno, and P. Malcovati, "Baseband analog front-end and digital back-end for reconfigurable multi-standard terminals," *IEEE Circuits and Systems Magazine*, vol.6, no.1, pp. 8- 28, 2006.

[16] T. Shono, Y. Shirato, H. Shiba, K. Uehara, K. Araki, M. Umehira, "IEEE 802.11 wireless LAN implemented on software defined radio with hybrid programmable architecture," *IEEE Trans Wireless Commun.*, vol.4, no.5, pp. 2299- 2308, Sept. 2005

[17] J. L. Hennessy and D. A. Patterson, *Computer Architecture: A Quantitative Approach*, Morgan Kaufmann Publishers, 3rd Edition, 2003.

[18] Shin-Yuan Wang, and Chia-Chi Huang, "On the architecture and performance of an FFT-based spread-spectrum downlink RAKE receiver," *IEEE Trans. Veh. Tech.*, vol.50, no.1, pp.234-243, Jan 2001.

[19] P. K. Prakasam, M. Kulkarni, Xi Chen, Yu Zhuizhuan, S. Hoyos, J. Silva-Martinez, and E. Sanchez-Sinencio, "Applications of multipath transform-domain charge-sampling wide-band receivers," *IEEE Trans. Circuits Syst. II*, vol.55, no.4, pp.309-313, Apr. 2008.

[20] S. Hoyos, B. M. Sadler, and G. R. Arce, "Broad-band multicarrier communications receiver based on analog to digital conversion in the frequency domain," *IEEE Trans. Wireless Commun.*, vol. 5, no. 3, pp. 652–661, Mar. 2006.

[21] Gernot Hueber, and Robert Bogdan Staszewski, *Multi-Mode / Multi-Band RF Transceivers for Wireless Communications: Advanced Techniques, Architectures, and Trends*. Wiley-IEEE Press, November 2010.

[22] S. Hoyos, S. Pentakota,Yu Zhuizhuan,E.S.A. Ghany, Chen Xi, R. Saad, S. Palermo,J. Silva-Martinez, "Clock-Jitter-Tolerant Wideband Receivers: An

Optimized Multichannel Filter-Bank Approach," *IEEE Trans. Circuits Syst. I*, vol.58, no.2, pp.253-263, Feb. 2011.

[23] S. Hoyos, and B. M. Sadler, "UWB mixed-signal transform-domain direct-sequence receiver," *IEEE Trans. Wireless Commun.*, vol. 6, no. 8, pp. 3038-3046, Aug. 2007.

[24] J.-J. van de Beek, M. Sandell, and P. O. Borjesson, "ML estimation of time and frequency offset in OFDM systems," *IEEE Trans. Signal Process.*, vol. 45, no. 7, pp. 1800–1805, Jul. 1997.

[25] H. Minn, V. K. Bhargava, and K. B. Letaief, "A robust timing and frequency synchronization for OFDM systems," *IEEE Trans. Wireless Commun.*, vol. 2, no. 4, pp. 822-839, Jul. 2003.

[26] A. J. Coulston, "Maximum likelihood synchronization for OFDM using a pilot symbol: algorithms," *IEEE J. Sel. Areas Commun.*, vol. 19, no. 12, pp. 2486-2494, Dec. 2001.

[27] E. Sourour and G. E. Bottomley, "Effect of frequency offset on DS-SS acquisition in slowly fading channels," in *Proc. IEEE Wireless Communications and Networking Conf.*, vol. 2, New Orleans, LA, Sept. 1999, pp. 569–573.

[28] A. Fort, J.-W. Weijers , V. Derudder , W. Eberle and A. Bourdoux "A performance and complexity comparison of auto-correlation and cross-correlation for OFDM burst synchronization", in *Proc. IEEE ICASSP*, vol. 2, pp. 341 2003.

[29] F. Tufvesson, O. Edfors, and M. Faulkner, "Time and frequency synchronization for OFDM using PN-sequence preambles," in *Proc. IEEE VTC.*, vol. 4, pp. 2203–2207, 1999.

[30] K. W. Yip, Y. C. Wu, and T. S. Ng, "Timing-synchronization analysis for IEEE 802.11a wireless LANs in frequency-nonselective Rician fading environments," *IEEE Trans. Wireless Commun.*, vol. 3, pp. 387-394, Mar. 2004.

[31] E. G. Larsson, G. Liu, J. Li, and G. B. Giannakis, "Joint symbol timing and channel estimation for OFDM based WLANs," *IEEE Commun. Lett.*, vol. 5, no. 8, pp. 325-327, Aug. 2001.

[32] Y.-C. Wu, K.-W. Yip, T.-S. Ng and E. Serpedin, "Maximum-likelihood symbol synchronization for IEEE 802.11a WLANs in unknown frequency-selective fading channels," *IEEE Trans. Wireless Commun.*, vol. 4, pp. 2751, Nov. 2005.

[33] J. Terry, and J. Heiskala, *OFDM Wireless LANs: A Theoretical and Practical Guide*, Indianapolis, Indiana., Sams, 2002.

[34] P.A. Dmochowski, and P.J. McLane, "Frequency domain equalization for high data rate multipath channels," in *Proc. IEEE Pacific Rim Conf.*, vol.2, pp.534~537, Aug., 2001.

[35] J.J. Shynk, "Frequency-domain and multirate adaptive filtering," *IEEE Signal Process. Mag.*, vol.9, Issue 1, Jan., 1992.

[36] T. D. Chiueh and P. Y. Tsai, *OFDM Baseband Receiver Design for Wireless Communications*. Wiley, September 2007.

[37] P.W. Wolniansky, G.J. Foschini, G.D. Golden, and R.A. Valenzuela, "V-BLAST: An architecture for realizing very high data rates over the rich-scattering wireless channel," in *Proc. IEEE ISSSE*, pp.295–300, Sept. 1998.

[38] X. Zhu and R. D. Murch, "Performance analysis of maximum likelihood detection in a MIMO antenna system," *IEEE Trans. Commun.*, vol. 50, pp. 187–191, Feb. 2002.

[39] E. Viterbo and J. Boutros, "A universal lattice code decoder for fading channels," *IEEE Trans. Inf. Theory*, vol.45, no.5, pp.1639–1642, July 1999.

[40] Kwan-wai Wong; Chi-ying Tsui; Cheng, R.S.-K.; Wai-ho Mow; , "A VLSI architecture of a K-best lattice decoding algorithm for MIMO channels," in *Proc. ISCAS*, vol.3, no., pp. III-273- III-276 vol.3, 2002.

[41] Zhan Guo, and Nilsson, P.; , "A VLSI architecture of the Schnorr-Euchner decoder for MIMO systems," in *Proc. ISCAS*, vol.1, no., pp. 65- 68 Vol.1, 2004.

[42] Mondal, S., Salama, K.N., and Eltawil, A., "On the VLSI Implementation of low complexity K-best MIMO decoders," in *Proc. ICM*, vol., no., pp.337-340, 2008.

[43] Higuchi, K.; Kawai, H.; Maeda, N.; Sawahashi, M.; , "Adaptive selection of surviving symbol replica candidates based on maximum reliability in QRM-MLD for OFCDM MIMO multiplexing," in *Proc. GLOBECOM*, vol.4, no.,

pp. 2480- 2486 Vol.4, 2004.

[44] L. Hideki et al., "Evaluating the Impact of RTS-CTS in OLPC's XOs' Mesh Networks," in *Proc. SBrT*, 2007.

[45] D. Koutsonikolas, J. Dyaberi, P. Garimella, S. Fahmy, Y.C. Hu, "On TCP throughput and window size in a multihop wireless network testbed," in *Proc. WiNTECH07*, Sep. 2007, Montreal, Quebec, Canada.

[46] Y. Sun, I. Sheriff, E.M. Belding-Royer, K.C. Almeroth, "An experimental study of multimedia traffic performance in mesh networks," in *Proc. WitMeMo*, 2005

[47] K. Chebrolu, B. Raman, S. Sen, "Long-distance 802.11b links: performance measurements and experience," in *Proc. MOBICOM*, 2006.

[48] D. Gokhale, S. Sen, K. Chebrolu, B. Raman, "On the feasibility of the link abstraction in (rural) mesh networks," in *Pro. INFOCOM*, 2008, pp.61–65.

[49] J. Camp, J. Robinson, C. Steger, E. Knightly, "Measurement driven deployment of a two-tier urban mesh access network," in *Proc. ACM MobiSys*, June 2006, pp. 96–109.

[50] A. Arjona, C. Westphal, J. Manner, A. Yla-Jaaski, S. Takala, "Can the current generation of wireless mesh networks compete with cellular voice?," in *Proc. Elsevier ComCom Journal*, pp.1564-1578, vol. 31, Issue 8, May 2008.

[51] A. Burg, M. Borgmann, M. Wenk, M. Zellweger, W. Fichtner, and H. Bolcskei, "VLSI implementation of MIMO detection using the sphere decoding algorithm," *IEEE J., Solid-State Circuits*, vol.40, no.7, pp. 1566-1577, July 2005.

[52] *Part 15.3: Wireless Medium Access Control (MAC) and Physical Layer (PHY) Specifications for High Rate Wireless Personal Area Networks (WPANs): Amendment 2: Millimeter-Wave Based Alternative Physical Layer Extension*, *IEEE 802.15.3c*, Oct. 2009.

[53] IEEE 802.11ad Task Group, 2010. [Online]. Available: http://www.ieee802.org/11/Reports/tgad update.htm

[54] J. Proakis and D. Manolakis, *Digital Signal Processing: Principles, Algorithm, and Applications*, 3rd ed. Englewood Cliffs, NJ: Prentice-Hall, 1996.

[55] B. O'Hara, and A. Petrick, *IEEE 802.11 Handbook: A Designer's Companion*,

IEEE Press, 2nd Edition, 2005.

[56] V. Erceg, et al., *TGn channel models*, *IEEE 802.11-03/940r4*, May, 2004.

[57] T. Y. Hsu, B. J. Shieh, and C. Y. Lee, "An all-digital phase-locked loop (ADPLL) based clock recovery circuits," *IEEE J. Solid-State Circuits*, vol. 34, pp. 1063-1073, Aug. 1999.

[58] C. C. Chung and C. Y. Lee, "An all-digital phase-locked loop for high-speed clock generation," *IEEE J. Solid-State Circuits*, vol. 38, pp. 347-351, Feb. 2003.

[59] M. Krstic, A. Troya, K. Maharatna, and E. Grass, "Optimized low-power synchronizer design for the IEEE 802.11a standard," in *Proc. ICASSP '03*, vol.2, no., pp. II- 333-6 vol.2, 6-10, 2003.

[60] T.-H. Kim, and I.-C. Park, "Low-Power and High-Accurate Synchronization for IEEE 802.16d Systems," *IEEE Trans. VLSI*, vol.16, no.12, pp.1620-1630, Dec. 2008.

[61] H.-Y. Liu; C.-Y. Lee, "A Low-Complexity Synchronizer for OFDM-Based UWB System," *IEEE Trans. Circuits Syst. II*, vol.53, no.11, pp.1269-1273, Nov. 2006.

[62] B. M. Baas, "A low-power, high-performance, 1024-point FFT processor", *IEEE J. Solid-State Circuits*, vol. 34, no. 3, pp. 380 - 387, 1999.

[63] A. Chun, E. Tsui, I. Chen, H. Honary, and J. Lin, "Application of the Intel@ Reconfigurable Communication Architecture to 802.11a, 3G and 4G Standards," in *Proc. IEEE Symp. Emerging Technol.*, May, 2004. pp.659~662.

[64] J. Hoffman, D. A. Ilitzky, A. Chun, and A. Chapyzhenka, "Architecture of the Scalable Communications Core," in *Proc. IEEE Symp. Networks-on-Chip*, 2007, pp. 40–52..

[65] J.H. Jang, H.C. Won, and G.H. Im, "Cyclic Prefixed Single Carrier Transmission with SFBC over Mobile Wireless Channels," *IEEE Signal Process, Lett.*, vol.13, no.5, pp.261~264, May, 2006.

[66] M. Morelli, L. Sanguinetti, and U. Mengali, "Channel Estimation for Adaptive Frequency-Domain Equalization," *IEEE Trans Wireless Commun.,* vol.4, no.5, pp.2508~2518, Sep., 2005.

[67] Y. Zhu, and K.B. Letaief, "Single Carrier Frequency Domain Equalization with

Time Domain Noise Prediction for Wideband Wireless Communications," *IEEE Trans Wireless Commun*, vol.5, no.12, pp.3548-3557, Dec. 2006.

[68] D. Falconer, "Frequency Domain Equalization for Single-Carrier Broadband Wireless Systems," *IEEE Commun. Mag.*, pp.58~66, April, 2002.

[69] Wang, X. Dong, P.H. Wittke, and S. Mo, "Cyclic Prefixed Single Carrier Transmission in Ultra-wideband Communications," *IEEE Trans Wireless Commun*, vol.5, no.8, pp.2017~2021, Aug., 2006.

[70] N. Benvenuto, and S. Tomasin, "On the Comparison Between OFDM and Single Carrier Modulation with a DFE Using a Frequency-Domain Feedforward Filter," *IEEE Trans Commun*, vol.50, no.6, pp.947~955, June, 2002.

[71] K.Wong, C. Tsui, R.-K. Cheng, and W. Mow, "A VLSI architecture of a K-best lattice decoding algorithm for MIMO channels," in Proc. IEEE ISCAS, vol. 3, pp.273~276, 2002.

[72] M. O. Damen, H. E. Gamal, and G. Caire, "On Maximum-Likelihood Detection and the Search for the Closest Lattice Point," IEEE Trans Information, vol.49, no.10, pp.2389~2402 Oct., 2003.

[73] Sizhong Chen, Tong Zhang, and Yan Xin, "Relaxed K-Best MIMO Signal Detector Design and VLSI Implementation," *IEEE Trans VLSI*, vol.15, no.3, pp.328-337, March 2007.

[74] K. Pahlavan, and A.H. Levesque, *Wireless Information Networks*, New York: Wiley, 1995.

[75] J. Terry, and J. Heiskala, *OFDM Wireless LANs: A Theoretical and Practical Guide*, Indianapolis, Indiana., Sams, 2002.

[76] G. Ungerboeck, "Adaptive Maximum-Likelihood Receiver for Carrier-Modulated Data-Transmission Systems," *IEEE Trans Commun.*, vol.22, no.5, pp.624~636, May, 1974.

[77] S. Lin, and D.J. Costello, *Error Control Coding: Fundamentals and Applications*, Prentice Hall, 1983.

[78] S.W. Gerstacker, C. Jonietz, and R. Schober, "Equalization for WLAN IEEE 802.11b," in *Proc. IEEE Int. Conf. Commun.*, vol.6, pp.20~24, June, 2004.

[79] K. Barman, and A.V. Malipatil, "ICI equalizer in a CCK based DSSS communication system," in *Proc. TENCN*, vol. 4, pp.15~17, Oct. 2003.

[80] R. Pandey and M. L. Bushnell, "Architecture for variable-length combined FFT, DCT and MWT transform hardware for multi-mode Wireless system," in *Proc. IEEE Inter. Conf. Embedded Syst.*, Jan. 2007, pp. 121–126.

[81] IEEE P802.16e, *IEEE Standard for Local and Metropolitan Area Networks, Part 16: Air Interface for Fixed and Mobile Broadband Wireless Access Systems, P802.16Rev2/D2*, Dec. 2007.

[82] I-Wei Lai; Ascheid, G.; Meyr, H.; Tzi-Dar Chiueh; , "Efficient Channel-Adaptive MIMO Detection Using Just-Acceptable Error Rate," *IEEE Trans Wireless Commun.*, vol.10, no.1, pp.73-83, January 2011.

[83] Yugang Jia; Andrieu, C.; Piechocki, R.J.; Sandell, M., "Depth-First and Breadth-First Search Based Multilevel SGA Algorithms for Near Optimal Symbol Detection in MIMO Systems," *IEEE Trans Wireless Commun.*, vol.7, no.3, pp.1052-1061, March 2008.

[84] G.A. Awater, A. van Zelst, and R. van Nee, "Reduced complexity space division multiplexing receivers," in *Proc. VTC*, pp.11–15, May 2000.

[85] C. Perkins and E. Royer, "Ad-Hoc On-Demand Distance Vector Routing," in *Proc. Mobile Comp. Sys. Apps.*, 1999.

[86] M. Bahr, "Proposed Routing for IEEE 802.11s WLAN Mesh Networks," in *Proc. Int'l. Wksp. Wireless Internet*, 2006.

[87] A. Doufexi et al., "A Comparison of the HIPERLAN/2 and IEEE 802.11a Wireless LAN Standards," *IEEE Commun. Mag.*, vol. 40, no. 5, May 2002, pp. 172–80.

[88] A. Kamerman and L. Monteban, "WaveLAN-II: A High-Performance Wireless LAN for the Unlicensed Band," *Bell Labs. Tech. J.*, 1997, pp. 118–33.

[89] D. Raychaudhuri, I. Seskar, M. Ott, S. Ganu, K. Ramachandran, H. Kremo, R. Siracusa, H. Liu, M. Singh, "Overview of the ORBIT radio grid testbed for evaluation of next-generation wireless network protocols," in *Proc. WCNC*, vol. 1663, 2005, pp. 1664–1669.

[90] T. Murakami, Y. Matsumoto, K. Fujii, Y. Yamanaka, "Effects of multipath propagation on microwave oven interference in wireless systems," in *Proc. Electromagnetic Compatibility*, 2003, vol. 742, 2003, pp. 749–752.

[91] D. Eckhardt, P. Steenkiste, "Measurement and analysis of the error characteristics of an in-building wireless network," in *Proc. ACM SIGCOMM*, Aug. 1996, pp. 243–254.

[92] S. Xu, T. Saadawi, "Does the IEEE 802.11 MAC protocol work well in multihop wireless ad hoc networks?," *IEEE Commun. Mag.*, vol.39, no.6, pp.130-137, Jun 2001

[93] Y.-D. Lin, S.-L. Tsao, S.-L. Chang, S.-Y. Cheng, C.-Y. Ku, "Design issues and experimental studies of wireless LAN mesh," *IEEE Wireless Commun.*, vol.17, no.2, pp.32-40, April 2010.

[94] R. Jones, Netperf Homepage, in. <http://www.netperf.org>.

[95] M. Afanasyev, T. Chen, G.M. Voelker, A.C. Snoeren, "Analysis of a mixed-use urban wifi network: when metropolitan becomes neapolitan," in *Proc. of ACM SIGCOMM*, 2008, pp. 85–98.

[96] S. Liese, D. Wu, P. Mohapatra, "Experimental characterization of an 802.11b wireless mesh network," in *Proc. of IWCMC*, 2006, pp. 587–592.

[97] E. Borgia, F. Delmastro, "Effects of unstable links on AODV performance in real testbeds," *EURASIP Journal of Wireless Communication Network*, 2007, pp.32–32.

[98] C.E. Perkins, E.M. Royer, "Ad-hoc on-demand distance vector routing," in *Proc. WMCSA*, 1999, pp. 90–100.